Search for the Standard Model Higgs boson decaying to a bottom-quark pair with the ATLAS detector

Kenji Kiuchi
Doctoral Program in Physics

Submitted to the Graduate School of Pure and Applied Sciences in Partial Fulfillment of the Requirements for the Degree of Doctor of Philosophy in Science

at the
University of Tsukuba

Abstract

A search for the Standard Model Higgs boson produced in association with a weak boson ($W^{\pm}H/Z^0H$) and decaying to a bottom-quark pair is performed at the ATLAS experiment. The data sample consists of proton-proton collisions recorded with the ATLAS detector at the Large Hadron Collider operated at a center-of-mass energy of $\sqrt{s} = 8$ TeV, corresponding to an integrated luminosity of 20.3 fb^{-1}. Three Higgs signal channels are considered in the search: $Z^0H \to \nu\bar{\nu}b\bar{b}$, $W^{\pm}H \to \ell^{\pm}\nu b\bar{b}$ and $Z^0H \to \ell^+\ell^- b\bar{b}$.

A multivariate analysis (MVA) technique is employed and MVA distributions are used to extract the significance and strength of possible Standard Model Higgs boson signals. With a combination of the full 2011 proton-proton collision data sample of 4.6 fb^{-1} recorded at $\sqrt{s} = 7$ TeV, the observed (expected) deviation from the background-only hypothesis corresponds to a local significance of 1.4 (2.6) standard deviations and the ratio of the measured signal yield to the Standard Model prediction for a Higgs mass of 125 GeV/c^2 is found to be $\mu = 0.51 \pm 0.31\ (\text{stat}) \pm 0.24\ (\text{syst})$. This analysis has the world's best expected sensitivity to the Standard Model Higgs boson with a mass of 125 GeV/c^2 and decaying to a bottom quark pair.

The analysis procedure is validated with a cut-based analysis. The signal strength obtained by the cut-based analysis is $\mu = 1.12 \pm 0.42\ (\text{stat}) \pm 0.40\ (\text{syst})$, and the corresponding observed (expected) significance is 2.1 (2.0) standard deviations, which are consistent with the MVA analysis results. The multivariate analysis method is also applied to a measurement of the diboson ($W^{\pm}Z^0/Z^0Z^0$) production rate with the decay mode $Z^0 \to b\bar{b}$. The observed diboson signal strength is found to be $\mu_{VZ} = 0.79 \pm 0.11\ (\text{stat}) \pm 0.16\ (\text{syst})$, consistent with the Standard Model predictions. The observed (expected) significance of the diboson signal is 4.9 (6.3) standard deviations.

Acknowledgments

I would like to thank my advisor Fumihiko Ukegawa. I am greatful for his many corrections for this thesis and proof-reading. I really appreciate to all people within the University of Tsukuba ATLAS group: Shinhong Kim, Kazuhiko Hara, Koji Sato, Koichi Nagai, Takayasu Hayashi, Keita Hanawa. Shinhong Kim gave me a lot of advice when I start the study at ATLAS experiment. Kazuhiko Hara always gave me a lot of useful suggestions.

I want to express my appreciation for all ATLAS collaborators. I also thank CERN for the very successful operation of the LHC.

First, I studied errors recorded at the ATLAS semiconductor tracker system in the ATLAS semiconductor tracker working group. I am greatful to ATLAS semiconductor tracker working group conveners: Steve McMahon and Dave Robinson and all ATLAS semiconductor tracker working group people. I was a really beginner and was slow to get work done. They wait patiently until I finish the work.

I would like to thank ATLAS $H \to b\bar{b}$ study working group conveners: Ricardo Jose Morais Silva Goncalo, Heather Gray, Christian Weiser, Andrew Metha, Giacinto Piacquadio. They encourage me many times and I can concentrate on my work thanks to their leadership. I am thankful to all the ATLAS $H \to b\bar{b}$ study working group members:

F. Ahmadov, Da Palma, A. M., L. Alio, B.M.M. Allbrooke, T. Bristow, D. Buescher, A. Buzatu, Y. Coadou, P. Conde Muio, C. Debenedetti, Y. Enari, G. Facini, W. Fisher, P. Francavilla, G. Gaycken, G. Gonzalez Parra, J.F. Grivaz, C. Gwilliam, S. Hagebck, G. Halladjian, M. Jackson, D. Jamin, R. Jansky, V. Kostyukhin, K. Lohwasser, D. Lopez Mateos, U. Mallik, J. Maneira, G. Marchiori, M. Martinez Perez, K. Mercurio, K. Mochizuki, N. Morange, Y. Ming, P. Mullen, Y. Nagai, J. Nielsen, I. Ochoa, A. Palma, C. Pandini, R. Pedro, M. Proissl, T. Ravenscroft, P. Rose, T. Scanlon, E. Schopf, S. Shaw, B. Smart, V. Sorin, M. Sousa, F. Sforza, J. Therhaag, P.D. Thompson, L. Vacavant, J. Wang, C. Wang, S. Wang, C. Weiser, R. Zaidan , L. Zhang. I had a lot of discussions with them and exchange interesting ideas.

Especially, I am truly grateful for the Yoshikazu Nagai's help. I express my warm thanks to Yuji Enari for his encouragement. I would also like to many thank Kazuya Mochizuki for the very useful discussion.

Contents

List of Figures

List of Tables

Chapter 1

Introduction

1.1 Experimental inputs

The goal of particle physics is to acquire the most fundamental and essential understanding of our world. In order to accumulate suitable experiences, particle physicists study elementary particles, which constitute the most fundamental unit of our world. All phenomena in this world are to be described by fundamental particles and their interactions. The mediator of the interactions is also understood as particles. There are two types of particles. One is half-integer spin particles called the fermions, which obey the Fermi-Dirac statistics, hence the Pauli exclusion principle. The other is integer spin particles called the bosons, which obey the Bose-Einstein statistics and mediate the forces between the fermions.
Experimentally observed elementally particles are summarised in Figure 1.1. There are four types of interactions between the fermions. The gluon mediates the strong interaction which is the strongest interaction. The electromagnetic interaction is the most familiar interaction and it is also most thoroughly understood. The photon is the mediator of the electromagnetic interaction. The weak interaction plays an important role in radioactive decays and nuclear fusion. The $W^{\pm}$ and Z^0 bosons carry the weak force. The gravitational interaction is a familiar force and highlighted by the general relativity. In fact, the interaction strength is very weak ($\mathcal{O}(10^{-36})$ smaller than electromagnetic interaction) compared to the other interactions, therefore the gravitational interaction is not measureable with the ATLAS detector and is not discussed in this thesis. The twelve fermions are categorised into six quarks and six leptons by their response to the strong interaction. The leptons do not interact through the strong interactions. On the other hand, the six quarks are engaged in the strong interaction. There are up-type quarks, down-type quarks, charged leptons and neutral leptons, which have an electric charge of $+2/3$, $-1/3$, -1 and 0, respectively. Such a group forms a generation and three generations have been experimentary identified. In ascending order of the mass, the up-type quarks are named up-quark, charm-quark and top-quark. The down-type quarks are labelled as down-quark, strange-quark and bottom-quark. The charged leptons are called electron, muon (μ) and tau (τ). The neutral leptons are electron-neutrino, muon-neutrino and tau-neutrino.
The quarks are not directly ovservable due to the characteristic property (quark confinement) of the strong interaction. The quarks construct composite particles called hadrons. The hadrons are categorised into baryons and mesons. The baryons consist of three quarks. The most familiar baryons are proton and neutron. The mesons are composed of a quark and an anti-quark. Baryons made of one type of quarks (Δ^{++} (uuu), Δ^{-} (ddd) and Ω^{-} (sss)) have been observed and they have spin 3/2. If three quarks are identical particle, the three same fermions occupy the same ground state, which is forbidden by the Pauli exclusion principle. Additional quantum number "colour" is considered as a solution to this problem. Each quark has three different colours (red, green and blue).
The Higgs boson is the only particle which has spin 0. It gives masses for all particles in terms of interaction in between. The mass of the particle is determined by the coupling strength between the particle and Higgs boson. However, the coupling strength for each fermion and the origin of the mass generations are not explained by the theory. The study of the Higgs-fermion (Yukawa) coupling is a first step for understanding the underlying theory.

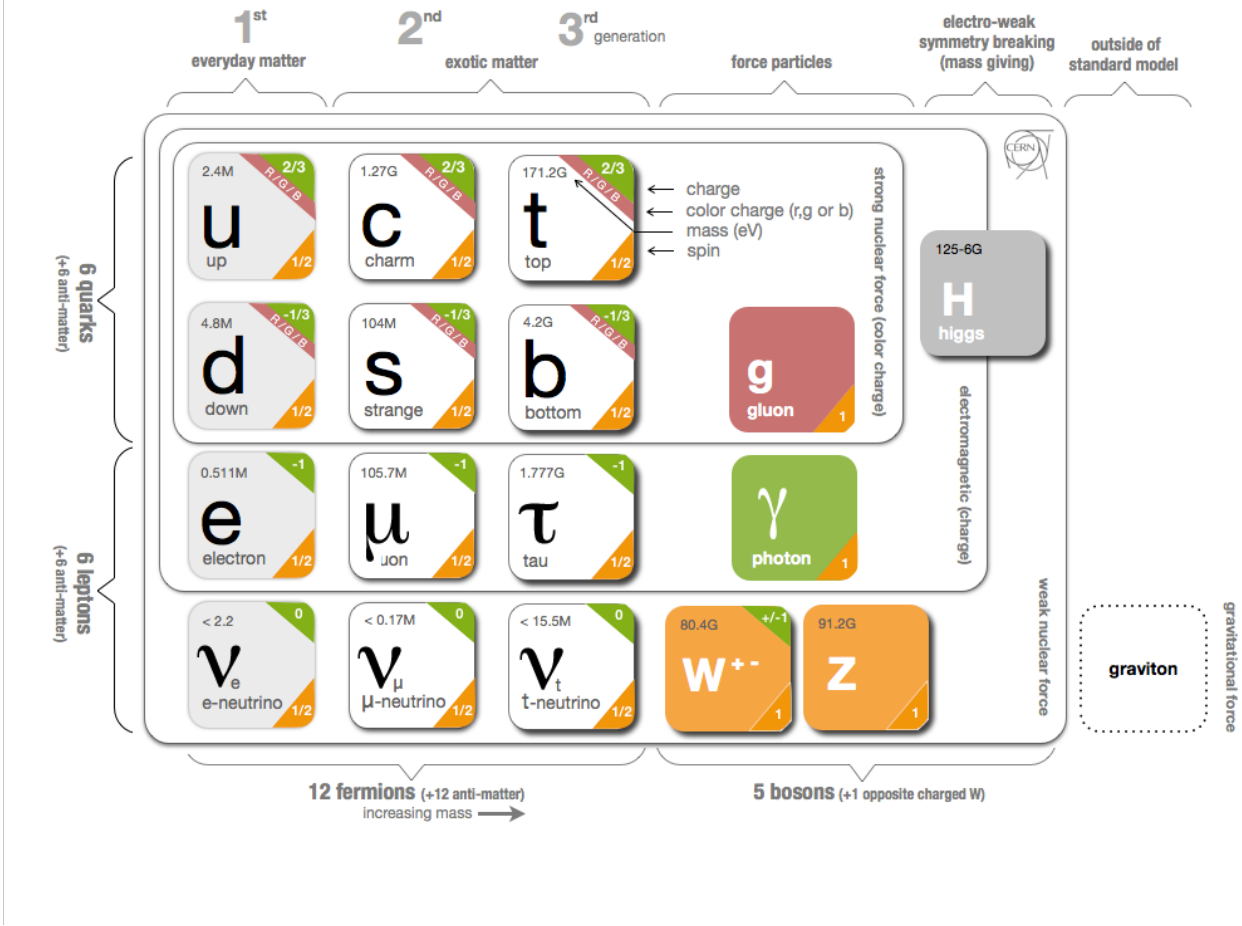

Figure 1.1: The elementary particles and their characteristics are shown [1]. There are six quarks and six leptons which have spin-$1/2$. The gluon, the photon and the weak bosons ($W^{\pm}$ and Z^0) are spin-1 particles which mediate the strong interaction, the electromagnetic interaction and the weak interaction, respectively. The graviton is spin-2 particle to responsible to the gravitational interaction, which is not observed yet. The Higgs boson is spin-0 particle which gives masses to all particles.

1.2 The Standard Model

The "Standard Model (SM)" is a summarised physics model of excellent achievements in particle physics. It explains almost all the data taken by various experiments and there is no negative result contradicting to this model. The basis of the Standard Model (SM) is a quantum field theory (QFT) with local gauge symmetry (gauge theory). The particles are expressed as an excitation states of fields in the QFT.
The Lagrangian density for a free massive fermion field is known as Dirac Lagrangian [2, 3] and written as

$$\mathscr{L} = \bar{\psi}\left(i\partial\!\!\!/ - m\right)\psi, \quad \bar{\psi} \equiv \psi^{\dagger}\gamma^{0} \text{ and } \partial\!\!\!/ \equiv \gamma^{\mu}\partial_{\mu} \tag{1.1}$$

where ψ is a fermion field and m is its mass. The Euler-Lagrange equation for $\bar{\psi}$ is the Dirac equation.

$$\partial_{\mu}\left(\frac{\partial\mathscr{L}}{\partial\left(\partial_{\mu}\bar{\psi}\right)}\right) - \frac{\partial\mathscr{L}}{\partial\bar{\psi}} = \left(i\partial\!\!\!/ - m\right)\psi = 0. \tag{1.2}$$

All the fermions are equivalent except their masses with this equation. The next step is adding boson terms and interaction terms to this Lagrangian. In the SM, three types of interactions are described by three symmetry groups:

$$\mathrm{SU}(3)_C \otimes \mathrm{SU}(2)_L \otimes \mathrm{U}(1)_{Y_W}. \tag{1.3}$$

This means that there are eight vector field known as gluons from $\mathrm{SU}(3)_C$ symmetry, three vector fields as a generator of $\mathrm{SU}(2)_L$ and one vector fields from $\mathrm{U}(1)_{Y_W}$. The $\mathrm{SU}(3)_C$ group describes the strong interaction, "C" denoting the colours. The $\mathrm{SU}(2)_L \otimes \mathrm{U}(1)_{Y_W}$ groups express origin of weak interaction and electromagnetic interaction. These two interactions are unified to the electroweak framework, "L" and "Y" denoting weak isospin in left handed particles and weak hypercharge, respectively. We cannot see $\mathrm{SU}(2)_L \otimes \mathrm{U}(1)_{Y_W}$ symmetry groups directly in our current world, since they are broken into $\mathrm{U}(1)_{EM}$ via spontaneously symmetry breaking.

$$\mathrm{SU}(3)_C \otimes \mathrm{SU}(2)_L \otimes \mathrm{U}(1)_{Y_W} \;\rightarrow\; \mathrm{SU}(3)_C \otimes \mathrm{U}(1)_{EM}. \tag{1.4}$$

The $\mathrm{U}(1)_{EM}$ is the electromagnetic theory that is the simplest and familiar theory. This section reviews the electromagnetic theory in the QFT form and generalises it to explain $\mathrm{SU}(3)_C$ and $\mathrm{SU}(2)_L$ theories. Finally, $\mathrm{SU}(2)_L$ and $\mathrm{U}(1)_{EM}$ are the unified to the electroweak theory. Higgs boson plays a unique role in the electroweak theory.

1.2.1 An Abelian gauge theory: Quantum Electrodynamics (QED)

The classical electromagnetic theory was first stated gauge theory and it has been developed to one of the most successful theories in physics. The quantilisation of the electromagnetic field was first studied by Dirac [4] and elegantly formulated by Fermi [5]. The remaining issue, the infinite integral due to higher order effects in perturbation theory, was solved by Schwinger, Feynman, Tomonaga and Dyson [6–12]. The framework is called Quantum Electrodynamics (QED), which has a U(1) gauge symmetry. The corresponding vector field is the photon. If we consider a bi-spinor field of spin 1/2 particle (ψ) with electromagnetic field (A_{μ}), the Lagrangian is written as [2, 3]

$$\mathscr{L}_{\mathrm{QED}} = \mathscr{L}_{\mathrm{Dirac}} + \mathscr{L}_{\mathrm{Maxwell}} + \mathscr{L}_{\mathrm{Interaction}} \tag{1.5}$$

$$= \bar{\psi}(i\partial\!\!\!/_{\mu} - m)\psi - \frac{1}{4}F_{\mu\nu}F^{\mu\nu} - e\bar{\psi}\gamma^{\mu}\psi A_{\mu} \tag{1.6}$$

where $F_{\mu\nu}$ is an electromagnetic field tensor

$$F_{\mu\nu} = \partial_{\nu}A_{\mu} - \partial_{\mu}A_{\nu} \tag{1.7}$$

and e is the coupling constant equal to the electric charge in the QED. The first term corresponds to the kinetic energy and mass of the fermion, the second term is the Maxwell field energy in covariant four field form, and

the third term describes the interaction of the fermion with the electromagnetic field. The Lagrangian can also be written as

$$\mathscr{L}_{\text{QED}} = \bar{\psi}(i\not{D}_\mu - m)\psi - \frac{1}{4}F_{\mu\nu}F^{\mu\nu}, \tag{1.8}$$

where D_μ is the gauge covariant derivative

$$D_\mu \equiv \partial_\mu + ieA_\mu(x). \tag{1.9}$$

The QED Lagrangian is invariant under the U(1) local gauge transformation.

$$\psi(x) \to e^{i\alpha(x)}\psi(x), \quad A_\mu \to A_\mu - \frac{1}{e}\partial_\mu\alpha(x). \tag{1.10}$$

The Euler-Lagrange equation for ψ is the Dirac equation with an interaction with the electromagnetic field.

$$(i\not{D} - m)\,\psi = 0. \tag{1.11}$$

The Euler-Lagrange equation for A_μ is

$$\partial_\mu F^{\mu\nu} = e\bar{\psi}\gamma^\nu\psi = ej^\nu \tag{1.12}$$

where j^ν is the Noether current [2, 3].

1.2.2 A non-Abelian gauge theory: Quantum Chromodynamics (QCD)

The U(1) Abelian gauge theory was generalised by Yang and Mills [13]. The theory of the quarks and gluons has an SU(3) gauge symmetry. The charge called colour was introduced by Greenberg, Nambu and Han [14–16]. This theory is called Quantum Chromo-Dynamics (QCD). The Lagrangian is written as [2, 3]

$$\mathscr{L}_{\text{QCD}} = \bar{\psi}_i(i(\not{D}_\mu)_{ij} - m\delta_{ij})\psi_j - \frac{1}{4}G^a_{\mu\nu}G^{a\mu\nu} \tag{1.13}$$

where ψ_i is the quark field. The gauge invariant gluon field strength is written as

$$G^a_{\mu\nu} = \partial_\mu A^a_\nu - \partial_\nu A^a_\mu + g_s f^{abc}A^b_\mu A^c_\nu \tag{1.14}$$

where $a =$ 1-8 corresponds to the gluon colours , g_s is the strong coupling constant and f^{abc} is the structure constant that satisfies the relation

$$[\lambda^a, \lambda^b] = 2if^{abc}\lambda^c, \tag{1.15}$$

where λ matrices are the Gell-Mann matrices. The covariant derivative is

$$D_{\mu ij} = \partial_\mu\delta_{ij} + ig_s G^\alpha_\mu \lambda^\alpha_{ij} \tag{1.16}$$

Obviously, the G^2 term has three- and four-point gluon self interactions.

1.2.3 Brout-Englert-Higgs (BEH) mechanism

This section discusses the simplest example of BEH mechanism. The $W^\pm$ and Z^0 bosons have masses 80 GeV and 91 GeV, respectively. If we consider the gauge term in QED Lagrangian with a mass term, the Lagrangian is

$$\mathscr{L} = -\frac{1}{4}F_{\mu\nu}F^{\mu\nu} + \frac{1}{2}m^2A_\mu A^\mu. \tag{1.17}$$

Clearly, the mass term violates the local gauge invariance. Thus we need to explain weak boson masses while keeping the local gauge invariance, which is achieved by the BEH mechanism. [17–22] The simplest extension is adding a single complex scalar field, ϕ. Then the Lagrangian becomes

$$\mathscr{L} = -\frac{1}{4}F_{\mu\nu}F^{\mu\nu} + \left|D_\mu\phi\right|^2 - V(\phi), \tag{1.18}$$

where

$$D_\mu = \partial_\mu - ieA_\mu \tag{1.19}$$

$$V(\phi) = -\mu^2\phi^*\phi + \frac{\lambda}{2}(\phi^*\phi)^2 \tag{1.20}$$

where μ and λ are the mass and self-interaction coupling constant of the scalar field. The Lagrangian is invariant under local gauge transformation. If $\mu^2 < 0$ the vacuum state is $\phi = 0$. Another possibility, in case of $\mu^2 > 0$, the vacuum expectation value (VEV) of ϕ is at

$$\langle\phi\rangle = \phi_0 = \sqrt{\frac{\mu^2}{\lambda}}. \tag{1.21}$$

The field $\phi(x)$ is expanded about the VEV as

$$\phi(x) = \phi_0 + \frac{1}{\sqrt{2}}(\phi_1(x) + i\phi_2(x)). \tag{1.22}$$

The potential term is written as

$$V(\phi) = \frac{1}{2}(\sqrt{2}\mu)^2\phi_1^2 - \frac{1}{2\lambda}\mu^4 + \mathscr{O}(\phi_i^3). \tag{1.23}$$

This formula is understood that ϕ_1 is an excitation along the radial potential direction thus it has a mass $m_{\phi_1} = \sqrt{2}\mu$, corresponding to the Higgs boson. ϕ_2 is a massless goldstone boson.
If we choose the unitarity gauge, the Lagrangian is also written as

$$\mathscr{L} = -\frac{1}{4}F_{\mu\nu}F^{\mu\nu} + (\partial_\mu\phi)^2 + e^2\phi^2 A_\mu A^\mu - V(\phi). \tag{1.24}$$

The degrees of freedom are conserved, where the goldstone boson is absorbed into a massive boson which has a mass $m_A = \sqrt{2}e\phi_0$.

1.2.4 Electroweak theory: The Glashow Weinberg Salam theory

The electroweak theory is a theory with $\mathrm{SU}(2)_L \otimes \mathrm{U}(1)_{Y_W}$ symmetry. In this section, previous example is extended to the $\mathrm{SU}(2)_L \otimes \mathrm{U}(1)_{Y_W}$ symmetry. Glashow, Weinberg and Salam with many others contributed to construct this unified theory of electromagnetic interaction and weak interaction [23–25]. The Lagrangian is written as

$$\mathscr{L}_{\mathrm{EWK}} = \mathscr{L}_{\mathrm{Dirac}} + \mathscr{L}_{\mathrm{gauge}} + \mathscr{L}_{\mathrm{Higgs}} + \mathscr{L}_{\mathrm{Yukawa}} \tag{1.25}$$

The gauge term of electroweak theory is

$$\mathscr{L}_{\mathrm{gauge}} = -\frac{1}{4}A^i_{\mu\nu}A^{i\mu\nu} - \frac{1}{4}B_{\mu\nu}B^{\mu\nu}, \tag{1.26}$$

where

$$A^i_{\mu\nu} = \partial_\mu A^i_\nu - \partial_\nu A^i_\mu + g\varepsilon^{ijk}A^j_\mu A^k_\nu, \tag{1.27}$$

$$B_{\mu\nu} = \partial_\mu B_\nu - \partial_\nu B_\mu. \tag{1.28}$$

The first term and second term correspond to the SU(2) and the U(1) gauge field energy. The complex Higgs doublet is

$$\Phi = \frac{1}{\sqrt{2}}\begin{pmatrix}\phi_1 & + & i\phi_2 \\ H & + & i\phi_0\end{pmatrix}. \tag{1.29}$$

The H denotes Higgs field. The Higgs potential is given by

$$V(\Phi) = -\mu^2\left|\Phi^\dagger\Phi\right| + \frac{\lambda}{2}\left(\left|\Phi^\dagger\Phi\right|\right)^2 \tag{1.30}$$

The vacuum expectation value is

$$\langle \Phi \rangle = \frac{1}{\sqrt{2}} \begin{pmatrix} 0 \\ v \end{pmatrix}, \quad v \equiv \sqrt{\frac{2\mu^2}{\lambda}}. \tag{1.31}$$

The covariant derivative of Φ is

$$D_\mu \Phi = \left(\partial_\mu - igA^a_\mu \tau^a - i\frac{1}{2} g' B_\mu \right) \Phi \tag{1.32}$$

where A^a_μ and B_μ are SU(2) and U(1) gauge bosons. The kinetic energy term of Higgs boson is

$$\mathscr{L}_{\text{HiggsKin}} = \frac{1}{2}(0\ v) \left(gA^a_\mu \tau^a + \frac{1}{2} g' B_\mu \right) \left(gA^{b\mu} \tau^b + \frac{1}{2} g' B^\mu \right) \begin{pmatrix} 0 \\ v \end{pmatrix} \tag{1.33}$$

$$= \frac{1}{2} \frac{v^2}{4} \left[g^2 (A^1_\mu)^2 + g^2 (A^2_\mu)^2 + \left(-gA^3_\mu + g' B_\mu \right)^2 \right] \tag{1.34}$$

$$W^\pm_\mu = \frac{1}{\sqrt{2}} \left(A^1_\mu \pm iA^2_\mu \right) \quad \text{with mass} \quad m_W = g\frac{v}{2} \tag{1.35}$$

$$Z^0_\mu = \frac{1}{\sqrt{g^2 + g'^2}} \left(gA^3_\mu - g' B_\mu \right) \quad \text{with mass} \quad m_Z = \sqrt{g^2 + g'^2}\frac{v}{2} \tag{1.36}$$

$$A_\mu = \frac{1}{\sqrt{g^2 + g'^2}} \left(g' A^3_\mu - gB_\mu \right) \quad \text{with mass} \quad m_\gamma = 0 \tag{1.37}$$

Three bosons have "eaten" the goldstone bosons presented in the Higgs field and acquired the masses. The photon stays massless.
The fermion masses are given by the Yukawa interactions between the Higgs boson and fermions.

$$\mathscr{L}_{\text{Yukawa}} = -\bar{Q}_{L_i} Y^d_{ij} \Phi d_{R_j} - \bar{Q}_{L_i} Y^u_{ij} \bar{\Phi} u_{R_j} - \bar{L}_{L_i} Y^l_{ij} \Phi e_{R_j} + h.c., \tag{1.38}$$

where $\bar{\Phi} = i\sigma_2 \Phi^*$, Y_{ij} are 3×3 parameterised Yukawa couplings, Q, d, u, L and e are the quark and lepton fields. The left handed particles Q and L construct SU(2) doublets. More simple form is obtained with diagonalised Yukawa couplings $M^f_{ij} = V^f_{L_{ij}} Y^f_{ij} V^{f\dagger}_{R_{ij}} (v/\sqrt{2})$ and redefined fermion fields with mass eigen states form ${F'}^f_{L_i} = (V^f_{L_{ij}}) F^f_{L_j}$ and ${F'}^f_{R_i} = (V^f_{R_{ij}}) F^f_{R_j}$, where $V^f_{L_{ij}}$ and $V^f_{R_{ij}}$ are unitarity matrices The Yukawa Lagrangian is given by

$$\mathscr{L}_{\text{Yukawa}} = -\bar{Q'}_{L_i} M^d_{ij} d'_{R_j} - \bar{Q'}_{L_i} M^u_{ij} u'_{R_j} - \bar{L'}_{L_i} M^l_{ij} e'_{R_j} + h.c., \tag{1.39}$$

where M^f_{ij} are the diagonalised matrices which contain fermion masses.

$$M^u = \begin{pmatrix} m_u & 0 & 0 \\ 0 & m_c & 0 \\ 0 & 0 & m_t \end{pmatrix}, \ M^d = \begin{pmatrix} m_d & 0 & 0 \\ 0 & m_s & 0 \\ 0 & 0 & m_b \end{pmatrix}, \ M^l = \begin{pmatrix} m_e & 0 & 0 \\ 0 & m_\mu & 0 \\ 0 & 0 & m_\tau \end{pmatrix}. \tag{1.40}$$

The neutrino masses could be added with similar mass term M^ν, if we assume the existence of right handed neutrinos ν_R. The Cabibbo-Kobayashi-Maskawa (CKM) matrix [26, 27] and the Pontecorvo-Maki-Nakagawa-Sakata matrix [28, 29] are defined as

$$V_{\text{CKM}} = V^u_L V^{d\dagger}_L, \quad V_{\text{PMNS}} = V^\nu_L V^{l\dagger}_L \tag{1.41}$$

1.2.5 The Standard Model Lagrangian

Finally, the Standard Model Lagrangian is written as a combination of the QCD and the electroweak theories.

$$\mathscr{L}_{\text{SM}} = \mathscr{L}_{\text{Dirac}} + \mathscr{L}_{\text{gauge}} + \mathscr{L}_{\text{Higgs}} + \mathscr{L}_{\text{Yukawa}} \tag{1.42}$$

For the perturbative calculation, the gauge-fixing term and the Faddeev-Popov ghost term [30] are added to quantilise the Lagrangian with R_ξ gauge.

$$\mathscr{L}_{\text{SM}} = \mathscr{L}_{\text{Dirac}} + \mathscr{L}_{\text{gauge}} + \mathscr{L}_{\text{Higgs}} + \mathscr{L}_{\text{Yukawa}} + \mathscr{L}_{\text{gauge-fix}} + \mathscr{L}_{\text{ghost}} \tag{1.43}$$

1.3 Perturbative QCD for hadron hadron collisions

The cross section of the process ($h_1h_2 \to P_1P_2 + X$) in hadron hadron collisions is written as

$$\sigma(P_1,P_2) = \sum_{i,j} \int dx_1 dx_2 f_{i/h_1}(x_1,\mu_F^2) f_{j/h_2}(x_2,\mu_F^2) \hat{\sigma}_{ij}(p_1,p_2,\alpha_s(\mu_R)Q),\mu_F^2,\mu_R^2). \tag{1.44}$$

where $f_{i/h}(x,\mu_F)$ is parton distribution function (PDF), $\hat{\sigma}$ is partonic cross section and μ_R is renormalisation scale. The $\alpha_S(\mu_R)$ is renormalised coupling constant, Q is momentum transfer and μ_F is factorisation scale. To calculate the cross section including the non-perturbative contribution in the strong interaction, PDFs at the factorisation scale and the running coupling constant at the renormalisation scale are introduced. Following subsections describe above two techniques.

1.3.1 Running coupling constant and renormalisation scale

The renormalisation is a crucial technique of the quantum theory to avoid the ultraviolet divergence. Of course, the QCD is also the renormalisable theory, however, the on-shell renormalisation scheme which is independent to any energy scale is not available. The effective (renormalised) coupling constant α_S dependent on the renormalisation scale within the modified minimal subtraction ($\overline{\text{MS}}$) scheme [31] is widely used in QCD calculation. The renormalised coupling "running" logarithmically with the renormalisation scale is described by the Renormalisation Group Equation (RGE).

$$\mu_R^2 \frac{d\alpha_s}{d\mu_R^2} = \frac{d\alpha_s}{d\ln\mu_R^2} = \beta\alpha_s. \tag{1.45}$$

where the $\beta(\alpha_s)$ is the beta function.

$$\beta(\alpha_S) = -\alpha_S^2(b_0 + b_1\alpha_S + b_2\alpha_S^2 + b_3\alpha_S^3 + ...). \tag{1.46}$$

$$\beta_0 = \frac{33-2n_f}{12\pi}, \qquad \beta_1 = \frac{153-19n_f}{24\pi^2}, \qquad \beta_2 = \frac{2857-\frac{5033}{9}n_f+\frac{325}{27}n_f^2}{128\pi^3} \tag{1.47}$$

where n_f is the number of quark flavours considered as light($m_q < \mu_R$). The four-loop coefficient(β_3) is calculated in reference [32]. The 3-loop perturbative solution to the RGE is written as

$$\alpha_S(\mu_R^2) \simeq \frac{1}{b_0 t}\left(1 - \frac{b_1}{b_0^2}\frac{\ln t}{t} + \frac{b_1^2\left(\ln^2 t - \ln t - 1\right) + b_0 b_2}{b_0^4 t^2}\right), \quad t \equiv \ln\frac{\mu_R^2}{\Lambda^2}, \tag{1.48}$$

where $b_0 = \beta_N/\beta_0$ (N=1,2) and Λ with a dimension of energy is an energy scale at which the perturbatively defined coupling would normally diverge. The 4-loop solution is to be found in reference [33]. This running coupling decreases with μ_R growth, this effect known as asymptotic freedom of strong interactions. The α_S at a typical scale M_Z is measured in $n_f = 5$ scheme [34]. The value is

$$\alpha_S(M_{Z^0}) = 0.1184 \pm 0.0007 \tag{1.49}$$

with Λ corresponds to

$$\Lambda_{\overline{\text{MS}}}^{(5)} = (213 \pm 9)\ \text{MeV} \tag{1.50}$$

The mass of the quark is not measured directly, which means that there is a non-perturbative contribution to the mass. The quark mass is dependent on renormalisation scale μ_R with $\overline{\text{MS}}$ scheme. The non-perturbative scale of the chiral symmetry breaking scale is approximately 1 GeV. The light quarks (u, d and s), having masses lighter than this scale ($m_q < 1$ GeV) are treated non-perturbatively with typical renormalisation scale $\mu_R \approx 2$ GeV. For the heavy quarks (c, b and top: $m_q > 1$ GeV), α_s is measured at renormalisation scale equal to their mass $\mu_R = \overline{m}_q^2$. The RGE for the quark mass is given by

$$\mu_R^2 \frac{d\overline{m}_q\left(\mu_R^2\right)}{d\mu_R^2} = -\gamma\left(\alpha_S\left(\mu_R^2\right)\right)\overline{m}_q\left(\mu_R^2\right), \tag{1.51}$$

where γ is calculated to NNNLO and first order to third order are given as

$$\gamma\left(\alpha_S\left(\mu_R^2\right)\right) \equiv \sum_{r=1}^{\infty} \gamma_r \left(\frac{\alpha_S\left(\mu_R^2\right)}{4\pi}\right)^r \tag{1.52}$$

$$\gamma_0 = 4, \qquad \gamma_1 = \frac{202}{3} - \frac{20N_L}{9}, \qquad \gamma_2 = 1249 + \left(-\frac{2216}{27} - \frac{160}{3}\zeta(3)\right)N_L - \frac{140}{81}N_L^2, \tag{1.53}$$

where N_L is the number of quarks with the mass $< \mu_R$ and ζ is the Riemann zeta function.

1.3.2 Parton distribution function (PDF) and factorisation scale

The stability of the theory for the soft gluon emission (IR safety) and collinear emission (collinear safety) is important requirements. Our parton picture has a collinear singularity in the long lived states. Factorisation theorem allows us to divide short-distance perturbative part and long-distance non-perturbative part. The $\overline{\text{MS}}$ factorisation scheme splits with arbitrary factorisation scale μ_F. Then non-parturbative contribution below μ_F is considered in the parton distribution which is obtained from the experimental data. Several PDF sets are available as MSTW, CTEQ, NNPDF, HERAPDF etc. Main differences between the PDFs are parameterisation and input datasets. Generally, each group globally analyses various datasets obtained from fixed target lepton-nucleon experiments (SLAC, FNAL and CERN), electron-proton HERA experiments (H1 and ZEUS) and Tevatoron experiments (CDF and D0). The fit is performed at low scale (μ_0) and obtained PDF is evolved through the Dokshitzer-Gribov-Lipatov-Altarelli-Parisi (DGLAP) equation [35–37],

$$\mu_F^2 \frac{\partial f_{i/p}\left(x,\mu_F^2\right)}{\partial \mu_F^2} = \sum_j \frac{\alpha_s\left(\mu_F^2\right)}{2\pi} \int_x^1 \frac{dz}{z} \left\{ P_{i\leftarrow j}^{(1)}\left(z, \alpha_s\left(\mu_F^2\right)\right) f_{j/p}\left(\frac{x}{z}, \mu_F^2\right) \right\} \tag{1.54}$$

where $q_i\left(x,\mu_F^2\right)$ and $g\left(x,\mu_F^2\right)$ are the parton distribution function for quark and gluon with typical factorisation scale, and the splitting function $P_{i\leftarrow j}(x,\alpha_x)$.

$$P_{i\leftarrow j}\left(x,\alpha_s\left(\mu_F^2\right)\right) = P_{i\leftarrow j}^{(0)}(x) + \frac{\alpha_s\left(\mu_F^2\right)}{2\pi} P_{i\leftarrow j}^{(1)}(x) + \left(\frac{\alpha_s\left(\mu_F^2\right)}{2\pi}\right)^2 P_{i\leftarrow j}^{(2)}(x) + \ldots \tag{1.55}$$

The $P^{(i)}$ are calculated in up to NNLO (massless) perturbative QCD [38].

1.4 Phenomenology of the Higgs boson production in the LHC

Phenomenology of the Higgs is studied by Ellis et al [40]. The Higgs sector in the Standard Model Lagrangian is written as [3]

$$\mathscr{L} = -g_{Hff}\bar{f}fH + \frac{g_{HHH}}{6}H^3 + \frac{g_{HHHH}}{24}H^4 + \delta_V V_\mu V^\mu \left(g_{HVV}H + \frac{g_{HHVV}}{2}H^2\right) \tag{1.56}$$

with

$$g_{Hf\bar{f}} = \frac{m_f}{v}, \quad g_{HVV} = \frac{2m_V^2}{v} \tag{1.57}$$

$$g_{HHVV} = \frac{2m_V^2}{v^2}, \quad g_{HHH} = \frac{3m_H^2}{v}, \quad g_{HHHH} = \frac{3m_H^2}{v^2} \tag{1.58}$$

where $V = W^\pm$ or Z^0 and $\delta_W = 1,\ \delta_Z = 1/2$ [3]. The weak bosons ($W^\pm$ and Z^0) and heavy fermions have larger contribution to the Higgs production and decay.

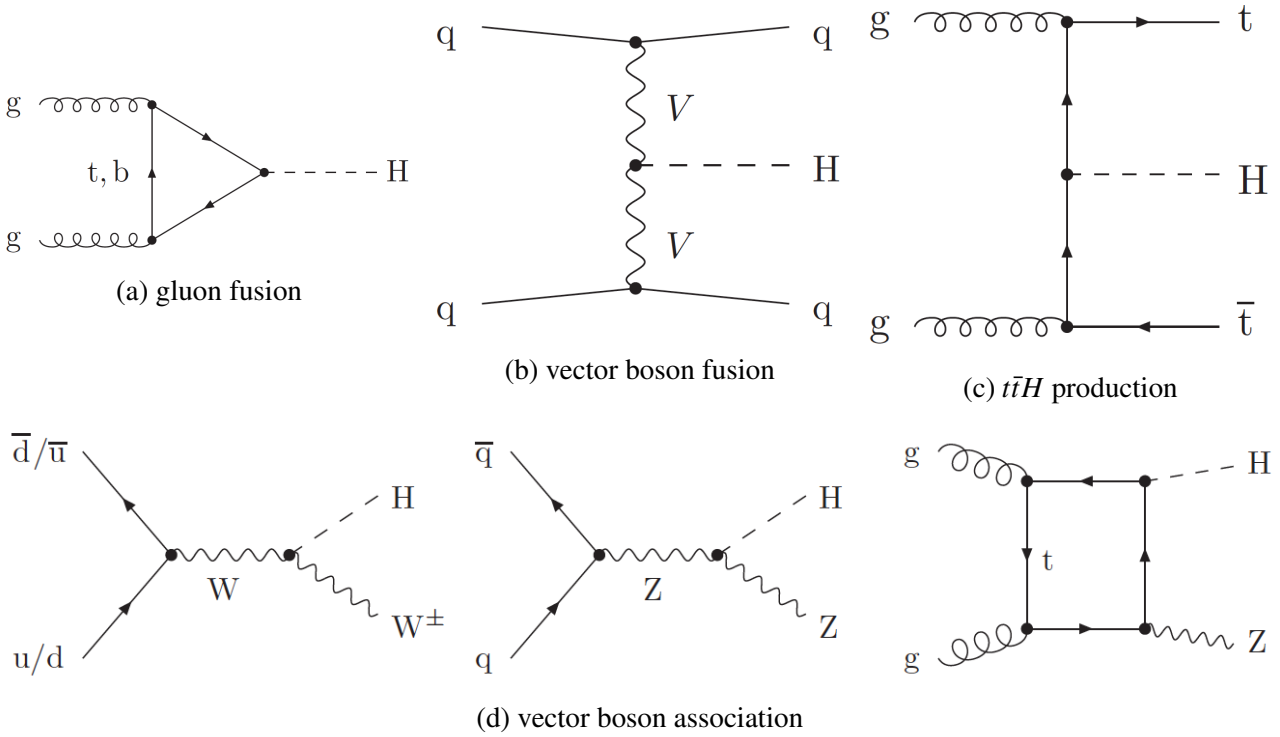

Figure 1.2: Feynman diagrams of the various Higgs production processes are shown. The vector boson association production includes a contribution from $gg \to Z^0 H$ diagram (NNLO) [39].

1.4.1 Higgs production

The dominant Higgs boson production mechanism at LHC is gluon fusion (Figure 1.2(a)). Since, gluons cannot directly couple to the Higgs boson, the top quark dominant quark loop contributes in this mechanism. The second dominant process is a vector boson fusion (VBF, Figure 1.2(b)). $W^{\pm}$ or Z^0 bosons radiated off from two quarks and Higgs boson is created by fusion of $W^{\pm}$ or Z^0 bosons. This process has a two hard jets produced in the forward region and the Higgs decay products are observed in the central region. The VBF process shows a significant contribution to $H \to \tau^+\tau^-$ analysis thanks to this characteristic signature while the cross section of VBF is about one order smaller than that of gluon fusion. Higgs production in association with $t\bar{t}$ (Figure 1.2(c)) has a very small cross section. However, this process allows us to measure the top Yukawa coupling. The weak boson associated productions ($W^{\pm}H$ and Z^0H, Figure 1.2(d)) are the most promising channel for $H \to b\bar{b}$ analysis at LHC. Tagging leptons from $W^{\pm}$ and Z^0 boson decay strongly suppresses the multi-jet background in the analysis. The cross section of this process is written as

$$\hat{\sigma}\left(q_i\bar{q}_j \to W^{\pm}H\right) = \frac{G_F^2 M_W^6 \left|V_{ij}\right|^2}{6\pi\hat{s}^2\left(1 - M_W^2/\hat{s}\right)^2}\lambda_{WH}^{1/2}\left[1 + \frac{\hat{s}\lambda_{WH}}{12M_W^2}\right], \tag{1.59}$$

where

$$\lambda_{WH} = 1 - \frac{2\left(M_W^2 + M_h^2\right)}{\hat{s}} + \frac{\left(M_W^2 - M_h^2\right)^2}{\hat{s}^2} \tag{1.60}$$

and V_{ij} is the Kobayashi-Maskawa matrix associated with the $q_i\bar{q}_j W^{\pm}$ vertex. The cross section with QCD radiative corrections is written as

$$\frac{d\sigma}{dq^2}\left(pp \to W^{\pm}H\right) = \sigma\left(pp \to W^{\pm *}H\right)\frac{G_F M_W^4}{\sqrt{2}\pi^2\left(q^2 - M_W^2\right)^2}\frac{|\mathbf{P}|}{\sqrt{q^2}}\left(1 + \frac{|\mathbf{P}|^2}{3M_W^2}\right) \tag{1.61}$$

to all orders in QCD [41], where $W^{\pm *}$ is a virtual $W^{\pm}$ with momentum q, G_F is the Fermi constant, M_W is a mass of $W^{\pm}$ boson and $|\mathbf{P}| = \sqrt{2}\lambda_{WH}^{1/2}/2$ is the momentum of the outgoing $W^{\pm}$ and H. The total cross section is obtained by integrating q^2. This Drell-Yan model gluon correction reduce the dependence of renormalisation

and factorisation scales. The remaining important dependence is the choice of the parton distribution function. The same procedure is available for Z^0H cross section. It is to be noted that there is an additional gluon fusion production $gg \to Z^0H$ for the Z^0H NNLO production. Also both $W^{\pm}H$ and Z^0H productions have top loop contribution in NNLO calculation. All the Higgs production cross sections are calculated to NNLO (+NNLL) QCD+ NLO EWK, which are shown in Figure 1.3(a).

1.4.2 Higgs decay

The dominant decay mode is $H \to b\bar{b}$. The partial width for bottom quark with massless approximation is calculated as

$$\Gamma\left(H \to b\bar{b}\right) = \frac{3G_F M_H}{4\sqrt{2}\pi} \bar{m}_b^2\left(M_H\right)\left[1 + \Delta_{QCD}\right], \tag{1.62}$$

where Δ_{QCD} is a QCD correction written as [42]

$$\Delta_{QCD} = 5.67\alpha_s\left(M_H\right) + 29.15\alpha_s^2\left(M_H\right) + 41.76\alpha_s^3\left(M_H\right) + \frac{m_b^2\left(M_H\right)}{M_H^2}\left(-6 - 40\alpha_S\left(M_H\right) - 87.72\alpha_S^2\left(M_H\right)\right), \tag{1.63}$$

The partial width for τ leptons are calculated similarly. The differences are QCD correction and a factor 3 smaller than the $H \to b\bar{b}$ decay since τ lepton is colour singlet. The partial decay width for boson pairs (W^+W^-, Z^0Z^0 and $\gamma\gamma$) are calculated with NNLO. For the W^+W^- and Z^0Z^0 cases, Higgs mass is below the di-boson mass threshold, hence one of the weak bosons is off-shell. The decay into $\gamma\gamma$ is achieved dominantly through a $W^{\pm}$ boson loop. The branching fractions for all processes are calculated as shown in Figure 1.3(b), and the full width as in Figure 1.3(c).
Finally, the cross section times branching fraction is calculated for accessible channels at the LHC and summarised in Figure 1.3(d).

1.5 Status of the Standard Model Higgs boson search at LHC

On 4 July 2012, the ATLAS and the CMS experiments announced thier independent observation of a new particle which is consistent with the Standard Model Higgs boson. Two experiment groups categorise the Higgs boson search based on the Higgs boson decay and production. The five decay channels: $H \to \gamma\gamma$, $H \to Z^0Z^0$, $H \to W^+W^-$, $H \to \tau^-\tau^+$ and $H \to b\bar{b}$, are separately studied. Additionally, $t\bar{t}H$ production process with various decay modes is independently analysed. The both groups reported comparable results in all the analysis channels.

1.5.1 Bosonic decay channels

The gluon fusion process predominantly contributes to the $H \to \gamma\gamma$ and $H \to Z^0Z^0$ channels. The main contributions to the $H \to W^+W^-$ channel are the gluon fusion and VBF processes. The fully leptonic decay channels have the largest and almost all sensitivity to the low mass Higgs boson analysis in the $H \to Z^0Z^0$ and $H \to W^+W^-$ channels. Thus, $H \to Z^+Z^- \to 4l$ and $H \to W^+W^- \to l\nu l\nu$ channels (where $l = e, \mu$) are ones of Higgs discovery. The dominant contribution of these channels are due to large top-quark Yukawa coupling in the loop in gluon fusion production and to large gauge coupling between weak bosons and Higgs boson in Higgs boson decay and VBF production. The $H \to \gamma\gamma$ and $H \to Z^+Z^- \to 4l$ channels have an excellent mass resolution. The $H \to \gamma\gamma$ takes advantage of the excellent mass resolution with the background estimated from the data by fitting the di-photon mass spectrum with a smooth polynomial and exponential function. The $H \to Z^0Z^0 \to 4l$ is the most cleanest channel in all the channels. The $H \to W^+W^- \to l\nu l\nu$ has a sensitivity despite its broad mass distribution thanks to the high production rate achieving a good S/N. Three bosonic decay channels contribute mainly to the discovery of the Higgs boson. The Higgs mass is measured in the $H \to \gamma\gamma$ and $H \to Z^0Z^0 \to 4l$ channels. The ATLAS result of the mass measurement is $m_H = 125.36 \pm 0.37\ (\text{stat}) \pm 0.18\ (\text{syst})$ GeV and the CMS result is $m_H = 125.03^{+0.26}_{-0.27}\ (\text{stat})^{+0.13}_{-0.15}\ (\text{syst})$ GeV (see Figure 1.5). The expected and observed significance to the Standard Model Higgs boson production obtained in the three bosonic decay modes are summarised in Table 1.1. The signal strengths of three bosonic channels are shown in Figure 1.4. The Standard Model Higgs boson has

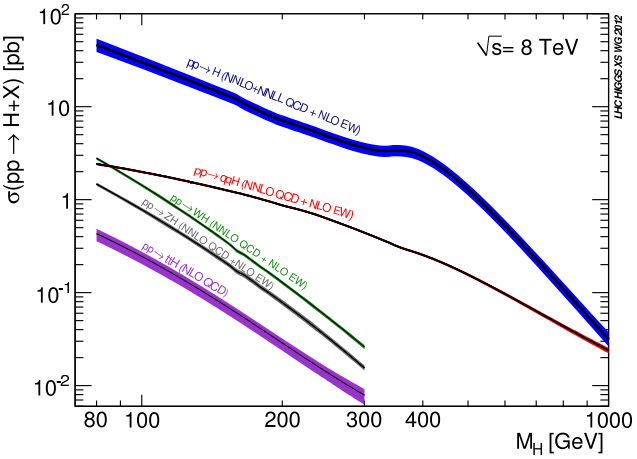

(a) Higgs production cross section

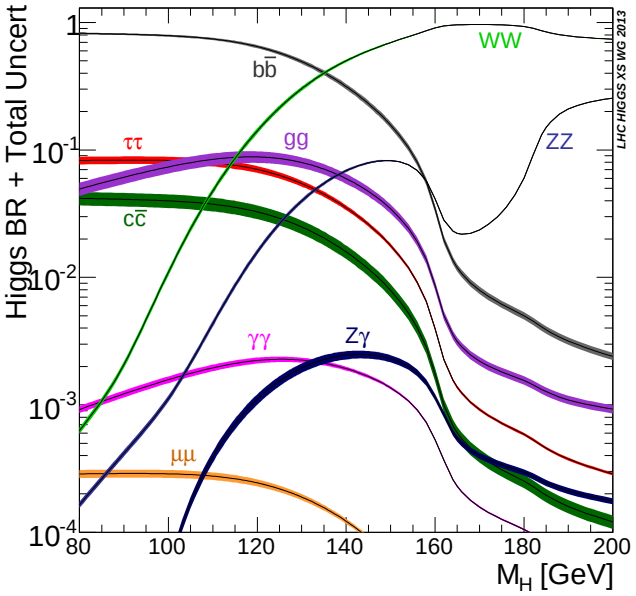

(b) Higgs branching ratio

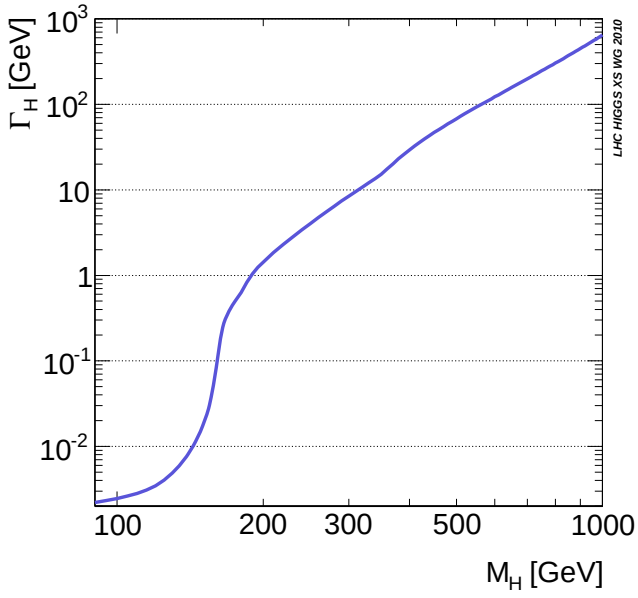

(c) Higgs full width

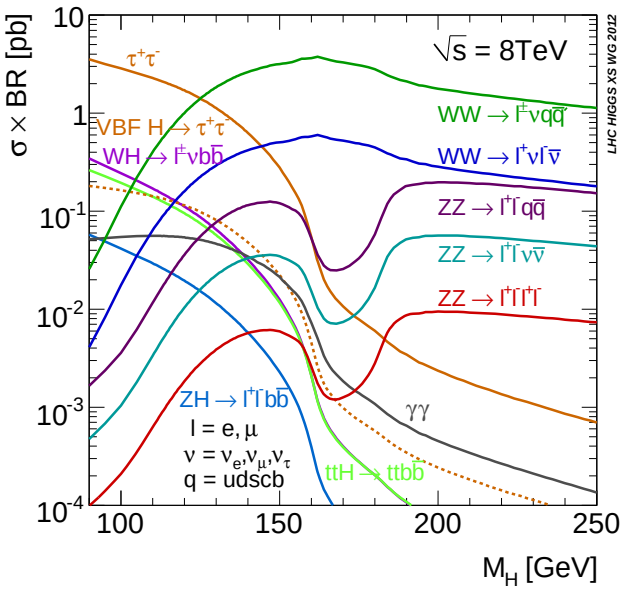

(d) $\sigma \times BR$ for analysis channels

Figure 1.3: (a) Production cross section, (b) branching ratio and (c) full width as function of Higgs boson mass. (d) The production cross section times branching ratio for main analysis channels [43].

spin 0 and positive parity. The spin and parity of the Higgs is measured in the two experiments. The ATLAS spin and parity studies provide evidence for spin-0 nature of the Higgs boson with positive parity being strongly preferred rejecting $J^P = 0^-, 1^+, 1^-$ and 2^+ models at 97.8%, 99.97%, 99.7% and 99.9% confidence levels, respectively (Figure 1.5). The CMS spin and parity results are also consistent with the spin-0 and positive parity nature of the Higgs boson.

1.5.2 Fermionic decay channels

The Yukawa coupling between the Higgs boson and the fermions are not described in the BEH mechanism. Actually, there is a beyond-the-Standard-Model scenario where higgs boson is a "Fermiphobic" (does not couple to the fermions). The existence of the Yukawa coupling is an extremely important nature of the Standard Model Higgs boson. The strength of the Yukawa coupling should be proportional to the fermion masses and the masses of the fermion themselves are free parameters in the theory. The Yukawa coupling measurements for all accessible fermion decay modes ($H\to\tau^+\tau^-$, $H\to b\bar{b}$ and $t\bar{t}H$) are absolutely imperative. The $H\to\tau^+\tau^-$ and $H\to b\bar{b}$ channels have high production rate compared to the $H\to\gamma\gamma$ and $H\to Z^0Z^0$ channels, however these analysis face on huge background from various physics processes. Additionally, the identification and energy measurement of the hadronic decay τ leptons and bottom quarks are technically difficult and have larger systematic uncertainties. The gluon fusion and VBF processes predominantly contribute to the $H\to\tau^+\tau^-$ channel. The two experiments observed an evidence for the Higgs boson to τ lepton coupling, see Table 1.1. In the $H\to b\bar{b}$ channel, both experiments focus on weak boson associate production, since leptons from weak boson decay strongly suppress the multi-jet background and drastically improve the trigger efficiency for the $H\to b\bar{b}$ events. This thesis describes the detail of the ATLAS $H\to b\bar{b}$ analysis which has ashieved the highest sensitivity, see Table 1.1. Chapters 2 and 3 describe the LHC and the ATLAS detector, respectively. The trigger, definition of the physics objects and event selection are given in Chapter 4, 5 and 6. The background modeling and signal analysis are detailed in Chapter 7 and 9, respectively, with Chapter 8 describing the Multivariate analysis, technique essential in this analysis. The results are given to Chapter 10 followed by the conclusion in Chapter 11.

Table 1.1: Summary of the expected and observed significance for the Higgs boson at $m_H = 125.36$ GeV for ATLAS data and $m_H = 125$ for CMS data. Both experiments show comparable results.

	ATLAS significance ($m_H = 125.36$ GeV)		CMS significance ($m_H = 125.0$ GeV)	
Decay mode	Expected	Observed	Expected	Observed
$H\to\gamma\gamma$	4.6 σ	5.2 σ	5.3 σ	5.6 σ
$H\to ZZ$	6.2 σ	8.1 σ	6.3 σ	6.5 σ
$H\to WW$	5.8 σ	6.1 σ	5.4 σ	4.7 σ
$H\to\tau\tau$	3.5 σ	4.5 σ	3.9 σ	3.8 σ
$H\to bb$	2.6 σ	1.4 σ	2.3 σ	2.0 σ

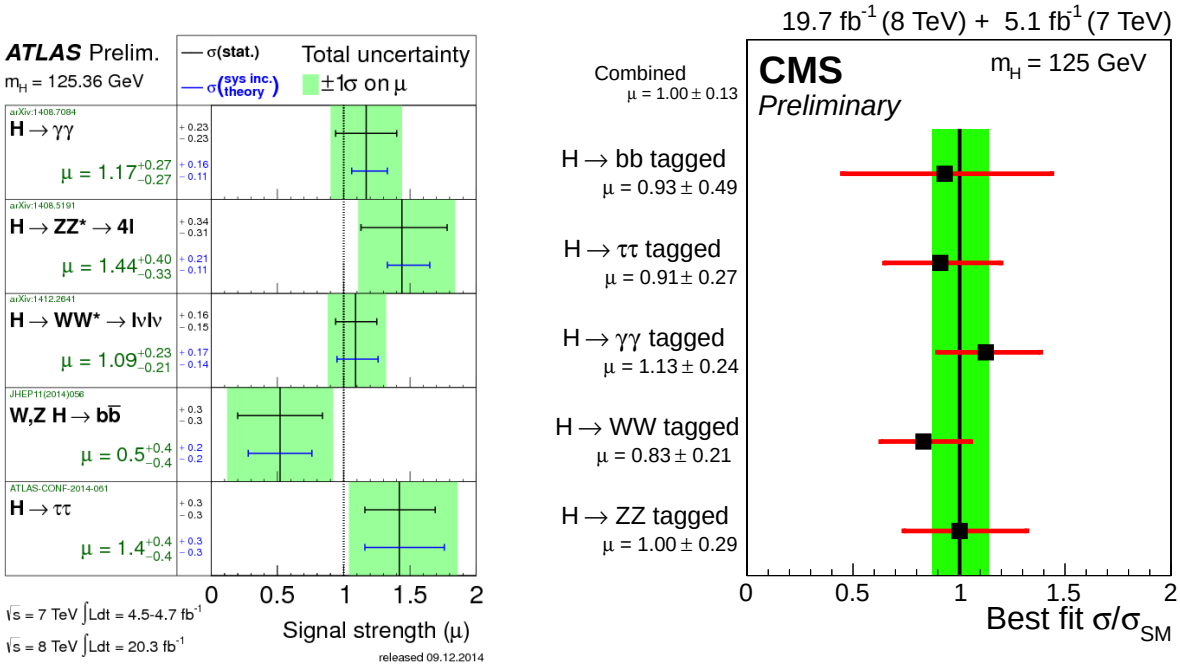

Figure 1.4: Measured Standard Model Higgs signal strengths $\mu = \sigma/\sigma_{SM}$ from ATLAS data (left) and CMS data (right). The green band in the CMS plots show the overall uncertainty on μ. The green bands in the ATLAS plot are the total uncertainty on μ shown for the individual decay mode. The horizontal bars indicate the ± 1 standard deviation uncertainties in the best-fit μ values for the individual decay modes. The CMS plot includes both statistical and systematic uncertainties. The ATLAS plot shows statistical and systematic uncertainties separately.

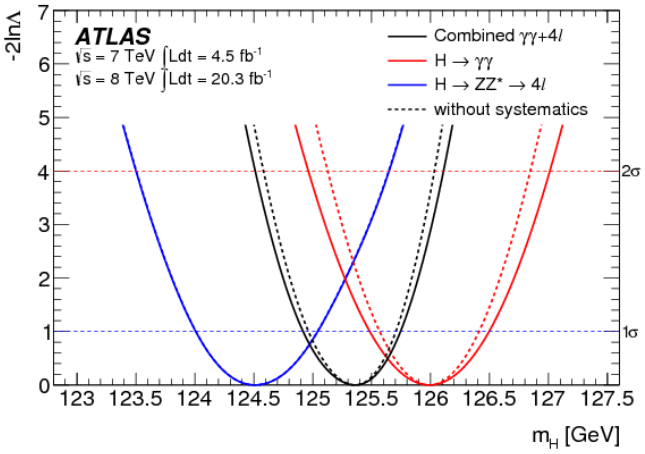

(a) ATLAS Higgs mass measurement

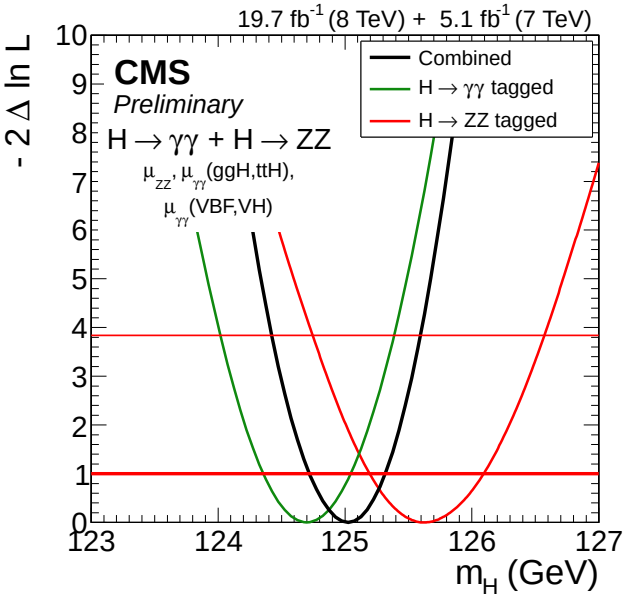

(b) CMS Higgs mass measurement

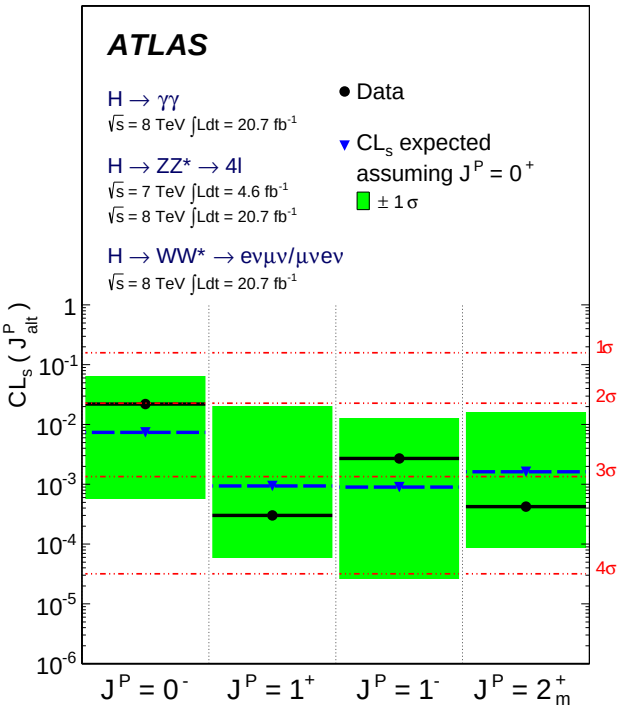

(c) ATLAS Higgs spin measurement

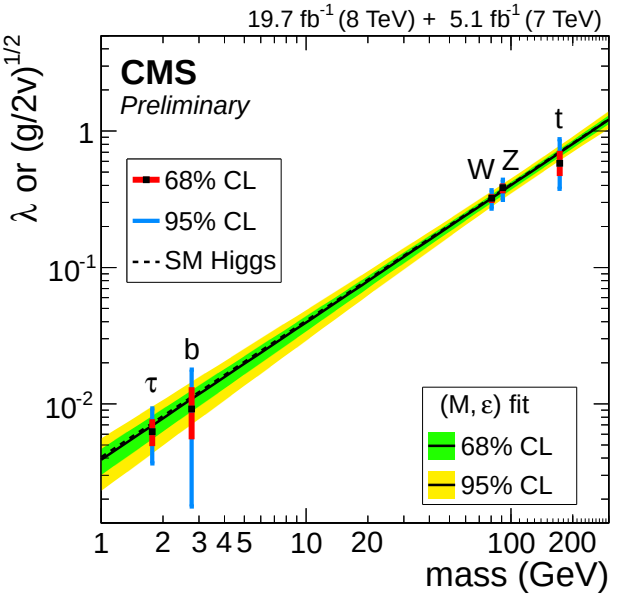

(d) CMS Higgs coupling measurement

Figure 1.5: (a), (b) Deviation of log-likelihood of observed and expected mass distributions calculated as a function of m_H for the individual $H\to\gamma\gamma$ and $H\to Z^0Z^{0*}\to 4l$ channels and their combination, where the signal strengths $\mu_{\gamma\gamma}$ and μ_{4l} are allowed to vary independently [44, 45]. (c) Expected (blue triangles with dashed lines) and observed (black circles with solid lines) confidence level CLs for alternative spin-parity hypotheses assuming a 0^+ signal. The green band represents the 68% CLs expected exclusion range for a signal with assumed 0^+ [46]. (d) For the fermions, the values of the fitted yukawa couplings λ are shown, while for vector bosons the $\sqrt{g/2v}$. The solid black line with 68% and 95% CL bands are taken from the fit to data [45].

Chapter 2

The Large Hadron Collider

2.1 History of LHC

The laboratory CERN operated the world's largest electron - positron synchrotron called LEP. It has a 27 kilometer circumference tunnel roughly 100 m underground. The LEP achieved $\sqrt{s} = 209$ GeV where the energy is limited by synchrotron radiation losses ($\propto (E_{beam}/\mathrm{m})^4$, m is the mass of the accelerating particle). CERN made a decision to build a proton - proton collider using LEP's existing tunnel. Since synchrotron radiation loss in the proton collider is much smaller ($< 10^{-12}$) than the electron collider, physics at higher energy regime can be explored. At that time Superconducting Super Collider (SSC) was planned in the U.S. (Unfortunately the SSC project was cancelled due to budget problem.) CERN's new hadron collider plan was the fastest and most economic way to achieve a multi TeV collider. It is named Large Hadron Collider (LHC). Now LHC is the world's largest and most powerful collider ever built. The first beam was circulated through the collider on 10 September 2008. The LHC achieved $\sqrt{s} = 1.18$ TeV per beam to become the world's highest energy particle accelerator on 30 November 2009. The LHC operated at $\sqrt{s} = 8$ (7) TeV and recorded around 20 (5) fb^{-1} of data until 2012.

2.2 Accelerator complex

The LHC is a last part of the CERN accelerator complex. Protons are produced in a Duoplasmatron source from hydrogen gasses. Then protons travel through 4 accelerators before reaching the LHC. First, protons are injected into LINAC2 and accelerated to 50 MeV. Next one is the Proton Synchrotron Booster (PSB), composed of four superimposed rings. It receives proton beams from LINAC2 at 50 MeV and accelerates them to 1.4 GeV. Third chain is Proton Synchrotron (PS) built as a 28 GeV proton accelerator in 1959. It was a world highest energy accelerator at that time. Now it accelerates protons to 25 GeV and it is responsible for providing 36 bunches of protons with 50 ns (design: 25 ns) spacing. Triplets of 36 bunches formed in the PS are injected into the Super Proton Synchrotron (SPS) where proton bunches are accelerated to 450 GeV. With the SPS (renamed from $Sp\bar{p}S$) discovered are W and Z bosons in 1983. Finally, the SPS injects the proton bunches into the LHC based on a bunch scheme (1374 bunches in 2012). The LHC accelerates them to an energy per beam of $E_p =$ 4.0 TeV (3.5 TeV) in the 2012 runs (2010 and 2011 runs). Once the desired collision status is reached, the stable beam condition is declared and data-taking proceeds by the experiments. The LHC will increase the beam energy up to $E_p = 6.5$ TeV (designed beam energy is $E_p = 7$ TeV) from next run.

2.3 Magnets to achieve TeV beam

There are a large variety of magnets in the LHC for accelerating, bending and focusing the beam. The biggest technological challenge was the dipole magnet for bending the beam. Required strength of the average magnetic field is $B = E_{beam}/(0.3 \times r)$, where r is the radius of the collider ($r = 4.3$ km). The LHC dipole magnets have to produce a magnetic field of 8.3 T to achieve designed beam energy $E_{beam} = 7$ TeV. The strength of the field is almost 2 times higher than the Tevatron (4.4 T). To achieve this very strong magnetic field, the magnet system uses superconducting NbTi Rutherford cables at 1.9 K cooled by high pressure superfluid helium. The dipole generates a maximum magnetic field of 8.3 T at supplied current of 11.850 A (designed). A two-in-one $\cos\theta$

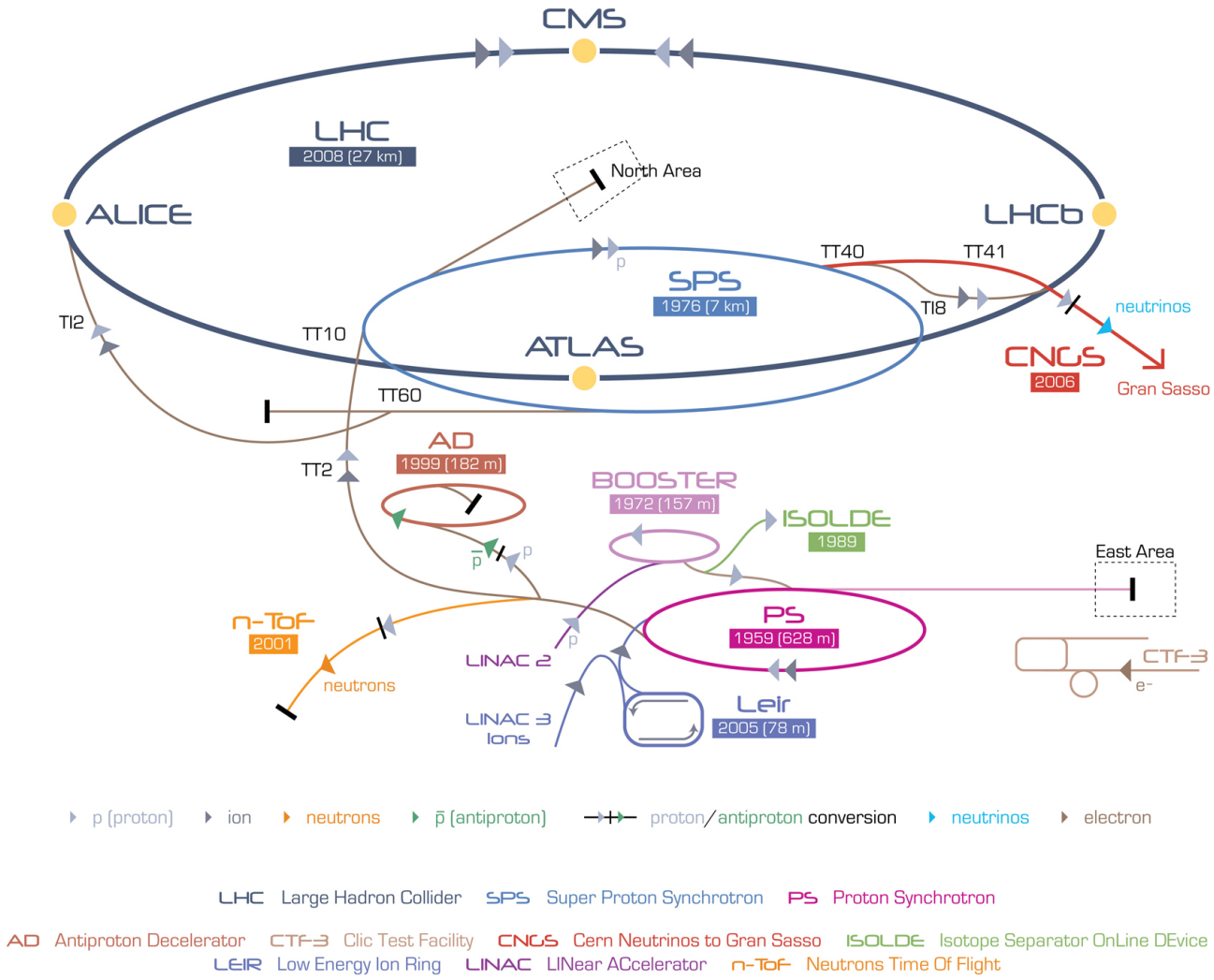

Figure 2.1: CERN accelerator complex [47]. The protons are first injected into LINAC2, where protons are accelerated to 50 MeV. They are successively injected into and accelerated by the PSB to 1.4 GeV, by the PS to 26 GeV, by the SPS to 450 GeV, and finally by the LHC where they are accelerated to 3.5 (4.0) TeV, which is half the designed beam energy of 7 TeV.

magnet design, shown in Figure 2.2, is employed to fit in the LEP tunnel. The same magnet provides magnetic fields in opposite directions in order to bend the two positively charged beams.

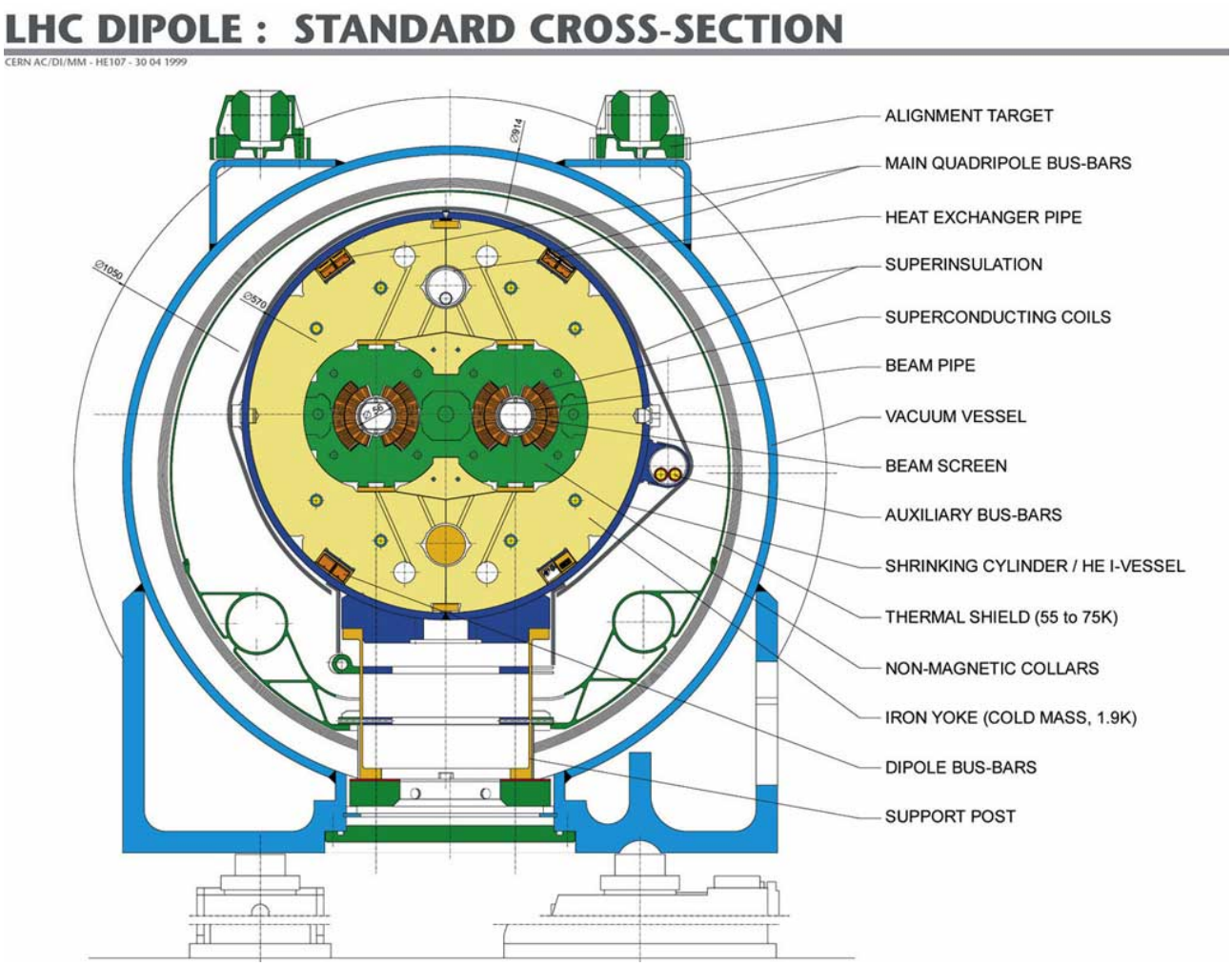

Figure 2.2: Cross section of a superconducting LHC dipole magnet. The two proton beams move in opposite directions through the two aperture beam-pipes [48].

2.4 Intensity of the beam

The luminosity is one of the most important parameters of the accelerator. The instantaneous luminosity $\mathscr{L}$ is the proportionality factor between the event yield rate and cross section as $dN/dt = \mathscr{L}\sigma$, defined as

$$\mathscr{L} = \frac{N_p^2 k_b f}{4\pi\sigma_x^*\sigma_y^*}\ [\mathrm{cm}^{-2}\mathrm{s}^{-1}], \tag{2.1}$$

where

- N_p is the number of protons per bunch
- k_b is the number of bunches
- f $[s^{-1}]$ is the revolution frequency
- σ_x^* [cm] is the horizontal beam size at interaction point

- σ_y^* [cm] is the vertical beam size at interaction point

Assuming round beams and equal values of the beta function for both beams, this equation is also expressed

$$\mathscr{L} = \frac{N_p^2 k_b f \gamma}{4\pi\varepsilon_n \beta^*} \mathscr{F} \ [\mathrm{cm}^{-2}\mathrm{s}^{-1}], \tag{2.2}$$

where

- ε_n [cm] is the normalised rms emittance
- β^* [cm] is the value of the beta (amplitude) function at the interaction point
- $\mathscr{F}$ is the geometrical luminosity reduction factor due to crossing angle, expressed as

$$\mathscr{F} = \frac{1}{\sqrt{1+\phi_c^2}} = \frac{1}{\sqrt{1+\left[\frac{\theta_c \sigma_z}{2\sigma^*_{trans}}\right]^2}} \tag{2.3}$$

where ϕ_c is known as the Piwinski angle, θ_c is the full crossing angle of the two beams at the interaction point, σ_z is the bunch length and σ^*_{trans} is the transverse beam size. To achieve high luminosity, LHC has to make low emittance beams of high population protons and collide them at high frequency at locations where the beam optics provides as low value of the amplitude functions as possible. Table 2.4 summarises the LHC status in 2012. The LHC recorded $\mathscr{L} \sim 7.7 \times 10^{33}\ cm^{-2}s^{-1}$ in 2012, which is 70% of the design luminosity$10^{34}\ cm^{-2}s^{-1}$. This excellent performance is a result of the good beam quality delivered by the injectors. The injector complex delivered 150% of nominal number of protons per bunch with a 2/3 of nominal emittance beam.

Parameter	Value in 2012	Design value
Beam energy [TeV]	4	7
β^* at IP [m]	0.6	0.55
Bunch spacing [ns]	50	25
Number of bunches	1374	2808
Average proton intensity per bunch [protons per bunch]	1.6-1.7$\times 10^{11}$	1.15$\times 10^{11}$
Normalised emittance at start of fill [mm.mrad]	2.5	3.75
Peak luminosity [$\mathrm{cm}^{-2}\mathrm{s}^{-1}$]	7.7$\times 10^{33}$	1$\times 10^{34}$
Max. mean number of events per bunch crossing	≈ 50	19
Stored beam energy [MJ]	≈ 140	362

Table 2.1: Summary of the LHC performance achieved in 2012 and designed values [49].

The total number of events with cross-section σ for an integrated luminosity L_{int} in a time period t is given as

$$N_{evt} = \sigma L_{int} = \sigma \int^t \mathscr{L} dt. \tag{2.4}$$

The integrated luminosity evolution is shown in Figure 3.15 for pp collisions at centre-of-mass energy of 7 and 8 TeV.

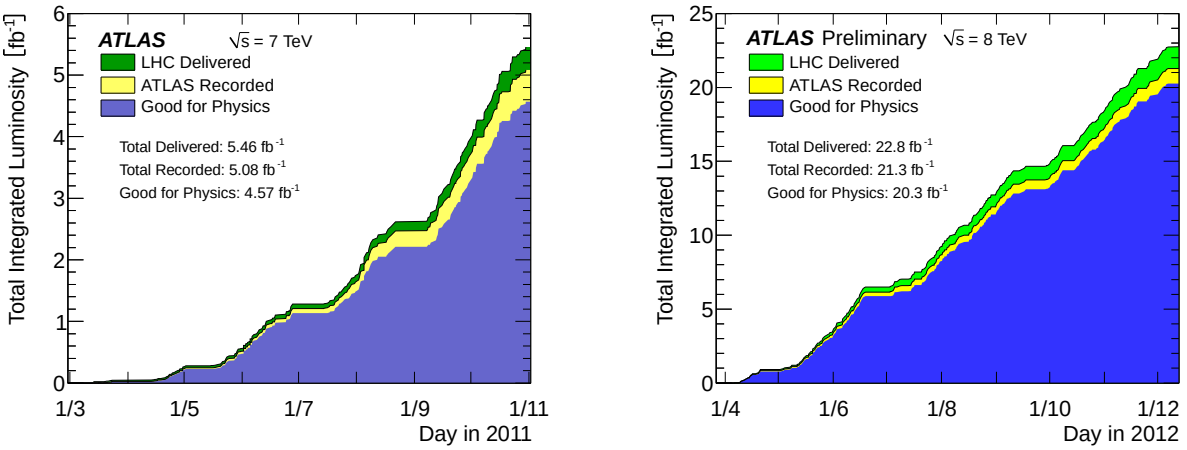

Figure 2.3: Integrated luminosity evolution defined as delivered by the LHC (green), recorded by the ATLAS (yellow) and certified to be good quality data (blue) for pp collisions at centre-of-mass energy of 7 TeV (left) and 8 TeV (right) [50].

Chapter 3

The ATLAS Detector

3.1 ATLAS coordinate system

The ATLAS reference system is a cylindrical coordinate system. The origin of the coordinate system is defined as the nominal interaction point which coincides with the centre of the ATLAS detector. The z axis is oriented parallel to the beam line and x-y plane is transverse plane to the beam line. The anti-clockwise beam direction defines the positive side of z axis and the x axis is defined as pointing from the interaction point to the centre of the LHC ring. The azimuthal angle ϕ is the angle in the x-y plane measured from the x axis. The polar angle θ is the angle from the z axis. The rapidity is defined as

$$y = 0.5 \times \ln\left(\frac{E + p_z}{E - p_z}\right), \tag{3.1}$$

where E is the energy and p_z is the momentum in z direction. The pseudorapidity is calculated by rapidity with massless approximation:

$$\eta = -\ln\left[\tan\left(\frac{\theta}{2}\right)\right]. \tag{3.2}$$

The pseudorapidity is a very useful in the collider experiment, since the particle multiplicity is approximately constant as a function of η. The distance ΔR in the pseudorapidity-azimuthal angle space is defined as $\Delta R = \sqrt{(\Delta\eta)^2 + (\Delta\phi)^2}$. This coordinate system is used throughout in this thesis.

3.2 Overview of the ATLAS detector

The ATLAS is designed as a "general purpose detector". The general purpose detector has a wide coverage of the solid angle composed of various types of detector components to identify and measure all stable particles, such as electrons, muons, photons, charged hadrons (protons, charged pions, etc.) and neutral hadrons (neutrons) by a combination of all the detector components. Other unstable particles decay into stable particles before reaching the detector and they are indirectly reconstructed from measured stable particles. Figure 3.1 shows a schematic view of particle indentification in the ATLAS detector. The tracker measures the momentum of charged particles (electrons, muons and charged hadrons) in a magnetic field. The electromagnetic calorimeter can measure the energy of electrons and photons. The hadronic calorimeter can measure the energy of charged hadrons and neutral hadrons. The muon chamber measures the momentum of muons in a magnetic field. The tracker installed innermost layer of the detector, inner detector measures the particle energy before they enter the calorimeters. All the particles except muons and neutrinos are absorbed by the calorimeter. Muons record hits on the tracker and also deposit a part of energy in the calorimeter. But the momentum/energy resolution for high momentum muons is limited. A dedicated detector is to measure the momentum of muons outside of the calorimeter, a muon spectrometer.

The reconstructed objects are categorized as photon, electron, muon, tau and jet. High energy quarks and gluons are reconstructed as a collimated flow of neutral and/or charged hadrons known as "jet". Leptonically decay tau

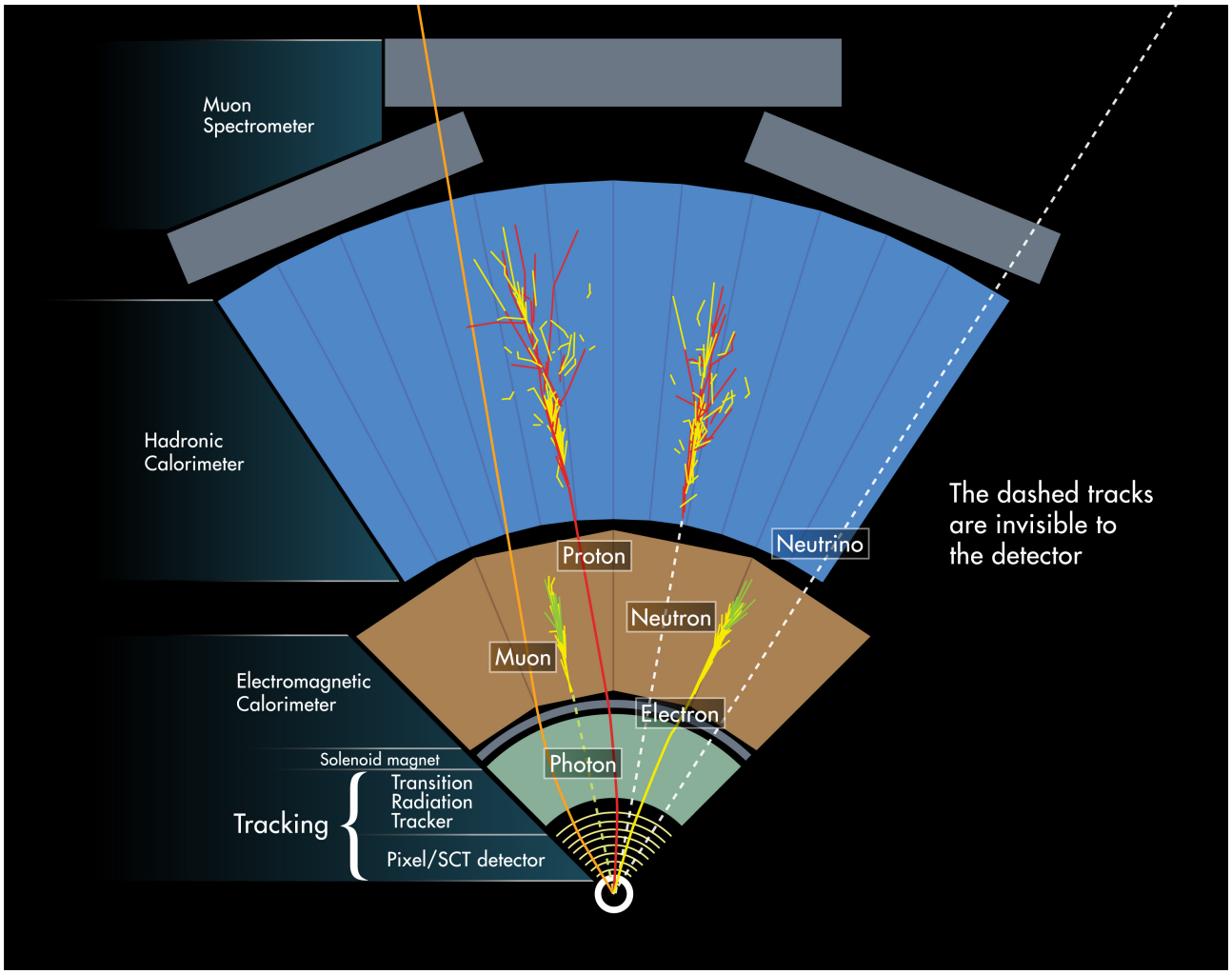

Figure 3.1: Illustration of identification of various particles with the ATLAS detector [51]. Muons record hits on the tracker and muon spectrometer. Photons do not record a hit on the tracker but make a cluster in the EM calorimeter. Electrons make hits on the tracker and deposit energy in the EM calorimeter. Protons and charged hadrons make hits on the tracker and deposit energy in the hadron calorimeter. Neutrons deposit energy in the hadron calorimeter without recording hits on the tracker.

leptons are reconstructed associated with an electron or muon. Hadronically decay tau leptons are reconstructed as a narrow jet: "reconstructed tau" refers to this hadronically decay tau lepton. Neutrinos are stable enough but they are not detectable due to tiny interaction with the detector materials. Fortunately, in the transverse plane, all the momentum sum in one hard collision is conserved. So the direction and momentum(equal to energy) of the neutrino in the transverse plane is calculated as a deficit from other reconstructed objects. Such a missing momentum in the transverse plane is called "missing transverse energy (MET, $E_{\mathrm{T}}^{\mathrm{miss}}$)". If there are more than two neutrinos, $E_{\mathrm{T}}^{\mathrm{miss}}$ is equal to the vector sum of all neutrinos. Figure 3.2 shows an overview of the ATLAS detector. The ATLAS detector has a cylindrical shape similar to other general purpose detectors. Each type of detector components has the sub-detectors to maximise the performance and divided into barrel and end-cap regions to cover the full η range. Table. 3.1 shows a final goal of the ATLAS detector performance. This section describes the detail how the ATLAS detector has achieved the excellent performance.

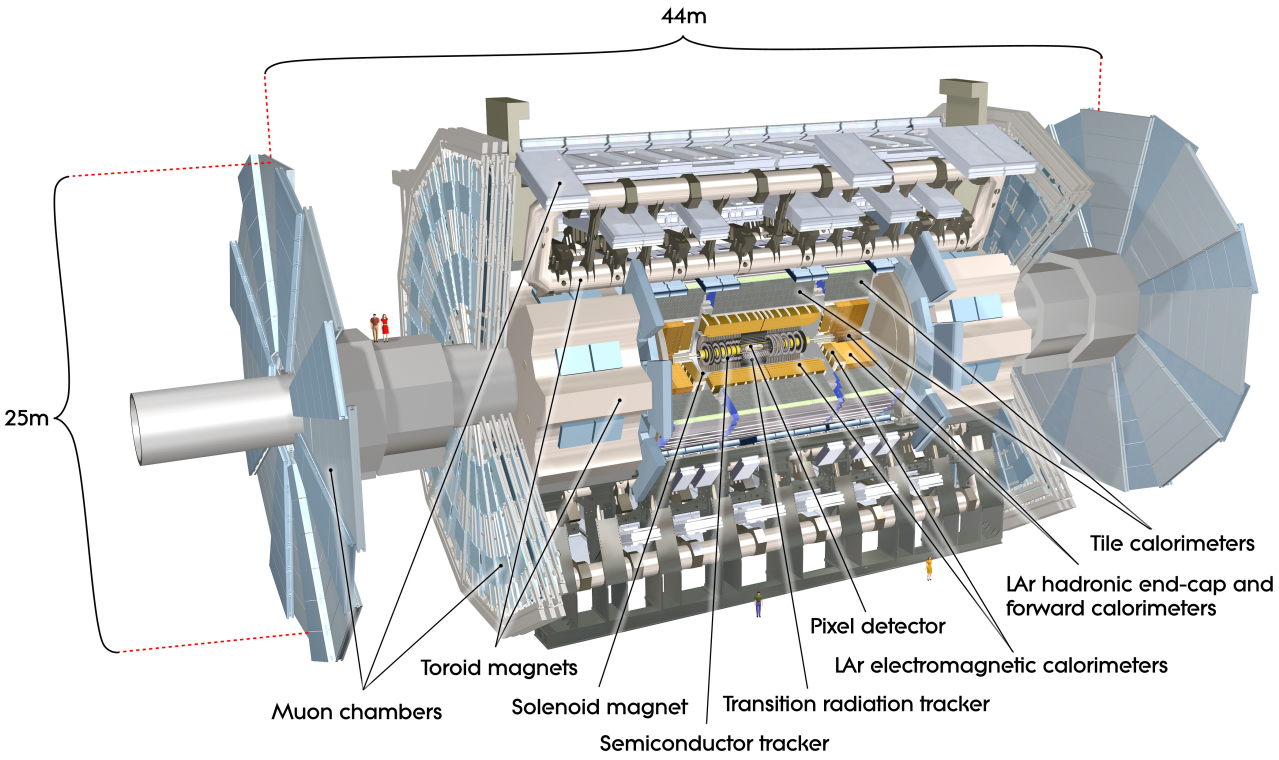

Figure 3.2: Illustration of the ATLAS detector [52]. Some of the detector names are labelled.

Table 3.1: Designed ATLAS detector performance and the η coverage of each detector [53]. Quadrature sum of the two terms is indicated by $\oplus$. P_T in GeV and E in GeV.

Detector component	Required resolution	η coverage	
		Measurement	Trigger
Tracking	$\sigma_{p_T}/p_T = 0.05\%\ p_T \oplus 1\%$	± 2.5	-
EM calorimetry	$\sigma_E/E = 10\%/\sqrt{E} \oplus 0.7\%$	± 3.2	± 2.5
Hadronic calorimetry (jets)			
barrel and end-cap	$\sigma_E/E = 50\%/\sqrt{E} \oplus 3\%$	± 3.2	± 3.2
forward	$\sigma_E/E = 100\%/\sqrt{E} \oplus 10\%$	$3.1 < \lvert\eta\rvert < 4.9$	$3.1 < \lvert\eta\rvert < 4.9$
Muon spectrometer	$\sigma_{p_T}/p_T = 10\%\ at\ p_T = 1$ TeV	± 2.7	± 2.4

3.3 Inner detector

When a charged particle with a momentum p transverses a magnetic field B, its trajectory is bent by the Lorentz force ($F = q(\mathbf{v} \times \mathbf{B})$). If the magnetic field $\mathbf{B}$ [T] is applied parallel to the beam axis, the momentum projection to the transverse plane p_T is written as p_T [GeV/c] $= 0.3BR$, where R [m] is a radius of the curvature. The solenoid magnet in the ATLAS detector produces 2-Tesla magnetic field parallel to the beam axis. The inner detector (ID) measures the trajectory of the charged particle and calculate the momentum. The sagitta $s \approx \frac{(0.3L^2B)}{8p_T}$ where L is the lever length of the sagitta measurement, is useful to calculate the momentum rather than the radius of the curvature, since it is measurable with high accuracy. In the case of N equidistant position measurements, the relative momentum resolution is written as

$$\frac{\sigma(p_T)}{p_T} = \frac{\sigma(x)p_T}{0.3BL^2}\sqrt{\frac{720}{N+4}} \text{ for N} \geq\sim 10 \tag{3.3}$$

where $\sigma(x)$ [m] is the uncertainty of single position measurement [54] and L in unit of [m]. Thus, the momentum resolution of the ID is dependent on the spatial resolution, number of measurements, strength of the magnetic field and the lever length of the tracking detector. The ATLAS ID has $B = 2$ T and $L \sim 1.1$ m. Assuming $N = 10$, $\sigma(x)$ should be less than ~ 50 μm to achieve the required performance. Actually, the resolution of ATLAS inner detector is better than ~ 50 μm. The relative error due to multiple scattering is independent to the momentum. In high p_T region, the error due to the multiple scattering is relatively smaller. Generally requirements for the tracking detector are to measure the position with high precision as well as to reduce the materials constructing the detector as much as possible. To achieve this requirement, there are three sub-detectors in the ID, pixel detector installed innermost near the beam pipe, the semiconductor tracker (SCT) and outermost transition radiation tracker (TRT). When a relativistic charged particle transverses the matter, the charged particle interacts predominantly with the electrons of the atoms in the material. The energy loss due to the interaction is described by the Bethe-Bloch equation [3].

$$-\left\langle \frac{dE}{dx} \right\rangle = Kz^2\frac{Z}{A}\frac{1}{\beta^2}\left[\frac{1}{2}\ln\frac{2m_ec^2\beta^2\gamma^2T_{max}}{I^2} - \beta^2 - \frac{\delta}{2}\right] [\text{MeVg}^{-1}\text{cm}^2], \tag{3.4}$$

where $K/A = 4\pi N_A r_e^2 m_e c^2/A = 0.307075$ MeV g^{-1}cm^2 for A= 1 g mol^{-1}, A is atomic mass of absorber, Z is atomic number of absorber, N_A is Avogadro's number, m_e is electron mass, r_e is the classical electron radius, I is mean excitation energy, z is charge of incident particle, β and γ are velocity and Lorentz factor in relativistic theory, δ is density correction, and T_{max} is the maximum kinetic energy which can be impacted to a free electron in a single collision given by

$$T_{max} = \frac{2m_ec^2\beta^2\gamma^2}{1 + 2\gamma m_e/M + (m_e/M)^2} \tag{3.5}$$

where M is mass of incident particle. This equation is valid for the particle which have mass $M > m_\mu$ and its momenta $0.05 < \beta\gamma < 500$. The Pixel and SCT use semiconductor technology to achieve excellent spatial resolution. In the semiconductor, deposited energy creates movable electron-hole pairs with the number proportional to the particle's energy loss. An externally applied electric field collects the charge carriers generating a signal. TRT is a gaseous detector utilising transition radiation to separate electrons and pions.

The structure of the ID is illustrated in Figures 3.3 and 3.4.

3.3.1 Solenoid magnet

The ATLAS central solenoid magnet produces a longitudinal magnetic field parallel to the z-axis. The solenoid produces a 2-Tesla magnetic field with minimising the material. It is installed between the ID and electromagnetic calorimeter. To reduce the material, the solenoid shares the vacuum enclosure with the electromagnetic calorimeter. The radius is 1.247 m and the length is 5.283 m in z. The conductor consists of Rutherford type NbTi/Cu cable stabilised by high strength aluminium (Ni, Zn doped). It is indirectly cooled to 4.5 K by helium-II. The cooled superconducting coil produces a 2-Tesla magnetic field at 7730 A. Two quench protection systems are applied for the safety. If a quench is detected, quench protection heaters are fired up and pure aluminium (99.9998%) strips immediately propagate the quench in the coil in axial direction. The magnetic

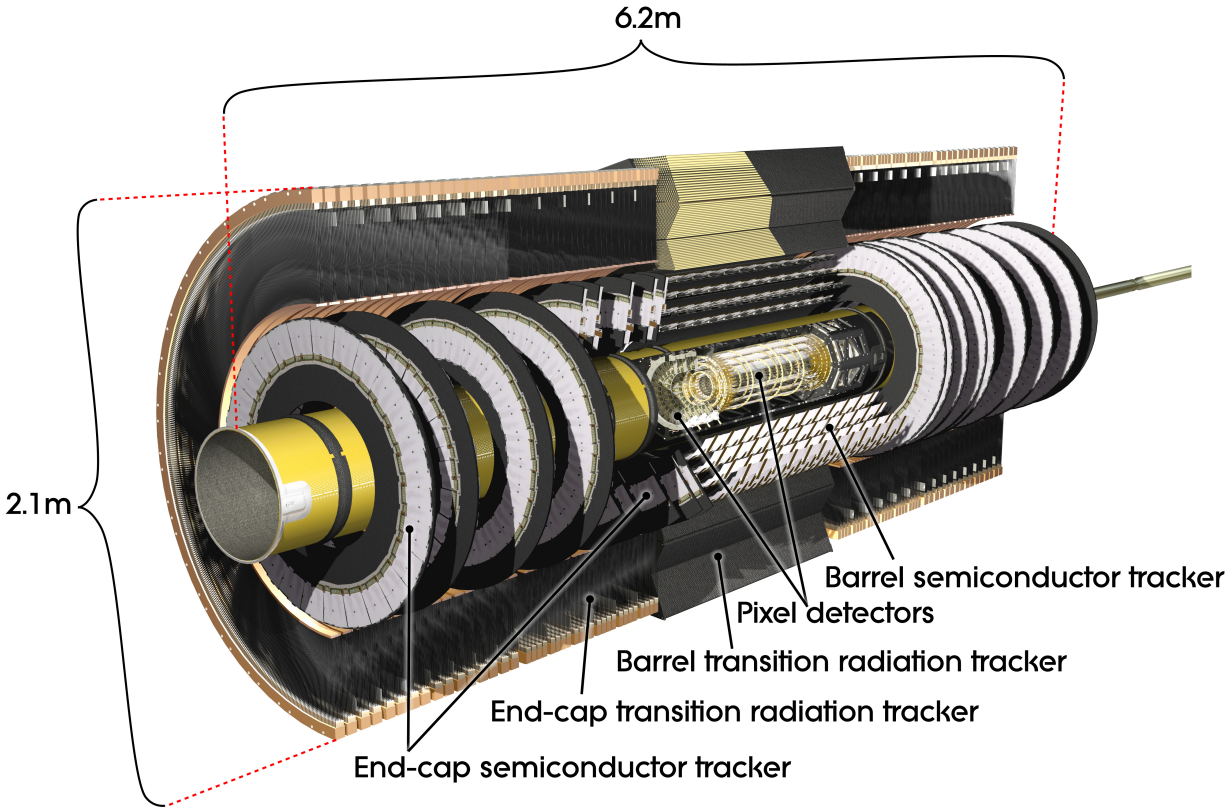

Figure 3.3: Illustration of the ATLAS Inner Detector [55].

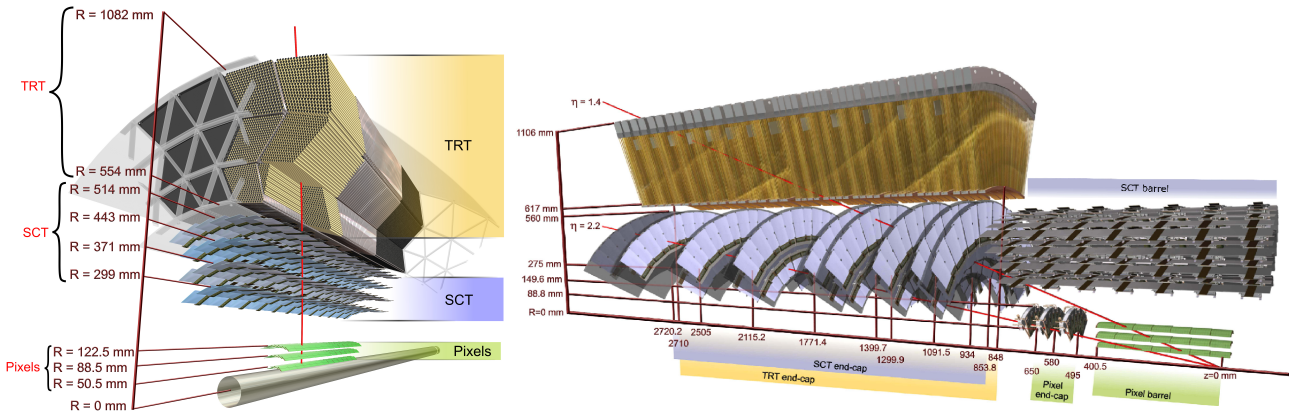

Figure 3.4: Cross section of the ATLAS Inner Detector. The barrel structure (left) and one side the ID including the end-cap (right) [55].

Table 3.2: Dimensions of the ATLAS Inner Detectors. Each detector consists of barrel part (cylindrical layers) and two end-cap parts (disks) [53].

Item		Radial extension (mm)	Length (mm)
Overall ID envelope		$0 < R < 1150$	$\|Z\| < 3512$
Beam-pipe		$29 < R < 36$	
Pixel	Overall envelope	$45.5 < R < 242$	$\|Z\| < 3092$
3 cylindrical layers	Sensitive barrel	$50.5 < R < 122.5$	$\|Z\| < 400.5$
3×3 disks	Sensitive end-cap	$88.8 < R < 149.6$	$495 < \|Z\| < 650$
SCT	Overall envelope	$255 < R < 549$ (barrel)	$\|Z\| < 805$
		$251 < R < 610$ (end-cap)	$810 < \|Z\| < 2797$
4 cylindrical layers	Sensitive barrel	$299 < R < 514$	$\|Z\| < 749$
2×9 disks	Sensitive end-cap	$275 < R < 560$	$839 < \|Z\| < 2735$
TRT	Overall envelope	$544 < R < 1082$ (barrel)	$\|Z\| < 780$
		$617 < R < 1106$ (end-cap)	$827 < \|Z\| < 2744$
73 straw planes	Sensitive barrel	$563 < R < 1066$	$\|Z\| < 712$
160 straw planes	Sensitive end-cap	$644 < R < 1004$	$848 < \|Z\| < 2710$

Table 3.3: The spatial resolution, the size of one channel, number of hits per track, total number of channels, and total area of the three ID sub-detectors [53].

Item	resolution (μm)	size of channel	Hits/track	# of channels	total area (m^2)
Pixel	12×115	$50\ \mu\text{m} \times 400\ \mu\text{m}$	3	80.4 million	1.7
SCT	12-16 $\times$ 580	57-90 μm $\times$ $\sim$12 (cm)	8	6.3 million	60
TRT	170 per straw	4 (mm, diameter)	$\approx$30	350,000	12 (m^3 volume)

field is well measured by probes operated under the principles of nuclear magnetic resonance (NMR) and the Hall effect. The relative error on the track sagitta $\delta s/s$ due to the field uncertainty varies from 0.023% in low rapidity to 0.12% in high rapidity regions.

3.3.2 Pixel Detector

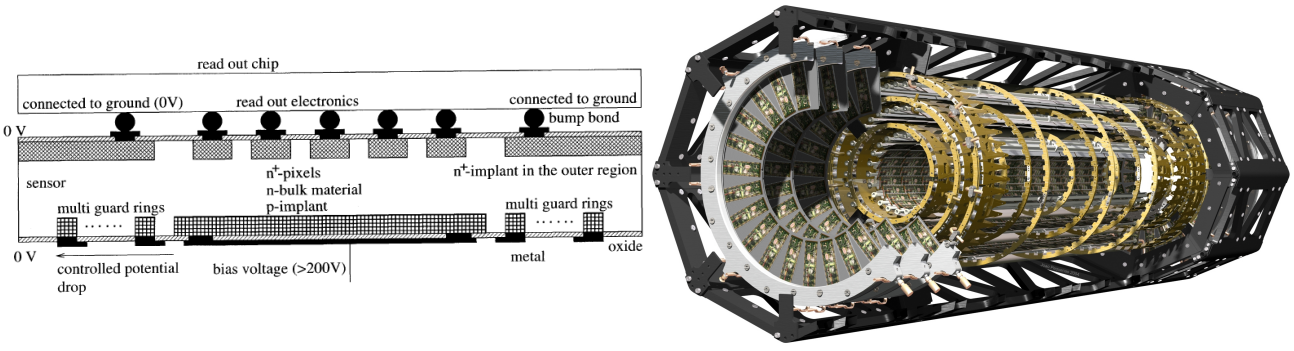

Figure 3.5: Cross section view of a pixel sensor (left) [56] and schematic view of the pixel detector (right) [57].

The pixel detector 3.5 is the innermost detector of the ID system. It is designed to provide three precision points for a charged track up to $\eta = 2.5$ with a resolution of 12 μm in the r-ϕ plane and 115 μm in the z direction. Thanks to this good resolution, especially in z direction, the pixel detector allows us to reconstruct the event vertex efficiently also in high pile up condition. The ATLAS system can tag the bottom-quark jet (b-tagging). Since the bottom quark has a lifetime $c\tau_b \approx 470\ \mu$m longer compared to other unstable particles. In this thesis, b-tagging has been developed to drastically suppress the light jet background and to improve

the sensitivity to the Higgs boson. In order to achieve this performance, first layer of the detector (b-layer) is located close (5 cm) to the beam axis. The lifetime dose of the b-layer is 500 kGy expected to reach in five years of LHC operation. The pixel sensors (Figure 3.5) employ n+implants on a 250 μm thick high resistivity n-bulk substrate with oxygenation enriched to enhance the radiation hardness. It can work under a partially depleted condition after the substrate is type inverted. A multiple guard ring structure allows its operation at fully depletion voltage up to 600 V. One module is 2 cm $\times$ 6 cm in area with 46,080 pixels, each pixel being 50 μm $\times$ 400 μm (600 μm for long pixels). Pixels are connected to 16 front-end (FE) Application Specific Integrated Circuits (ASIC) chips using fine pitch solder (Pb/Sn) or Indium bump bonding. The FE chips work over 300 kGy of radiation corresponding to ten years of LHC operation. The FE chips are connected to a module-control chip (MCC) and they communicate with the off-detector read-out drivers (RODs) via optical fibre links. The modules are assembled into 3 cylindrical layers for the barrel region and 3 layers for each end-cap region. The modules are overlapped on the support structure to diminish the inactive area. All modules are cooled at -7°C by an evaporative C_3F_8 cooling system to suppress the noises and radiation damage. The thickness of each layer is about 1.7% of a radiation length at normal incidence.

3.3.3 Semi-Conductor Tracker (SCT)

The Semi-Conductor Tracker (SCT) is a silicon microstrip detector installed in the middle section of the inner detector. It is designed to provide eight precision points for a charged track up to $\eta = 2.5$ with a resolution of 17 μm in the r-ϕ plane and 580 μm in the z direction. The design of the barrel module and end-cap modules are different. One barrel module (Figure 3.6) consists of four 6.38$\times$6.4 mm^2 p-on-n single sided sensors with 770 readout strips (768 active) arranged at an 80 μm pitch. Two sensors are glued on each side of a 380 μm thick thermal pyrolytic graphite (TPG) base board to make a 128 mm (126 mm active with a 2 mm dead space) long module, with both sides of the strips rotated by $\pm$20 mrad with respect to the long axis of the module. The spatial resolution in z direction is given as $\sigma_z = \sigma_{strip}/\sin(40\text{ mrad}) = 580$ μm with ($\sigma_{strip} = 80/\sqrt{12} = 23$ μm) and in r-ϕ plane is calculated as $\sigma_{r-\phi} = \sigma_{strip}/\sqrt{2} = 17$ μm. The signals are digitised by 128ch front-end ASIC named ABCD3T mounted bridging over the sensor and the data are transmitted via optical transmitter. The structure of the end-cap module is similar to the barrel module but use tapered strips with varied strip pitch (50-90 μm). The end-cap modules cover the η range up to 2.5 with a combination of short modules (6-7 cm) strip length and long modules (12 cm) strip length. The modules are operated at -7°C by a C_3F_8 evaporative cooling system.

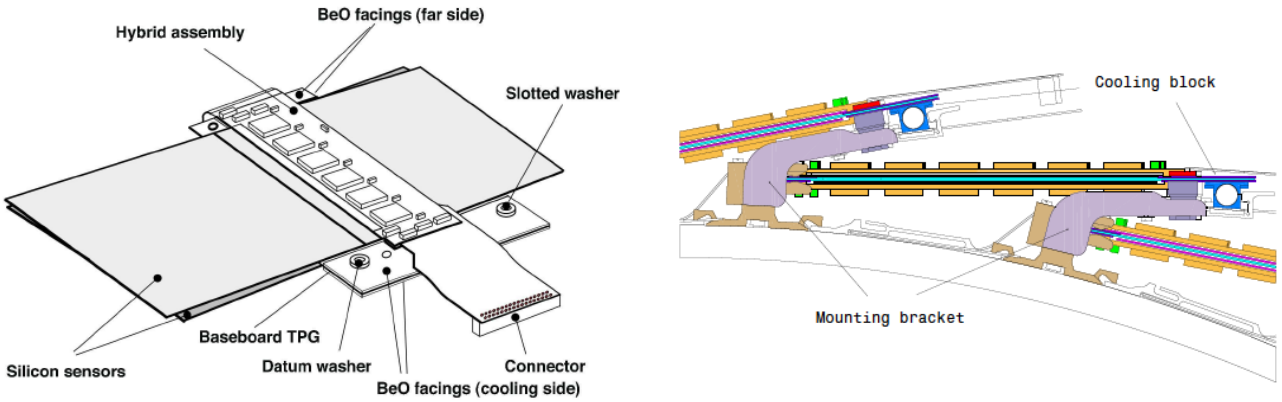

Figure 3.6: Structure of the SCT barrel module and the arrangement on the SCT barrel support structure [53].

3.3.4 Transition Radiation Tracker (TRT)

The Transition Radiation Tracker (TRT) is a gaseous detector consisting of 370,000 cylindrical straw tubes. It improves the momentum resolution of the ID system and provides electron/hadron separation by the transition radiation signature, since the transition radiation depends on the Lorentz factor of the particle. A 4 mm diameter tube made of 60 μm thick multi-layer film of carbon-polyimide-aluminium-Kapton-polyurethane functions as cathode while a 30 μm diameter gold-plated tungsten-rhenium wire works as anode. The straws are filled with

a gas mixture based on Xenon (70%) for good X-ray absorption with addition of CO_2 (27%) and O_2 (3%) to increase the electron drift velocity and for photon-quenching. The wire potential is kept at ground and a voltage of -1.5 kV is applied to the tube. The amplification factor is about 2.4×10^4 and the maximum drift time is 45 ns. The TRT also has two parts, the barrel consisting of 73 layers of straws and the two end-caps each consisting of 160 straw layers. 15 μm diameter polypropylene/polyethylene(PP/PE) fibre sheets are used as the transition radiation material in barrel and 17 μm thick PP/PE foils are used in the end-cap regions. The TRT is designed to have 36 hits (22 hits in the transition region: $0.8 < |\eta| < 1.0$) for a charged particle with $p_T > 0.5$ GeV up to $|\eta| < 2.0$. A front end electronics consists of Amplifier Shaper Discriminator Baseline Restorer (ASDBLR) and Digital Time Measurement Readout Chip (DTMROC). The front end system has two thresholds: low threshold is about 300 eV for minimum ionising particle and high threshold is about 6-7 keV for electron. The pion rejection factor is 20 with a 90% electron efficiency.

3.4 Calorimeter

The calorimeter is one of the commonly used detectors in high-energy physics experiments for the following distinguishable points.

- Energy resolution of calorimeter improves with increasing the energy of the particle, $\sigma_E/E \sim 1/\sqrt{E}$.
- The calorimeter can measure the energy of neutral particle (photon and neutral hadrons).
- The calorimeter response is fast enough and the energy deposit from the particle is easily calculated (less CPU load).
- The shower depth increases only logarithmically with the energy, $L \sim \ln(E/E_c)$, where E_c is the critical energy.

The calorimeters can be classified as a homogeneous calorimeter and a sampling calorimeter. The homogeneous calorimeter is made high density of uniform material, with whole detector volume functioning not only as absorber but also as active material. Generally, homogeneous calorimeter provides better energy resolution but it is expensive. The sampling calorimeter consists of alternating layers of absorber and active material. It is more flexible for the material choice, thus it is cost effective. The ATLAS calorimeter system is based on sampling calorimeter design. See, Figure 3.7. The electromagnetic (EM) calorimeter is used to measure the energy of electrons and photons via electromagnetic interactions (bremsstrahlung, electron-positron pair production). The hadronic calorimeter is used to measure the energy of hadrons via electromagnetic and strong interactions. This section describes the detail of the ATLAS calorimeter system.

3.4.1 Electromagnetic calorimeter

The electromagnetic (EM) calorimeter measures the energy of electron and photon via electromagnetic process. The radiation length X_0 is a parameter to describe the characteristic length of the EM calorimeter. The radiation length is approximately written as [3]

$$X_0(\mathrm{g/cm^2}) \simeq \frac{716\ \mathrm{gcm^{-2}A}}{\mathrm{Z(Z+1)\ ln(287/\sqrt{(Z)})}}, \tag{3.6}$$

where Z and A are the atomic number and mass number of the material. For high energy electrons (E>1 GeV), bremsstrahlung is the dominant process when the electron deposit the energy on the calorimeter. The radiation length is a mean length that an electron loses the energy to 1/e of its energy, $\langle E(x)\rangle = E_0 e^{-\frac{x}{X_0}}$. For high energy photons (E>1 GeV), the energy is absorbed mainly via electron-positron pair creation. The radiation length is also 7/9 of the mean free path for pair creation. The incident electron produces a photon via bremsstrahlung and produced photon produces electron-positron pair again via pair creation. These processes continue until the energy of produced particles are lower than the critical energy E_c, below which the particle predominantly looses the energy by ionisation instead of particle creation. E_c is approximately given by $E_c \simeq 610(710)/(Z+1.24(0.92))$ MeV (there are other definitions). The processes are observed as an EM shower

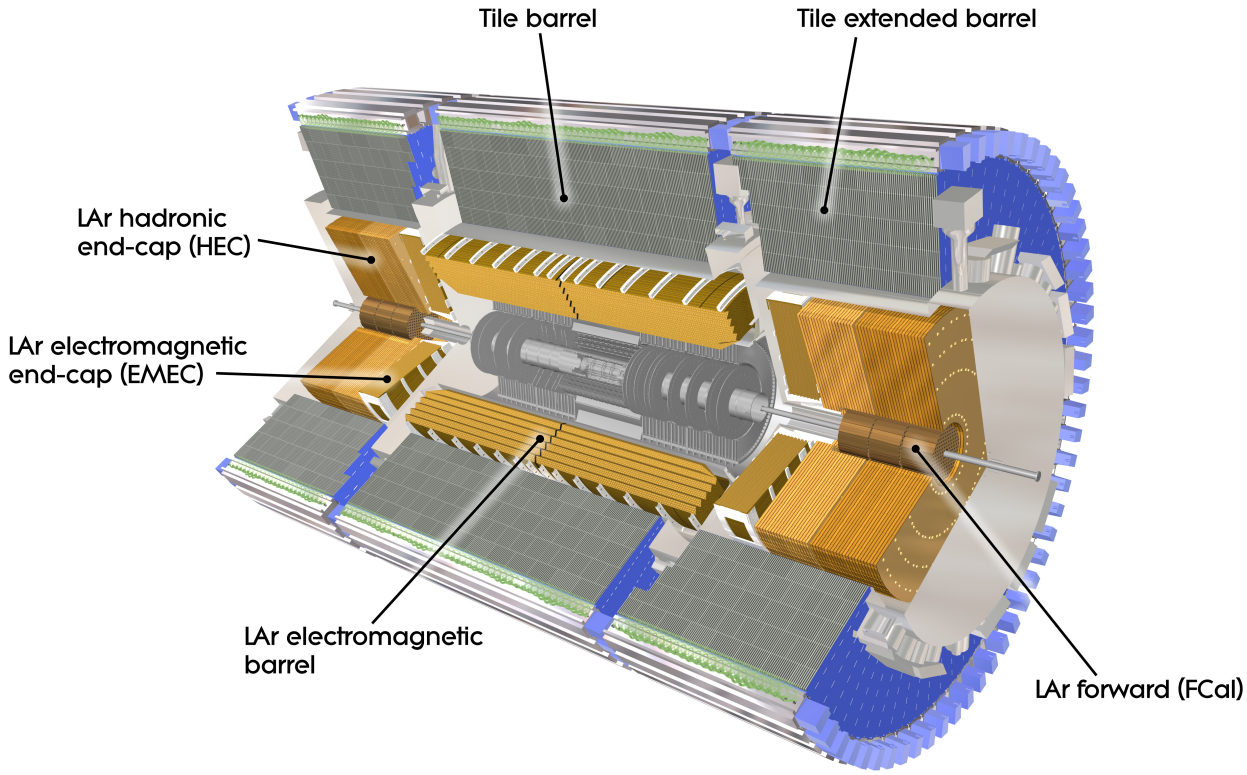

Figure 3.7: Illustration of the ATLAS Calorimeter [58].

in the calorimeter with the shower shape scaled in terms of in the radiation length. The shower distance is measured in unit of radiation length and the energy in unit of critical energy, both scales being dependent on the material of the absorber. The calorimeter thickness containing 95% of the shower energy is approximately given in terms of the scale variables $t = x/X_0$ and $y = E_0/E_c$ by [3]

$$t_{95\%} \simeq \ln y + t_0 + 0.08Z + 9.6. \tag{3.7}$$

where t_0=-0.5 (+0.5) for electrons (photons). and the transverse shower size is given by the Moliere radius (R_M) [3]

$$R_M(\mathrm{g/cm^2}) \simeq 21(\mathrm{MeV})\frac{\mathrm{X_0}}{\mathrm{E_c(MeV)}} \tag{3.8}$$

A cylinder with radius R_M contains 90% of the shower energy. The energy measurement in the EM calorimeters is equal to measure the number of electrons and positrons produced in an EM shower, which is proportional to the energy of incident electron/photon. The showering process is a stochastic process. The calorimeter energy resolution is ideally described by the stochastic uncertainty, $\sigma(E)/E \propto 1/\sqrt{E}$. For the sampling calorimeter, there is an additional contribution for stochastic term due to the sampling fluctuation. Since the number of electron and positrons reaching active layer is approximated $N_{ch} = E/(E_c t_{abs})$, where t_{abs} is a thickness of absorber in radiation length, the intrinsic resolution of sampling calorimeter is given by $\sigma(E)/E \propto \sqrt{E_c t_{abs}/E}$. In the real case, there are additional uncertainties and the actual energy resolution is written as

$$\frac{\sigma_E}{E} = \frac{a}{\sqrt{E}} \oplus b \oplus \frac{c}{E}, \tag{3.9}$$

where the symbol $\oplus$ indicates a quadratic sum. Each term is known as stochastic term, constant term and noise term.

The stochastic term includes photo-electron statistics of photo device if used. The constant term includes contributions due to response non-uniformities, calibration uncertainty, the effect of dead material and energy loss before the calorimeter. Especially, in radiation environment, radiation damage of active material may become considerable. The noise term is a contribution from readout electronics. The ATLAS EM calorimeter is a sampling calorimeter with lead absorber and liquid argon (LAr) as an active material. The LAr provides good energy resolution since the uniformity of the detector is well controlled. The disadvantages of the LAr is relatively slow signal due to slow charge collection. The LAr gap has a constant distance of 2.1 mm in the barrel and a high voltage of $\simeq$2 kV is applied across this gap, where the maximum electron drift time is $\simeq$450 ns. The calorimeter signal is sampled at every 25 ns in coincidence with the beam crossing. The signal is extracted out radially to reduce the wiring delay and to make the longitudinal segmentation easier. To minimise the inactive area, an accordion design is employed to cover the full ϕ region. In the η direction, the EM calorimeter cover $|\eta|$ <3.2. A presampler is a thin independent LAr layer to measure the energy loss before reaching the EM calorimeter. The EM barrel calorimeter (EMB) covers $|\eta|$ <1.475 and EM end-cap calorimeter (EMEC) covers 1.375< $|\eta|$ <3.2. The EMB consists of two identical half-barrels with small gap (6 mm) at z=0. The EMEC consists of two co-axial wheels on each side, divided at $|\eta|$ = 2.5. The absorbers are made of lead plates cladded with stainless steel of 0.2 mm thickness. The lead thickness is 1.53 (1.13) mm for $|\eta| < 0.8$ ($|\eta| > 0.8$) in barrel and is 1.7 (2.2) mm for $|\eta| < 2.5$ ($|\eta| > 2.5$) in end-caps. The gap thickness is 2.1 mm for barrel and 2.8-0.9 (3.1-1.8) mm for $|\eta| < 2.5$ ($|\eta| > 2.5$) in end-caps. The readout electrode consists of three copper layers insulated by kapton sheets and is located in the gap between the absorber plates. High-voltage is applied to the outer two copper layers while the signal is read out through centre copper layer which is capacitively coupled to the ground. The first segment of the calorimeter is read out from the front, the second and third segments are read out from the back. The LAr are cooled at $\sim$89 K. The variation of LAr temperature has influence on the signal height by -2%/K, adding an extra constant term of energy resolution. The temperature is measured using 500 of PT100 platinum resistors every minute to suppress the energy resolution degradation to a negligible (<0.2%) level. Also impurity of LAr has a contribution to the constant term. The purity of LAr is measured using 30 purity monitors in each cryostat every 15 minutes. The impurities are controlled to 200$\pm$100 ppb O_2 equivalent, impact on the energy resolution being negligible. A summary of the calorimeter read-out segmentation in η-ϕ plane and in depth is shown in Table 3.5. The typical energy resolution of electromagnetic barrel calorimeter is $\sigma_E/E = 9.4\%/\sqrt{E} \oplus 0.1\%$ [59].

Table 3.4: Summary of the segmentation in (η, ϕ) of the EM calorimeters. [53]

Detector and Segment	$\lvert\eta\rvert$ coverage	Segmentation in (η, ϕ)	Radiation Lengths
Pre-sampler Barrel	$\lvert\eta\rvert < 1.52$	(0.025, 0.1)	-
EM Barrel	$\lvert\eta\rvert < 1.475$		$22-$
1_{st} segment	$\lvert\eta\rvert < 1.4$	(0.025/8, 0.025)	≈ 4
	$1.4 < \lvert\eta\rvert > 1.475$	(0.025, 0.025)	
2_{nd} Segment	$\lvert\eta\rvert < 1.4$	(0.025, 0.025)	≈ 17
	$1.4 < \lvert\eta\rvert < 1.475$	(0.075, 0.025)	
3_{rd} Segment	$\lvert\eta\rvert < 1.35$	(0.05, 0.025)	$\approx 1-10$
Pre-sampler End-cap	$1.5 < \lvert\eta\rvert < 1.8$	(0.025, 0.1)	-
EM End-cap	$1.375 < \lvert\eta\rvert < 3.2$		
1_{st} Segment	$1.375 < \lvert\eta\rvert < 1.425$	(0.050, 0.1)	≈ 4
	$1.425 < \lvert\eta\rvert < 1.5$	(0.025, 0.1)	
	$1.5 < \lvert\eta\rvert < 1.8$	(0.025/8, 0.1)	
	$1.8 < \lvert\eta\rvert < 2.0$	(0.025/6, 0.1)	
	$2.0 < \lvert\eta\rvert < 2.4$	(0.025/4, 0.1)	
	$2.4 < \lvert\eta\rvert < 2.5$	(0.025, 0.1)	
	$2.5 < \lvert\eta\rvert < 3.2$	(0.1, 0.1)	≈ 25
2_{nd} Segment	$1.375 < \lvert\eta\rvert < 1.425$	(0.050, 0.025)	≈ 17
2_{nd} Segment	$1.425 < \lvert\eta\rvert > 2.5$	(0.025, 0.1)	
2_{nd} Segment	$2.5 < \lvert\eta\rvert > 3.2$	(0.1, 0.1)	$\approx 3-11$
3_{rd} Segment	$1.5 < \lvert\eta\rvert < 2.5$	(0.050, 0.025)	$\approx 5-15$

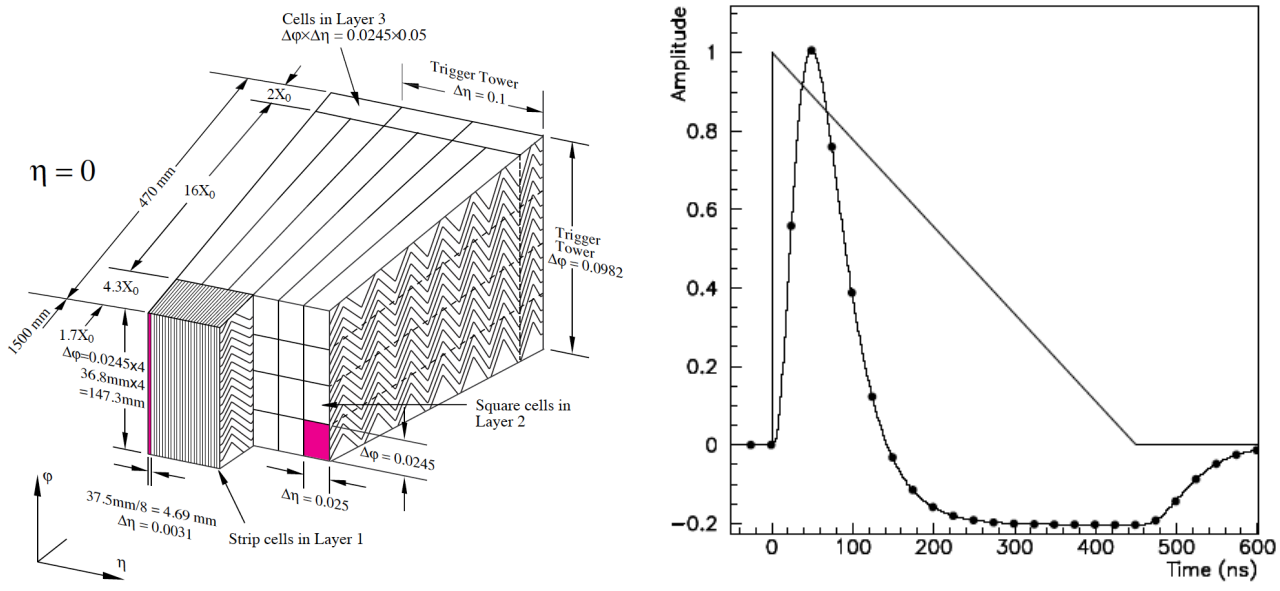

Figure 3.8: LAr accordion EM calorimeter(left) has three segmentations in depth. LAr calorimeter raw signal, and sampling of the signal after over compensated shaper amplifier. [53]

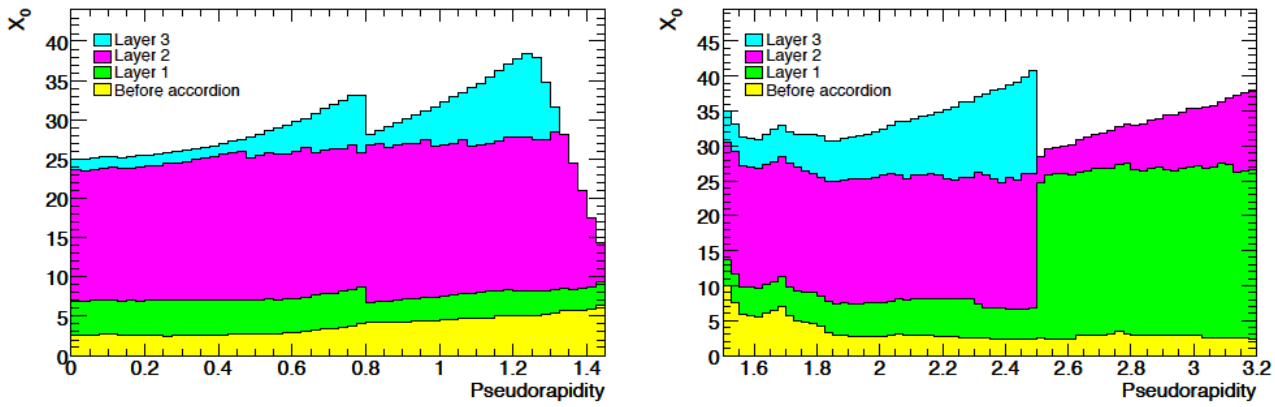

Figure 3.9: The radiation length of the ATLAS EM calorimeter in the barrel(left) and end-cap(right) regions, which is $> 25\ X_0$ except in barrel-to-endcap transition region. [53]

3.4.2 Hadron calorimeter

The hadronic interaction in the hadron calorimeter may be described in the analogy of the electromagnetic interaction in the EM calorimeter. But the interaction is more complex due to the nature of strong interaction. The hadronic interaction length characterises the hadron shower similar to the radiation length in EM shower. It is approximated as $\lambda \sim 35(\mathrm{g/cm^2})A^{1/3}$. The interaction length is about one order longer compared to the radiation length ($\lambda/X_0 \sim 10$ in case of Fe). The longitudinal shower size is approximately described by

$$L_{95\%} = 0.2\ln(E) + 0.7 + 2.5(E)^{0.3}\ \text{(E in GeV)}. \tag{3.10}$$

Typically 6-9λ is required to contain high energy hadron shower with the transverse shower size $R_{95\%} = \lambda$. So the hadron shower size is longer and wider than EM shower. The sampling calorimeter is an appropriate design feasible for the hadron calorimeter. The energy resolution of hadron calorimeter is expressed in the same equation as EM calorimeter resolution ($\sigma_E/E = a/\sqrt{E} \oplus b \oplus c/E$). The values are worse than of EM calorimeter, since there are two components in the hadron shower, EM contribution and hadron contribution and some fraction of energy are transformed into invisible components, such as muons, nuclear-binding energy. After the hadronisation, 25%, 65% and 10% of the energy is converted into photons, charged hadrons and neutral hadrons, respectively. Roughly, 30% of the charged hadron energy is depositted into electromagnetic calorimeter, hence half the energy is measured at electromagnetic calorimeter and remaining half the energy is measured at hadronic calorimeter. The effect of the former is explained as the energy response of the calorimeter is different for EM energy deposition and hadron energy deposition (e/h ratio $\neq$ 1) and the fraction of EM and hadronic components is dependent on the energy of the incident particle, which also fluctuates statistically. Various effects can be partially compensated by taking the effects by calibration, but the fluctuations are inherent.

Tile hadron calorimeter

The tile calorimeter system is divided into three subdetectors. The central barrel with a length of 6.54 m and two extended barrels with a length of 2.28 m each installed both sides of the central barrel provide an energy measurement up to $|\eta| < 1.7$. The inner radius is 2.28 m and outer radius is 4.25 m. The interaction length of approximately 7.4λ at $|\eta| = 0$. They consist of steel absorbers and plastic scintillator plates with a volume ratio of approximately 4.7:1. The scintillation photons are collected and extracted using wavelength-shifting fibres (WLSFs) and detected by photomultiplier tubes (PMTs, Hamamatsu R7877). The e/h ratio of the tile calorimeter is approximately 1.4. The read-out cells have an almost projective geometry with the boundaries being approximately constant in η and ϕ providing a granularity of 0.1×0.1 in $\eta \times \phi$ (The last segment has an η granularity of 0.2). Figure 3.13 shows the thickness of each of the longitudinal segments in units of interaction length. The gaps between the barrel and extended barrel are filled with steel/scintillator

special module. The PMTs and front-end boards are integrated in 1.4 m long aluminium units called drawers. The barrel comprises of 64 modules divided in ϕ direction. Each module has 11 rows filled with basic unit which is a laminate structure of 5±0.05 mm thick full length steel sheets (master plate) and 4.05±0.04 mm thick short steel sheets (spacer plates) glued in a staggered arrangement along the radial direction to form the pockets. Polystyrene scintillator tiles, 3 mm thick and with radial length ranging from 97 mm to 187 mm and azimuthal length ranging from 200 mm to 400 mm, are inserted into the pockets. The scintillator emits the ultraviolet scintillation light, and converts it to visible light (peak at 476 nm) in pTP (1.5%) and POPOP (0.044%) doped polystyrene. The visible light is collected by 1 mm diameter WLSF attached to the plate side. One PMT detects the light from the WLSFs in one cell which is defined as follows. The radial direction is divided into 3 segments with interaction lengths 1.5, 4.1 and 1.8 λ at $|\eta| = 0$. The granularity is $\Delta\eta \times \Delta\phi = 0.1 \times 0.1$ (0.2×0.1 for outermost segments). The light collected at each edge is read out by one PMT; two PMTs per segment for redundancy and signal uniformity. The tile calorimeter energy resolution for

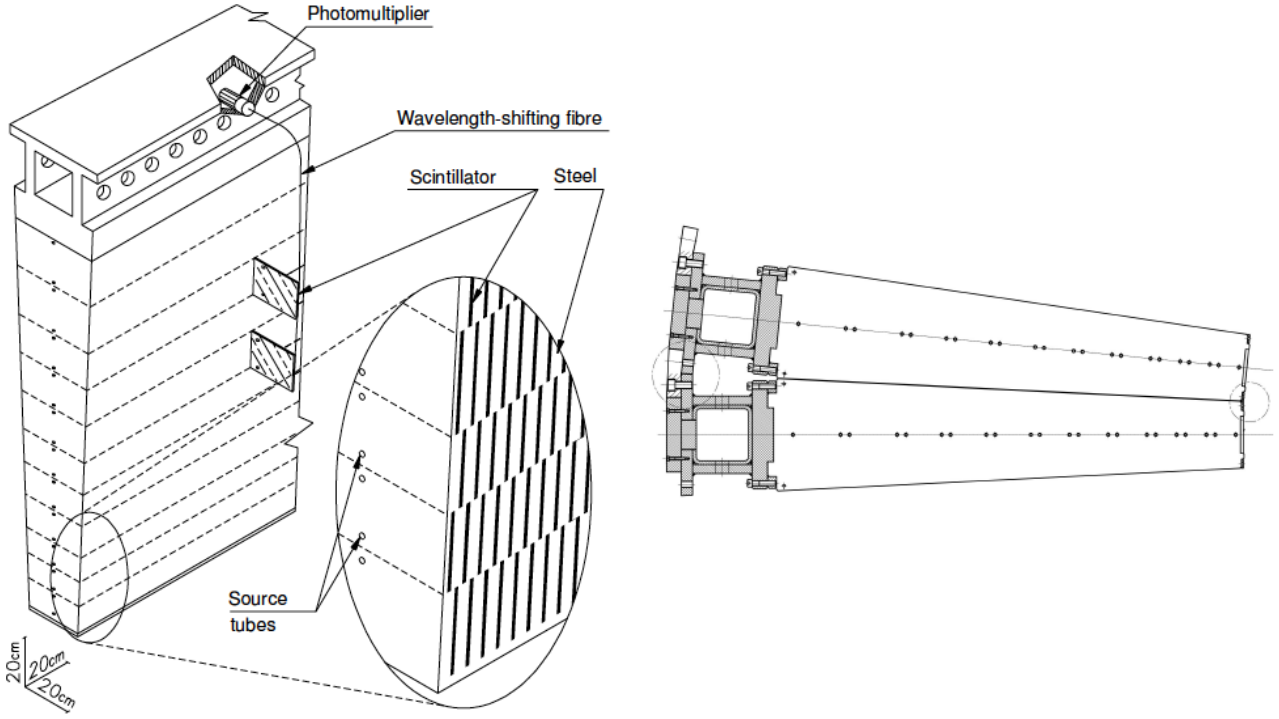

Figure 3.10: Schematic view of the ATLAS tile calorimeter module (left). The modules are stacked to build a barrel structure (right) [53].

single pion is $\sigma_E/E = 52.9\%/\sqrt{E} \oplus 5.7\%$.

Hadronic end-cap calorimeter (HEC)

The hadronic end-cap calorimeter (HEC) is a sampling calorimeter with liquid argon as active material and copper as absorber technically similar to the EM calorimeter. Since LAr calorimeter is radiation hard, it covers the η range of $1.5 < |\eta| < 3.2$. The HEC shares the cryostat with other end-cap LAr calorimeters (electromagnetic calorimeter and forward calorimeter). Each side of end-cap has a front wheel (HEC1) and a rear wheel (HEC2) constructed with 32 modules. The thicknesses of the copper plate are 25 mm and 55 mm for HEC1 and HEC2, respectively. The gap between the absorbers 8.5 mm is divided into four drift zones of 1.85 mm width each separated by three electrodes. The sampling fractions of HEC1 and HEC2 are 4.4% and 2.2%. The middle electrode functions as the read-out electrode and defines the $\eta \times \phi$ segmentation, while the other two function as high voltage electrode. These planes form an electrostatic transformer (EST). Their granularity is $\Delta\eta \times \Delta\phi = 0.1 \times 0.1$ in the HEC1 and 0.2×0.2 in the HEC2. Typical drift time is 430 ns with the high voltage at 1800 V. The HEC uses cyrogenic GaAs preamplifiers working at LAr temperature (89 K) to optimise the signal to noise ratio.

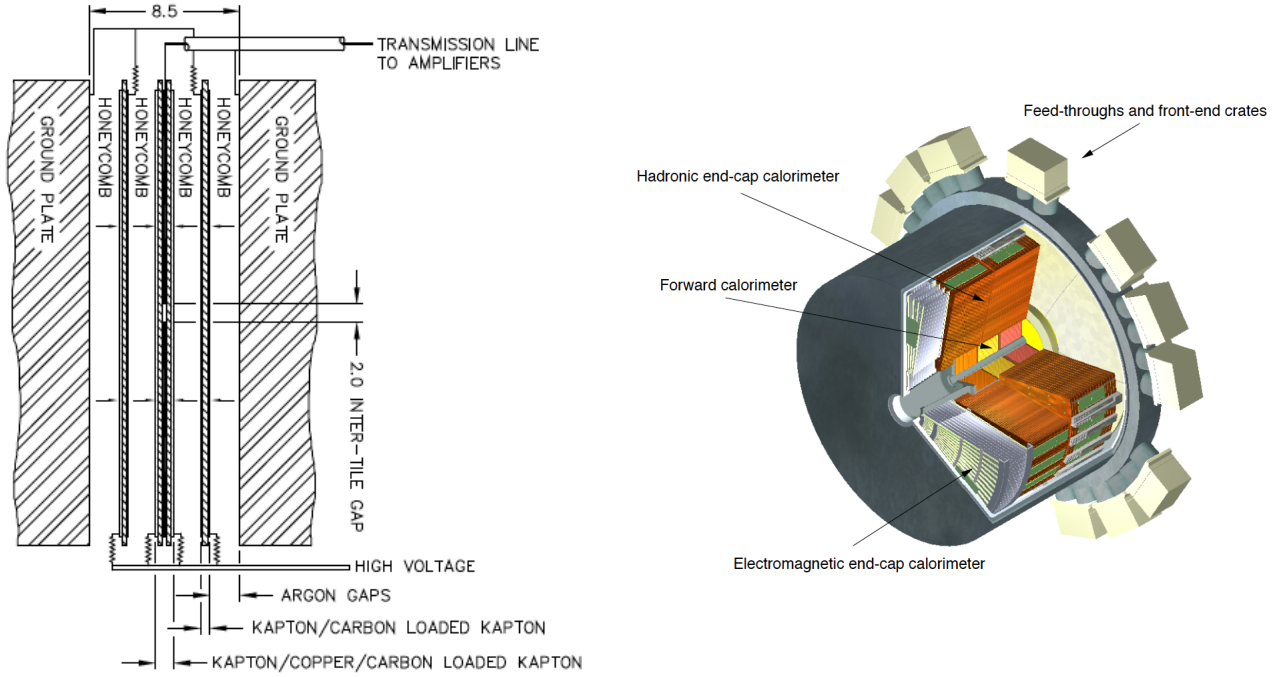

Figure 3.11: The HEC read out structure (left) and the end-cap cryostat(right). The end-cap HEC shares the cryostat with other end-cap calorimeters. [53]

Forward calorimeter (FCal)

The forward calorimeter (FCal) also shares the cryostat with other LAr calorimeters. They are located at $|z|$=4.7 m and cover the η range of 3.1< $|\eta|$ <4.9. The FCal is divided into three 45 cm thick modules. The innermost is an electromagnetic module (FCal1) and outer two are hadronic modules (FCal2 and FCal3). Copper absorber was chosen for FCal1 to optimize the resolution and heat removal. Tungsten absorber is used in FCal1 and FCal2 to reduce the hadronic shower size. A copper alloy shielding plug has been mounted behind the FCal to reduce backgrounds in the end-cap muon system. The basic structure consists of plates having holes where electrode are rods inserted. The gaps are filled with LAr (Figure 3.12). The high voltage is distributed via high resistive charbon-loaded kapton layers. This design was chosen to fit to the small LAr gaps (0.269-0.508 mm) and to work under high radiation environment. A summary of the calorimter read-out segmentaions in η-ϕ

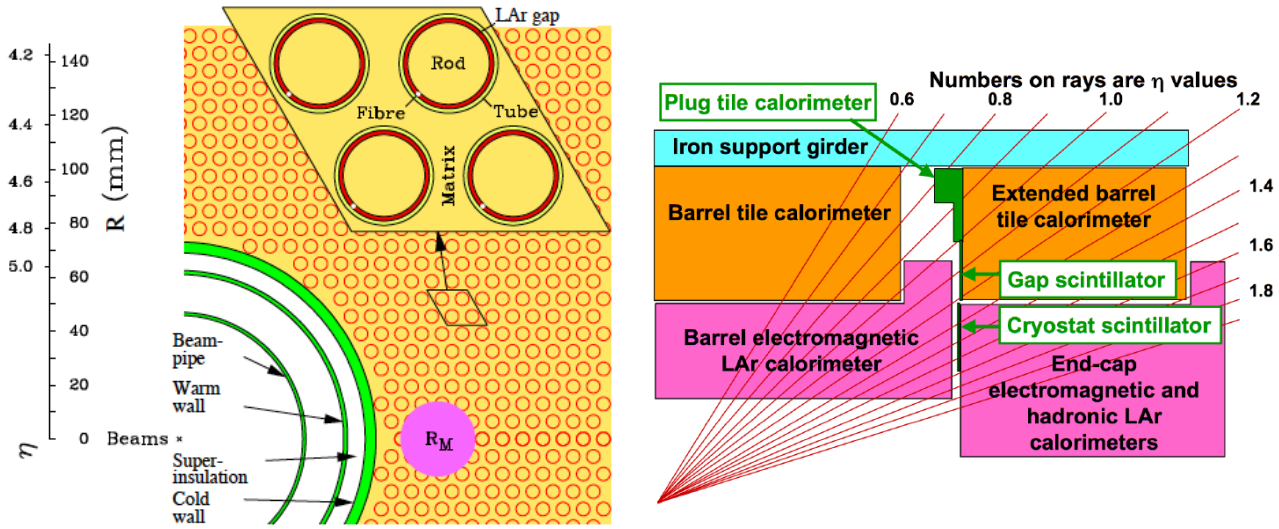

Figure 3.12: Design of the forward calorimeter module and arrangement of various calorimeter system. [53]

plane and in depth is shown in Table 3.5.

Table 3.5: Summary of the segmentation in (η, ϕ) of the hadron calorimters in the barrel and in the end-cap (EM FCal1 included) [53].

Detector and Layer	$\lvert\eta\rvert$ coverage	Segmentation in (η, ϕ)
Tile Barrel	$\lvert\eta\rvert < 1.0$	
1_{st} and 2_{nd} Layer	$\lvert\eta\rvert < 1.0$	(0.1,0.1)
3_{rd} Layer	$\lvert\eta\rvert < 1.0$	(0.2,0.1)
Tile Ext-Barrel	$0.8 < \lvert\eta\rvert < 1.7$	
$1_{st} and 2_{nd}$ Layer	$0.8 < \lvert\eta\rvert < 1.7$	(0.1,0.1)
3_{rd} Layer	$0.8 < \lvert\eta\rvert < 1.7$	(0.2,0.1)
LAr End-cap	$1.5 < \lvert\eta\rvert < 3.2$	
Inner wheel	$1.5 < \lvert\eta\rvert < 2.2$	(0.1,0.1)
Outer wheel	$2.5 < \lvert\eta\rvert < 3.2$	(0.2,0.2)
LAr Forward	$3.1 < \lvert\eta\rvert < 4.9$	Granularity $\Delta x \times \Delta y$ (cm)
FCal1	$3.15 < \lvert\eta\rvert < 4.3$	3.2×2.6
	$3.10 < \lvert\eta\rvert < 3.15$	four times finer
	$4.30 < \lvert\eta\rvert < 4.83$	four times finer
FCal2	$3.24 < \lvert\eta\rvert < 4.50$	3.3×4.2
	$3.20 < \lvert\eta\rvert < 3.24$	four times finer
	$4.50 < \lvert\eta\rvert < 4.81$	four times finer
FCal3	$3.32 < \lvert\eta\rvert < 4.6$	5.4×4.7
	$3.29 < \lvert\eta\rvert < 3.32$	four times finer
	$4.6 < \lvert\eta\rvert < 4.75$	four times finer

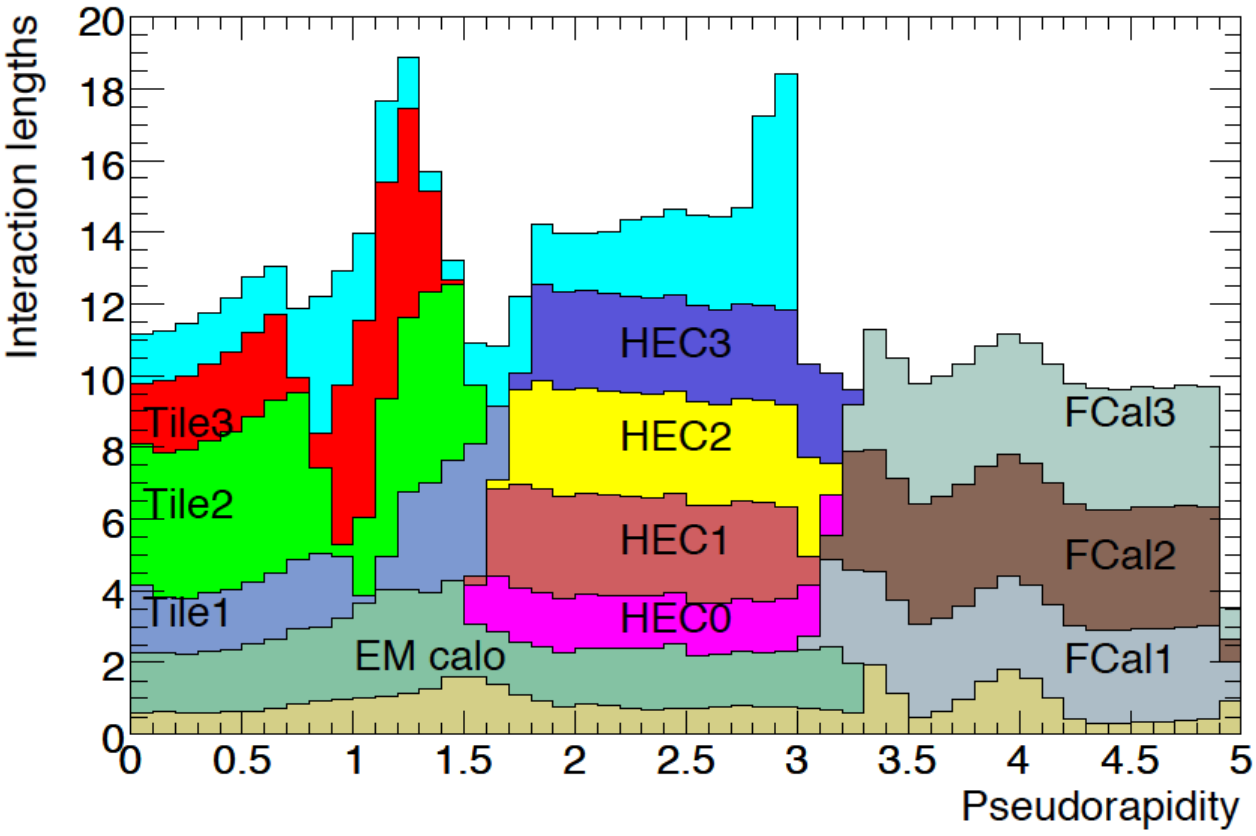

Figure 3.13: The interaction length of calorimeter system as function of pseudorapidity. $> 10\ \lambda$ is achieved up to $\lvert\eta\rvert < 4.9$. [53]

3.5 Muon spectrometer

Muon spectrometer is a detector for muon identification and momentum measurement. This system consists of distinctive toroid magnets, muon detectors with precision position measurement and muon detectors with fast response for trigger. The precision muon detectors cover the region $|\eta| < 2.7$ and the fast muon detectors cover the region $|\eta| < 2.4$. Gaseous detectors are used to cover the huge area outside of the calorimeter. Precision tracking system measures the muon trajectory within $\mathcal{O}(\mu s)$. On the other hand, trigger chambers provide very fast response $\mathcal{O}$(ns) in order to construct a trigger signal.

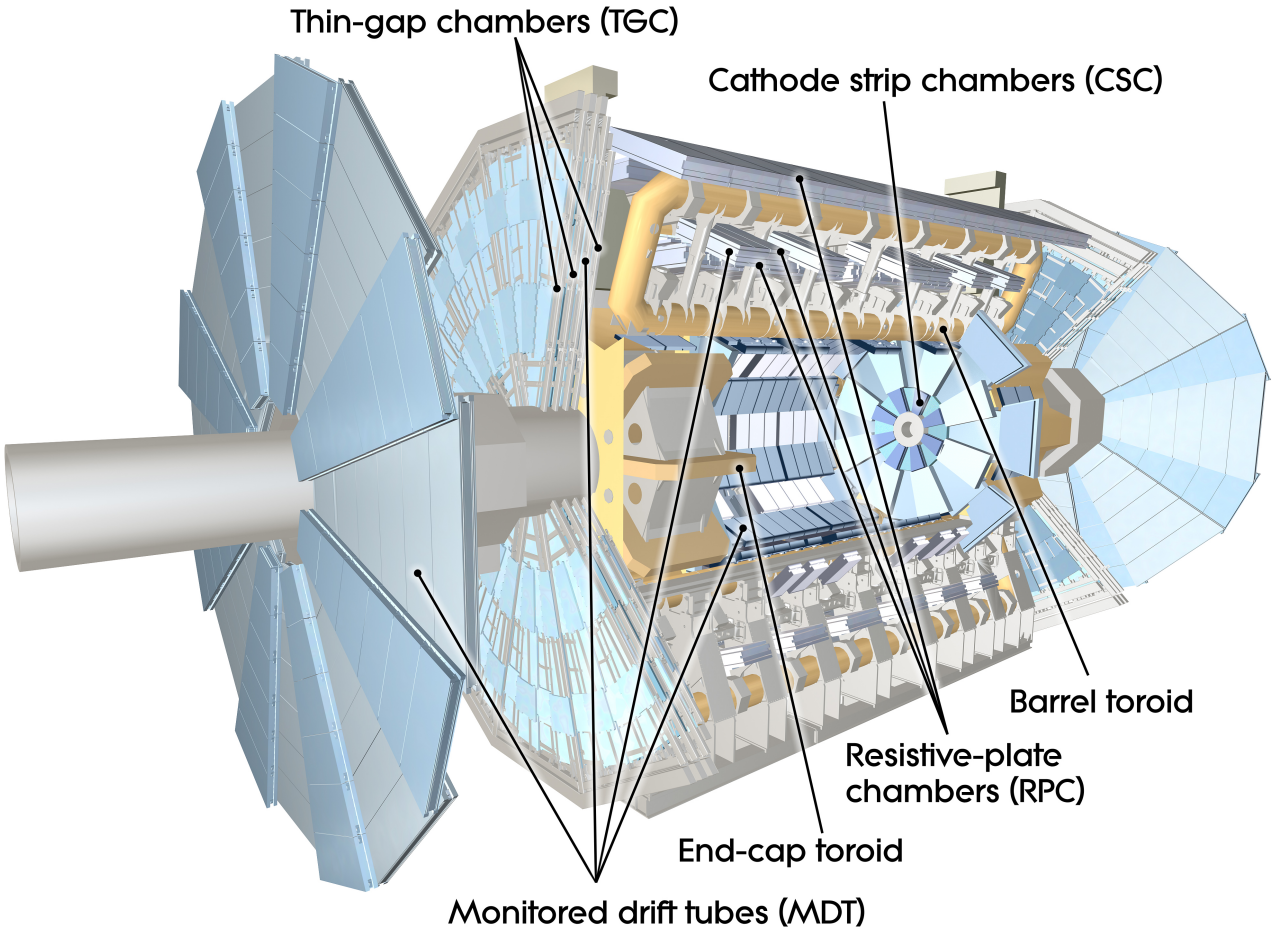

Figure 3.14: Illustration of the ATLAS Muon spectrometer [60].

3.5.1 Toroidal magnet system

Very large air-core toroidal magnets provide 1.5 to 5.5 Tm of bending power in the barrel region ($|\eta| < 1.6$) and $1-7.5$ Tm in the end-cap region ($1.6 < |\eta| < 2.7$). The bending power can be negative around the transition region ($1.4 < |\eta| < 1.6$) (See Figure 3.5.1). Air-core toroid design suppresses the multiple scattering and provides a magnetic field in the forward region. The coil is made of Rutherford NbTi/Cu superconducting strands stabilised by high purity Al. The barrel toroid system has eight coils housed in independent cryostat, each coil having axial length of 25.3 m located at radii $9.4-20.1$ m. Each of the end-cap toroid systems also has eight coils, axial length 5 m and in radii $1.65-10.7$ m. They are rotated by 22.5° with respect to the barrel toroid coil system in order to provides radial overlap and to optimise the bending power at the interface between the two coil systems. The coil is cooled at 4.5 K and provide the peak magnetic field of ≈ 4 T at current of 20.5 kA. The magnetic field is complex, distributed inhomogeneously. The magnetic field was precisely ($< 0.5\%$) mapped.

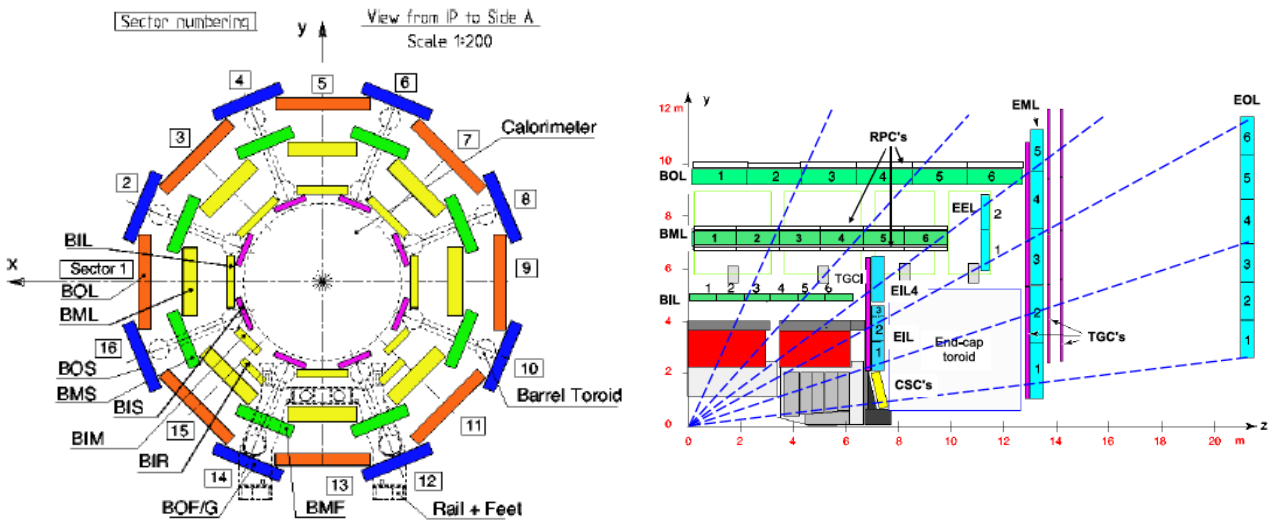

Figure 3.15: Illustration of the ATLAS muon spectrometer [53]. The transverse plane (left) and the longitudinal plane (right). Barrel muon spectrometer divided into 16 sectors.

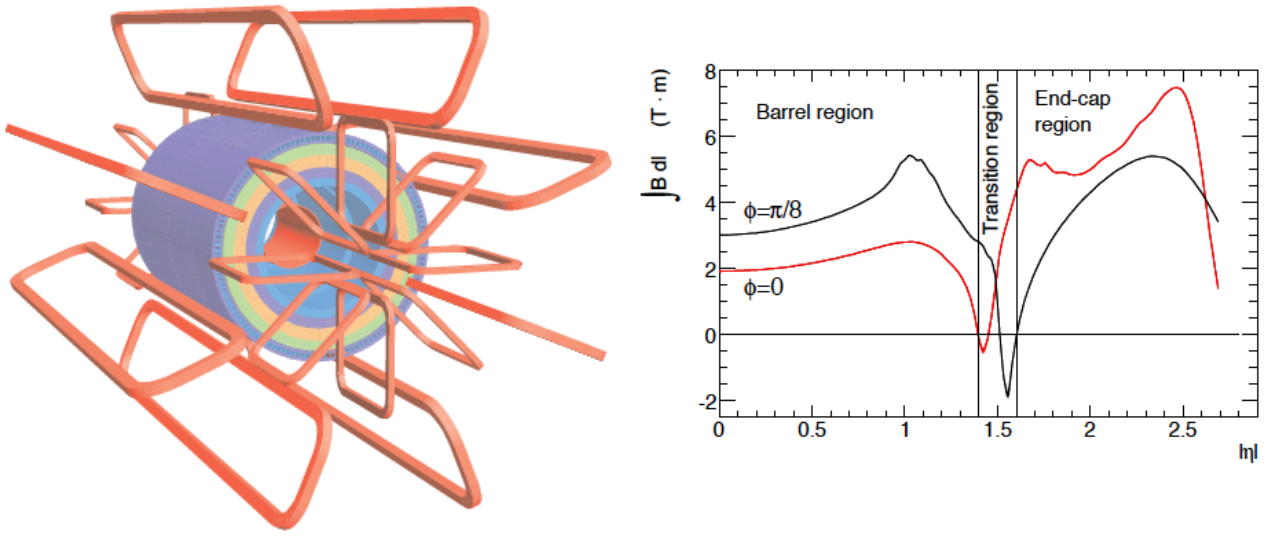

Figure 3.16: Schematic view of ATLAS toroid magnet coil (left) and the bending power as a function of $|\eta|$. The curves correspond to the azimuthal angles $\phi = 0$ (red) and $\phi = \pi/8$ (black) [53].

3.5.2 Muon precision chambers

The performance goal of muon spectrometer is a transverse momentum resolution of approximately 10% for 1 TeV muons. Since the corresponding sagitta is approximately 500 μm, the resolution of muon precision chamber must be better than 50 μm. Monitored Drift Tube (MDT) and a Cathode Strip Chamber (CSC) detectors provides precision measurement of the muon track. The MDT covers $|\eta| < 2.7$, where as innermost region within $2 < |\eta| < 2.7$ is covered by CSC to cope with the high rate (150 Hz/cm^2).

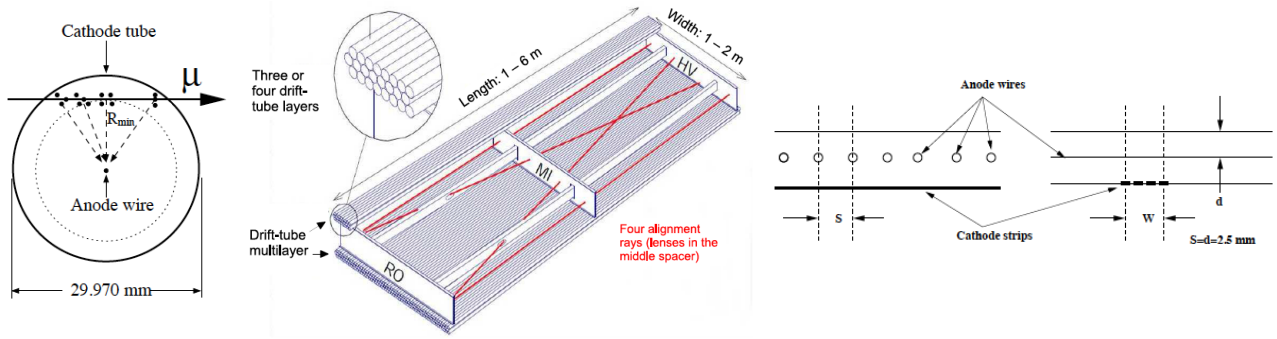

Figure 3.17: MDT consists of drift tubes (left) and the alighment is laser monitored (middle). CSC is a multi-wire proportional chamber (right). [53]

Monitored Drift Tube (MDT)

The MDT is a drift tube detector which fills a total area of 5500 m^2. The drift tube is aluminium tube with a wall thickness of 0.4 mm and diameter of 29.970 mm where 50 μm diameter W-Re(97/3) wire is strang. The tube is filled with a mixture of Ar/CO_2(93/7) at 3 bar. The gain is 2×10^4 at high voltage of 3.080 V. Each module consists of double layer of 3 or 4 monolayers. The resolution with single tube measurement is 80 μm and with one chamber is 35 μm. The barrel part has 3 modules of stations, each module installed radius of 5 m, 7.5 m and 10 m. For a track crossing three MDT chambers, a sagitta resolution of δS = 45 μm is thus expected. In the end-cap parts, modules are located at $|z| \approx 7.4$ m, 10.8 m, 14 m and 21.5 m. There are gaps of $|\eta| < 0.08$ in the large and of $|\eta| < 0.04$ in the small sectors, and around $\phi = 6\pi/4$ and $\phi = 7\pi/4$ due to the detector support structure. The maximum drift time is about 700 ns.

Cathode Strip Chamber (CSC)

The Cathode Strip Chamber is located at $|z| \sim 7$ m and at radius of around $1 < r < 2$ m. The CSCs are multiwire proportional chambers (MWPCs). The anode wire pitch is 2.54 mm and the cathode read out strip width is 1.519/1.602 mm with 5.308/5.567 mm pitch in the large/small chambers. The anode-cathode spacing is 2.54 mm, same as the anode wire pitch. The electron drift time is less than 40 ns with a time resolution of $\sim$7 ns. The gas is a mixture of Ar : $CO_2 = 80\% : 20\%$ and the gain is 6×10^4 at a high voltage of 1900 V. The spatial resolution of the CSC is 60 μm per CSC plane.

3.5.3 Muon trigger chambers

The muon trigger system employs two different types of detectors for the barrel and the end-cap. The requirements for the muon trigger chambers are to perform muon transverse momentum measurement with bunch-crossing identification. The system has to have a time resolution less than 25 ns. The muon information from the trigger chambers is used to produce level 1 trigger and used also in the higher level trigger system.

Resistive Plate Chamber (RPC)

The RPC is a gaseous detector only with two resistive plates as electrodes. It covers η range of $|\eta| < 1.05$. The resistive plate is made of phenolic-melaminic plastic laminate. Figure 3.5.3 shows the structure of the RPC

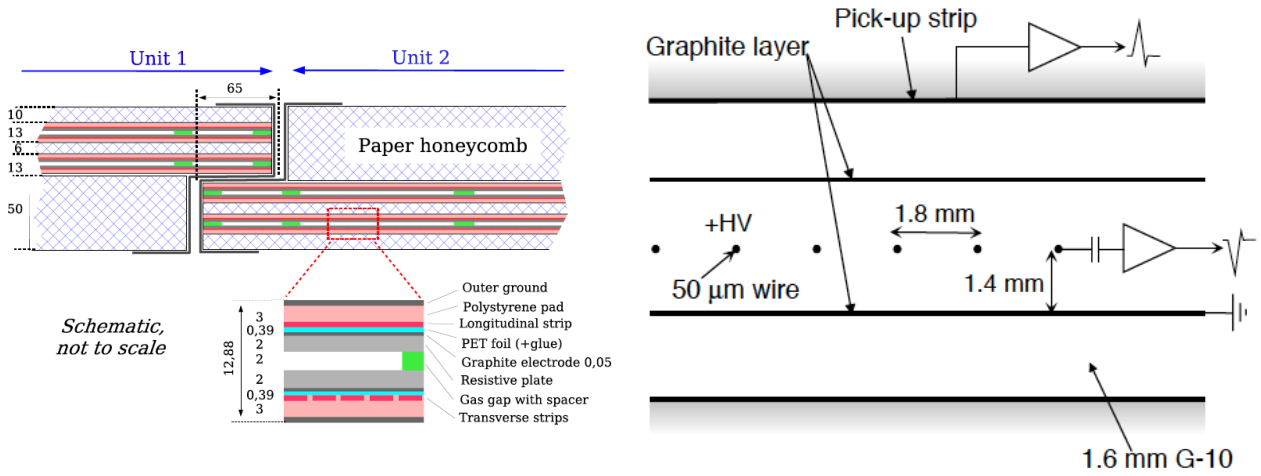

Figure 3.18: Schematic view of the RPC (left) module and TGC (right) module. Both detectors have very thin gaps filled with gases providing very fast signal to identify the bunch identification. [53]

module. The gap between the two plates is 2 mm and electric field of 4.9 kV/mm is applied. The signal is read out capacitively via metallic strips. The gas is a mixture of $C_2F_4H_2/i-C_4H_{10}/SF_6$ (94.7/5/0.3).

Thin Gap Chamber (TGC)

The thin Gap Chambers (TGCs) have two functions, one providing a trigger signal and another measuring the azimuthal angle to complement the measurement of the MDTs in the bending (radial) direction. It covers η range of $1.05 < |\eta| < 2.4$. The middle layer of the MDT in the end-cap is composed of seven layers of TGC, while the inner layer is composed of two layers. The TGC is a multi-wire proportional chamber (MWPC) which has a wire-cathode distance of 1.4 mm and wire-wire distance of 1.8 mm with a high quenching gas mixture of CO_2 and n-pentane (55% and 45%). The TGC is operated in a quasi-saturated mode with gas gain of $\approx 3 \times 10^5$. The TGC module consists of 1.6 mm thick FR4 (Frame Resistant 4) plates with graphite coated on the wire side and copper cladding on other side, and 50 μm Au coated W-Re wires. The position measurement on radial direction is provided by anode wires and is provided by cathode strips on ϕ direction. The wires are grouped in width of 10.8 mm to 55.8 mm and the radial strips are staggered to achieve an azimuthal granularity of 2-3 mrad.

3.6 Forward detectors for luminosity measurement

The luminosity measurement is achieved within 2-3% precision. The accuracy of luminosity calculated from the information provided by the LHC (e.g. number of protons, revolution frequency etc.) is 5-10% level. Luminosity measurements using Cherenkov Integrating Detector (LUCID) and Absolute Luminosity for ATLAS (ALFA) can achieve the required precision.

3.6.1 Luminosity measurement using Cherenkov integrating detector (LUCID)

The LUCID provides a relative luminosity by measureing the rate of inelastic p-p scattering in forward region. The absolute luminosity is obtained from QED ($\gamma\gamma \to \mu\mu$), $W \to l\nu$ and $Z \to ll$ processes calculations. The LUCID response calibrattion is cross-checked using the data obtained by the ALFA (see next section). The LUCID is located ≈17 m apart from the IP ($5.6 < |\eta| < 6$). It consists of 20 aluminium tubes filled with C_4F_8 at a pressure of 1.1-1.5 bar. The Cherenkov light emitted due to an incident charged particles is detected via PMT. The threshold for Cherenkov light by electrons is 10 MeV and that by πs is 2.8 GeV. The detector response is $\mathcal{O}$ ns to identify bunch crossing ID (BCID).

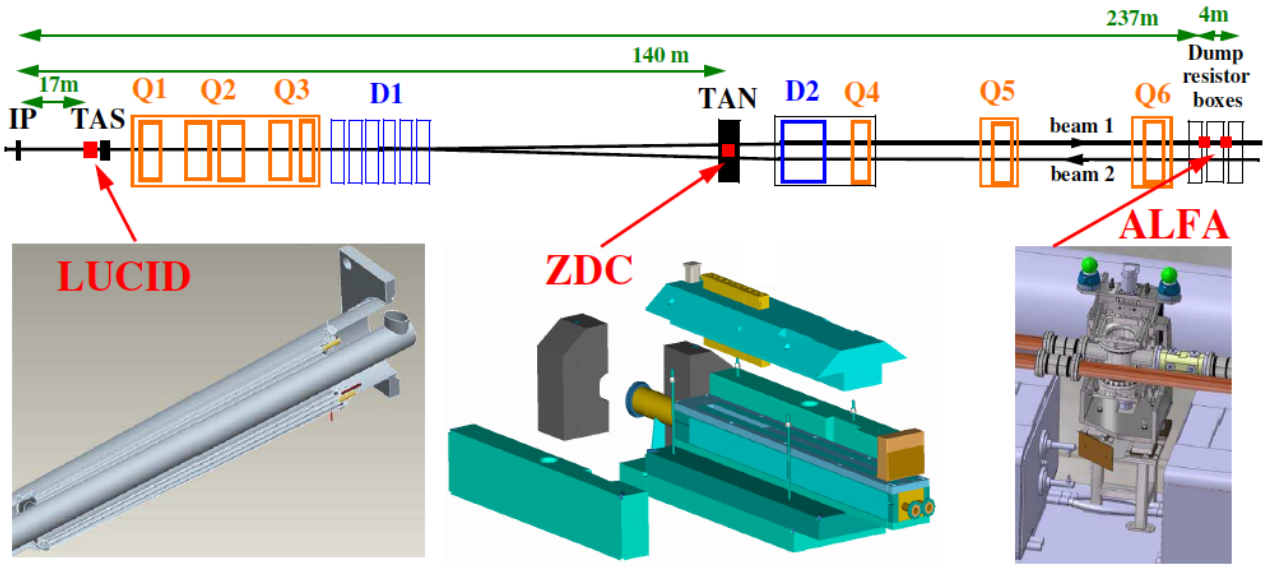

Figure 3.19: Illustration of the ATLAS Forward detectors [53]. LUCID, ZDC and ALFA are shown.

3.6.2 Absolute luminosity for ATLAS(ALFA)

The absolute luminosity has been determined via elastic scattering at even smaller angles (in case of ALFA, $< 3\mu$rad). in the Coulomb-nuclear interference region (CNI). The momentum transfer spectrum ($t = (p\Theta)^2$ distribution, where p is the beam momentum and Θ is the forward scatter angle) of the elastic proton scattering in small Θ is expressed as following:

$$\frac{dR_{el}}{dt} = \mathscr{L}\pi\left|-\frac{2\alpha}{|t|}+\frac{\sigma_{tot}}{4\pi}(i+\rho)e^{-b|t|/2}\right|^2, \tag{3.11}$$

where $\mathscr{L}$ is the luminosity, ρ is a ratio of real part to imaginary part of the scattering amplitude, σ_{tot} is the total proton-proton cross section and B is a slope parameter to be determined using the data. The ALFA data is fitted with four parameters ($\mathscr{L}$, ρ, σ_{tot} and B) to determine the absolute luminosity. The ALFA is a scintillating fibre detector housed in Roman Pots read out by Multi-Anode Photo-Multipliers (MAPMTs, Hamamatsu R7600). The pots are located 240 m away from the IP. The requirements on the spatial resolution is about 30 μm. Thus ALFA consists of 10 layers of U-V geometry (perpendicularly arranged) scintillator fibres with width of 0.5 mm. The U-V geometry provides a theoretical resolution of 14.4 μm ($\sigma = \sqrt{2}\times 500/\sqrt{12}/10\ \mu$m). The spatial detector resolution was determined to be 36 μm in both the x and y directions (resolution of 25 μm is expected in simulation). Measured luminosity is shown in Chapter 2. The uncertainty is 3% in 2012.

3.7 Trigger and data acquisition system

The LHC has achieved 70% of the designed instantaneous luminosity. The ATLAS can not record all the collisions produced by the LHC. Since the raw data size per event is approximately 1.3-1.6 Mbytes, the expected data rate would reach 1.5 PB/s (1.5 MB$\times\mathscr{L}\times\sigma$) to record all the data. In fact, production rate of interesting events is less frequent and most of the events are low energy multi-jet events produced in QCD interactions. The trigger system is designed to reduce the data rate from 1 GHz to 200 Hz without loosing interesting events. The promising signals to be triggered are events containing high transverse-momentum leptons, photons, τs and large $E_T^{\rm miss}$. Very high p_T jets and high multiplicity jets are available, since the event rate of 300 GeV jet is approximately same as W bosons decaying to the leptons at $\sqrt{s}$ =14 TeV. The data size is more than 3000 TByte annually. The ATLAS trigger system consists of three levels of trigger called Level 1 (L1), Level 2 (L2) and Event Filter (EF). The L1 trigger system has to make decision in 2.5 μs and reduces the event rate below 75 kHz. It consists of L1 Calorimeter trigger (L1Calo), L1 Muon trigger (L1Muon) and Central Trigger Processor

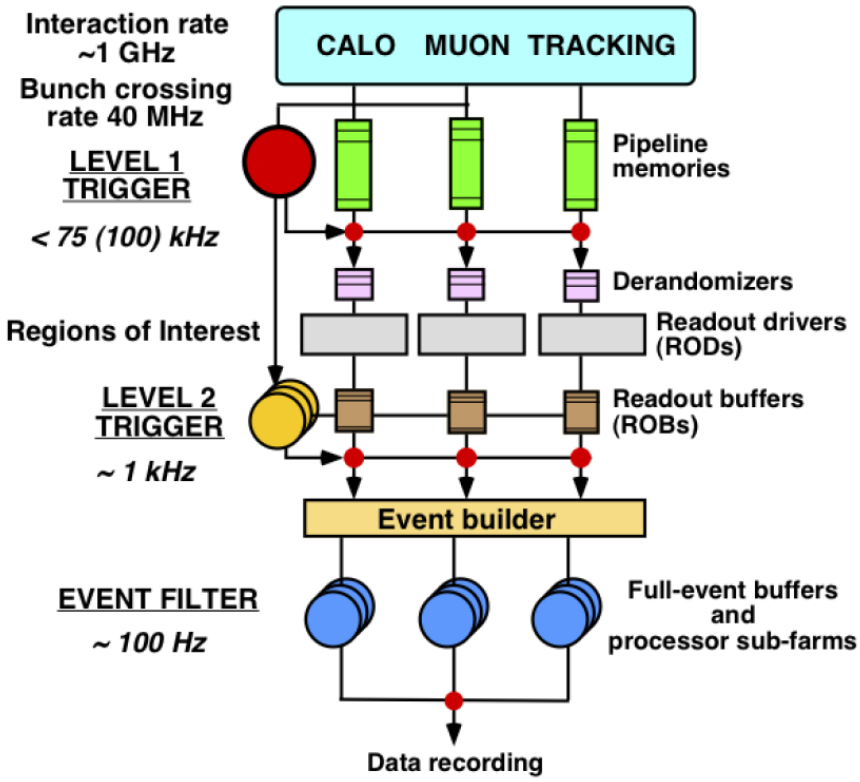

Figure 3.20: Schematic diagram of the ATLAS trigger system [61].

(CTP) based on custom processor (FPGAs and ASICs) electronics. The tracking information is not available at this level due to a heavy CPU load. The L1Calo makes decision based on the calorimeter data in restricted region called the Region of Interest (ROI). The basic tower granularity calorimeter tower, $\Delta\eta \times \Delta\phi = 0.1 \times 0.1$ in $|\eta| < 2.5$ and $\Delta\eta \times \Delta\phi = 0.2 \times 0.2$ to 0.4×0.4 in $2.5 < |\eta| < 4.9$. Local E_T maxima are searched in the 2×2 towers for triggering the electrons, photons and taus with 12 towers around the 2×2 towers used for the isolation calculation. For the jets, 4×4 to 8×8 tower RoIs summed over EM calorimeters and hadron calorimeters are available.

The L1Muon provides a muon momentum up to $|\eta| < 2.4$ using the information from the RPC and the TGC. Low p_T muon are triggered by inner two layers and high p_T moun triggered by outer two layers.

The CTP takes the information from L1Calo and L1Muon and makes a decision called L1 accept(L1A). The data is stored in front-end pipelines until CTP finishes sending an L1A signal. The L2 and EF are called high level trigger (HLT). Since usual linux computers and Giga-bit Ethernet hardware are available where necessary software algorithms are implemented from this stage. The level 2 trigger system is seeded by the RoI information. The detector information including the inner detectors are available only within the RoI with corresponding data size being $\approx$ 2% of the total. At this stage, the output rate is reduced to $\approx$3 kHz with a processing time of $\approx$ 40 ms/event. The EF makes a final decision within $\approx$4 seconds with reducing the record rate to $\approx$400 Hz. The EF algorithms are very close to the offline algorithms.

Chapter 4

Trigger

As we discussed in section 3.20, the ATLAS trigger system drastically reduces the data rate with retaining interesting signal events. The $VH(\rightarrow bb)$ signals are divided into three channels depending on their final states. They are zero-lepton, one-lepton and two-lepton channels and each channel focuses on $ZH\rightarrow\nu\nu bb$, $WH\rightarrow l\nu bb$ and $ZH\rightarrow llbb$ signals, respectively. Available triggers for each channel are different. The zero-lepton analysis uses large $E_{\mathrm{T}}^{\mathrm{miss}}$ as a trigger signal. Detail of the $E_{\mathrm{T}}^{\mathrm{miss}}$ trigger is discussed in subsection 4.0.1. The main triggers for the one-lepton channel are single electron trigger and single muon trigger, with additional $E_{\mathrm{T}}^{\mathrm{miss}}$ trigger useful to recover the inefficiency of the single muon trigger. Two-lepton mainly uses single electron and single muon triggers, bu di-electron and di-muon triggers are also available. The momentum threshold for each trigger is kept as low as possible. The electrons and muons produce a single isolated track in the tracker while hadrons are associated with many tracks. The track-based isolation requirement effectively reduces the background QCD interaction. Hence the isolated trigger can set the p_T threshold lower with maintaining same trigger rate. All the trigger used in this analysis is summarised in Table 4.1,4.2.

4.0.1 The $E_{\mathrm{T}}^{\mathrm{miss}}$ trigger

In 2012, three different $E_{\mathrm{T}}^{\mathrm{miss}}$ triggers were available and we combined them to maximise the acceptance, shown in Table 4.2. Successful L1Calo noise suppression in the forward region allowed $E_{\mathrm{T}}^{\mathrm{miss}}$80_loose trigger activated since May/21/2012. Approximately 90% of the data analysed in this analysis is recorded with this trigger. Before the activation, two triggers were available. The $E_{\mathrm{T}}^{\mathrm{miss}}$80T_loose trigger has a same threshold as $E_{\mathrm{T}}^{\mathrm{miss}}$80_loose, but it vetoes the first three bunches (BGRP7) in a bunch train. This BGRP7 mask is intended to suppress spurious high trigger rate bunches in $E_{\mathrm{T}}^{\mathrm{miss}}$ trigger due to the relatively long calorimeter response affecting the L1Calo The $E_{\mathrm{T}}^{\mathrm{miss}}$80 trigger has a higher threshold without BGRP7 mask. The trigger requirement in this analysis is following.

- if the data is recorded after May/21, require $E_{\mathrm{T}}^{\mathrm{miss}}$80_loose
- if $E_{\mathrm{T}}^{\mathrm{miss}}>160$ GeV, require $E_{\mathrm{T}}^{\mathrm{miss}}$80
- if $E_{\mathrm{T}}^{\mathrm{miss}}<160$ GeV, require $E_{\mathrm{T}}^{\mathrm{miss}}$80T_loose

Table 4.1: List of all triggers used in this analysis. Isolated lepton triggers are the main triggers in one-lepton and two-lepton analysis categories. The detail of 2012 $E_{\mathrm{T}}^{\mathrm{miss}}$ triggers is summarised in Table 4.2.

Trigger	threshold [GeV]	Zero-lepton	One-lepton	Two-lepton
Single isolated electron	24		×	×
Single electron	60		×	×
Di-electron	2×12			×
Single isolated muon	24		×	×
Single muon	36		×	×
Di-muon	2×13			×
$E_{\mathrm{T}}^{\mathrm{miss}}$	80	×	×	

Table 4.2: The list of three $E_{\mathrm{T}}^{\mathrm{miss}}$ triggers used in this analysis.

Trigger	Start Date	VBGRP7	L1 [GeV]	L2 [GeV]	EF [GeV]	Luminosity [fb^{-1}]
$E_{\mathrm{T}}^{\mathrm{miss}}$80	April/04/2012		50	55	80	18.1
$E_{\mathrm{T}}^{\mathrm{miss}}$80_loose	April/04/2012		40	45	80	2.1
$E_{\mathrm{T}}^{\mathrm{miss}}$80T_loose	May/21/2012	×	40	45	80	1.9

L1 $E_{\mathrm{T}}^{\mathrm{miss}}$ is calculated from RoI information discussed in Chapter 3. L2 $E_{\mathrm{T}}^{\mathrm{miss}}$ calculation uses cell-based energy sum from calorimeter read-out system. The topological clusters (See Chapter 5) are available from EF level and EF $E_{\mathrm{T}}^{\mathrm{miss}}$ is calculated as the vector sum of all topological clusters. The efficiency of the $E_{\mathrm{T}}^{\mathrm{miss}}$80 trigger at $E_{\mathrm{T}}^{\mathrm{miss}}$=160 GeV is almost 100%. Note that trigger level $E_{\mathrm{T}}^{\mathrm{miss}}$ calculation is fast but not precise enough, notably in L1. The $E_{\mathrm{T}}^{\mathrm{miss}}$ trigger turn on from $E_{\mathrm{T}}^{\mathrm{miss}}$=80 GeV and reach 100% around $E_{\mathrm{T}}^{\mathrm{miss}}$=160 GeV in view of offline $E_{\mathrm{T}}^{\mathrm{miss}}$ calculation. The turn on region (80<$E_{\mathrm{T}}^{\mathrm{miss}}$<160 GeV) contains a lot of signals. In order to use the events in this turn on region, $E_{\mathrm{T}}^{\mathrm{miss}}$ trigger efficiency is precisely measured. The trigger efficiency is a product of the trigger efficiencies in the three different trigger levels (L1, L2, EF). It is defined at each level as follows:

$$\mathrm{Eff}_{\mathrm{L1}} = \mathrm{L1}_{\mathrm{passed}}/\mathrm{Total} \tag{4.1}$$

$$\mathrm{Eff}_{\mathrm{L2}} = \mathrm{L2}_{\mathrm{passed}}/\mathrm{L1}_{\mathrm{passed}} \tag{4.2}$$

$$\mathrm{Eff}_{\mathrm{L3}} = \mathrm{EF}_{\mathrm{passed}}/\mathrm{L2}_{\mathrm{passed}} \tag{4.3}$$

$$\mathrm{Eff}_{\mathrm{total}} = \mathrm{Eff}_{\mathrm{L1}} \times \mathrm{Eff}_{\mathrm{L2}} \times \mathrm{Eff}_{\mathrm{EF}} \tag{4.4}$$

To measure these using the data, orthogonal samples acquired by the muon trigger have been used. Since the muon momentum is not counted in the on-line trigger $E_{\mathrm{T}}^{\mathrm{miss}}$ calculation. The $E_{\mathrm{T}}^{\mathrm{miss}}$ trigger turn on for $W\to\mu\nu$ and $Z\to\mu\mu$ are quite similar to $Z\to\nu\nu$. The $E_{\mathrm{T}}^{\mathrm{miss}}$ trigger efficiencies at the L1, the L2 and the EF are measured using $W(\to\mu\nu)$+jets or $Z(\to\mu\mu)$+jets events in the muon triggered data, The event selection for $W\to\mu\nu$ + jets and $Z\to\mu\mu$ + jets processes are quite similar to the cut-base analysis selections (see next section). Additionally, tight multi-jet rejection cuts, track isolation<3% and m_{T}^{W}>60 GeV, and b-jet veto are applied for $W\to\mu\nu$ events, to remove residual multi-jet and $t\bar{t}$ backgrounds. With the above selections applied, $W\to\mu\nu$ and $Z\to\mu\mu$ events are selected at nearly 100% purity. Figure 4.0.1 shows the strong correlation the scalar sum of p_T^{jets} and the $E_{\mathrm{T}}^{\mathrm{miss}}$ trigger efficiency. The other variables have almost no bias in the signal region. The efficiency measured with simulated data can not explain the efficiency measured with data. The scalar sum of p_T^{jets} > 120 (150) GeV is required to remove this biased region for 2-jet (3-jet) events. Finally,

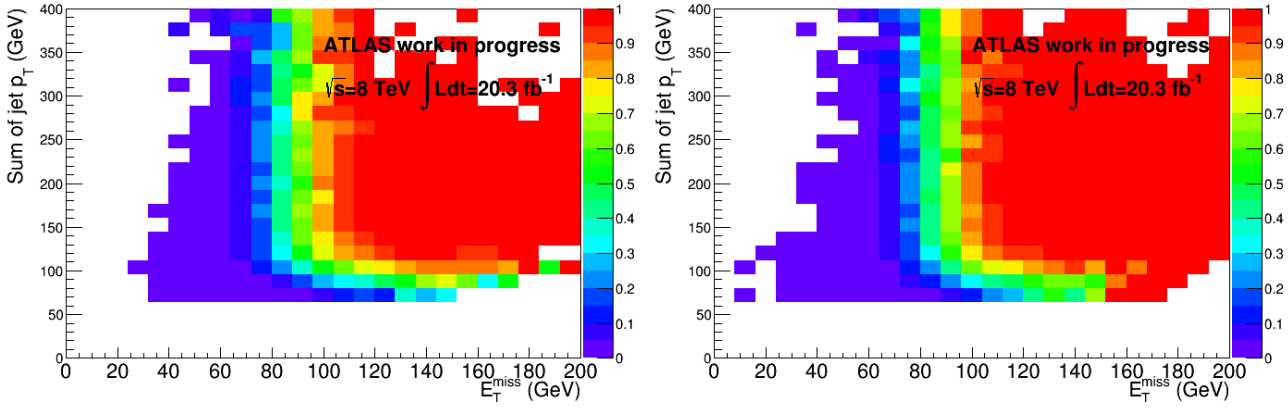

Figure 4.1: $E_{\mathrm{T}}^{\mathrm{miss}}$80T_loose trigger efficiency with respect to the scalar sum of p_T^{jets} and $E_{\mathrm{T}}^{\mathrm{miss}}$ in data (left) and in simulated data (right).

$E_{\mathrm{T}}^{\mathrm{miss}}$ trigger scale factor is calculated using the measured efficiencies. Each level of efficiency turn-on curve is parameterised using an error function to reduce the statistical uncertainty (See figure 4.0.1).

$$\mathrm{Efficiency} = \frac{1}{2}\left(1 + Erf\left(\frac{E_{\mathrm{T}}^{\mathrm{miss}} - \mathrm{threshold}}{\sqrt{2}\mathrm{width}}\right)\right) \tag{4.5}$$

where "threshold" denotes the trigger threshold and "width" corresponds to the rms spread of differencen of trigger $E_{\mathrm{T}}^{\mathrm{miss}}$ and off-line $E_{\mathrm{T}}^{\mathrm{miss}}$ distributions. The scale factor (SF = $\mathrm{Eff_{data}}/\mathrm{Eff_{MC}}$) is calculated using $E_{\mathrm{T}}^{\mathrm{miss}}$

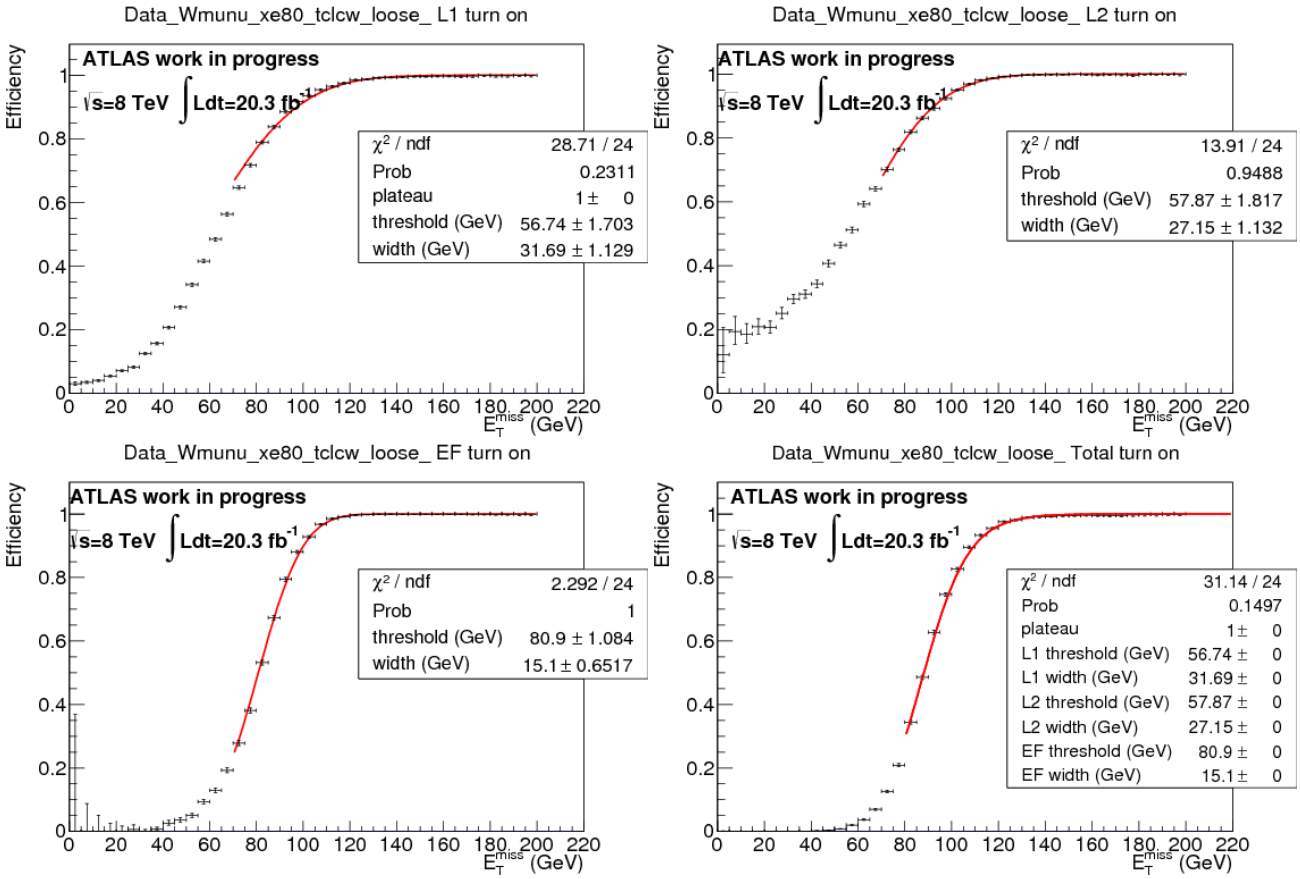

Figure 4.2: $E_{\mathrm{T}}^{\mathrm{miss}}$80T_loose trigger efficiency for $W\to\mu\nu$ events at L1 (top left), L2 (top right), EF (bottom left) and total (bottom right) are shown. Red curves are parameterised $E_{\mathrm{T}}^{\mathrm{miss}}$ trigger turn on curve.

trigger efficiency for $W\to\mu\nu$ and $Z\to\mu\mu$ events. The $W\to\mu\nu$ scale factor ($\mathrm{SF_W}$) is used as a nominal scale factor and derivation of $Z\to\mu\mu$ scale factor ($\mathrm{SF_Z}$) from the nominal is considered as a systematic uncertainty. Two scale factors are consistent in signal region ($E_{\mathrm{T}}^{\mathrm{miss}}$>100 GeV), the estimated systematic uncertainty is negligible.

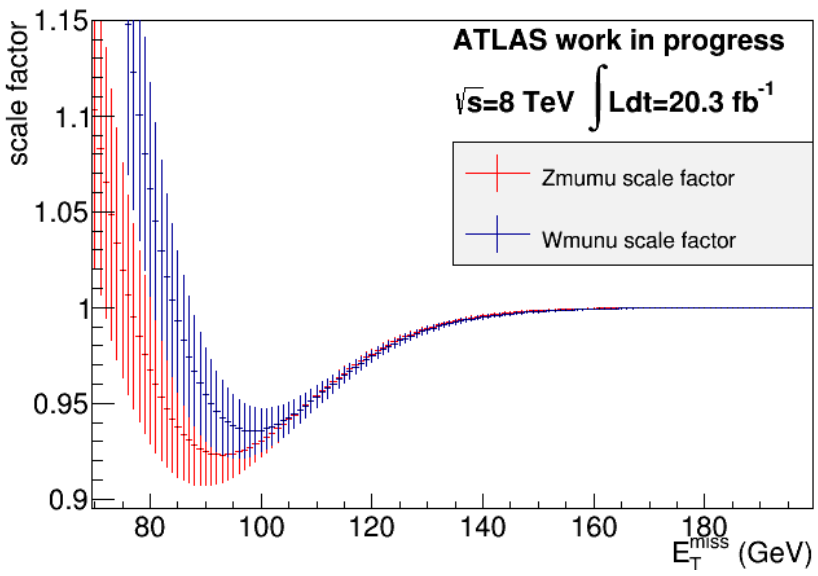

Figure 4.3: $E_{\mathrm{T}}^{\mathrm{miss}}$ trigger scale factor for $W \to \mu\nu$ events (blue) and for $Z \to \mu\mu$ events (red).

Chapter 5

Definition of physics objects

5.1 Particle categorisation

On the collision of two beams, many particles are created. The ATLAS detector identifies the particles and reconstructs the event using dedicated algorithms suitable for each object (electron, muon and jet etc.). The raw data recorded with all the detector elements are fully utilised. In this process, specific requirements are imposed to the reconstructed objects to maximise the analysis sensitivity. Each object is independently reconstructed and selected. Since in some case the object rarely overlaps. After this object level selection is passd, object overlaps are removed. Finally the event is analysed using the redefined objects.

5.2 Tracking and vertex reconstruction

The track reconstruction is performed mainly in an "inside-out" strategy. Track finding starts from the semiconductor detector and then extends the trajectory of successfully fitted track to the TRT to reconstruct as a full inner detector track. The track is parameterised at the point of closest approach with the global z-axis using five perigee parameters (d_0:the transverse impact parameter, z_0:the longitudinal impact parameter, ϕ_0: the azimuth angle, θ: the polar angle and q/p: the charge over momentum magnitude). There are two track fitting methods, the global least-squares fit and the Kalman filter. Both track fitting methods show a performance identical to each others. In the 2011-2012 data taking periods, 10-40 vertices are produced at one beam crossing. The ATLAS analysed such overlapping events and determined the most hardest collision in all as the event with "primary vertex". Several particles which have measurable lifetimes (bottom-quark hadrons, charm-quark hadrons and τ leptons etc.) produceing additional vertices in their decay processes. The vertex produced by the particle decay is named "secondary vertex". Reconstructing the secondary vertex is crucial to identify the jet as bottom-quark originated jet. Vertex finding and fitting to calculate the vertex position are important in this analysis. Several vertex fitting methods have been implemented. One of them is the Billoir vertex fitting method [62].

5.3 Electron

Electrons are reconstructed with the following processes:

- Find a cluster seed through a sliding window algorithm (scan the calorimeter energy sum in a fixed window size) [63]
- Match the cluster to a high momentum track
- Examine if the matched track has a secondary vertex (mainly for photon conversion)
- Rebuild the cluster in an optimised cluster size
- Compute the electron energy
- Apply calibrations

The above algorithm starts from the EM clusters. There is another algorithm to start from the ID tracks, which is effective for low momentum electron reconstruction. Three categories are defined for the reconstructed electrons. In the increasing order of purity, they are named as loose, medium and tight. Loose electrons are required to have a transverse energy $E_T > 7$ GeV and electron cluster η $|\eta_{clus}| < 2.47$. Loose electrons have to satisfy a very loose likelihood identification criterion [64].Very loose likelihood identification can achieve a better identification efficiency compared to a cut-based ID while keeping same QCD rejection. Energy leakage in the hadron calorimeters, shower shape in the EM calorimeter segments and track information are used to construct the likelihood. Track-based isolation is defined such that the scalar sum of all tracks ($p_T > 1$ GeV) momenta within $\Delta R = 0.2$ except electron in concern must be less than 10% of the electron E_T. Various corrections including electron identification scale factor, reconstruction scale factor, isolation scale factor, energy resolution correction and energy scale correction are applied. They are estimated using Z$\rightarrow$ ee, W$\rightarrow$ eν and J/$\psi \rightarrow$ ee events [65].Medium electrons additionally required to have a transverse energy $E_T > 25$ GeV, to take into account the single lepton trigger threshold of $E_T > 24$ GeV. Tight electrons have to satisfy tighter track-based isolation and calorimeter-based isolation to further remove fake electrons. The track-based isolation threshold is set tighter to 4% of the electron E_T. The calorimeter-based isolation is to require scalar sum of all topological cluster (see Jet section) energies within $\Delta R = 0.3$ except electron in concern must be less than 4% of electron E_T. The topological-cluster-based isolation is corrected for both the leakage energy and event pileup. The pileup contribution is corrected by subtracting event-by-event ambient energy density. Systematic uncertainties on electron energy measurement (scale and resolution), isolation and identification selection are considered.

5.4 Muon

The Inner detector (ID) and muon spectrometer (MS) are able to reconstruct muons independently. The ID has a better resolution for low momentum muons. Complementary, the MS is good at high momentum muon measurement. To improve the overall performance of momentum measurement, an ID reconstructed muon and a MS reconstructed muon are combined. There are two types of muon reconstruction algorithm chains in ATLAS. STACO chain combines an ID track with a MS track using a statistical method. Muid chain combines an ID track with a MS track using a global refit of the two tracks. This analysis uses Muid muons. The Muid muon reconstruction chain contains the muon found by four different algorithms.

- Muid combined algorithm combines an inner detector track with a muon spectrometer track using a global refit of the two tracks.
- Muid standalone algorithm starts from hit information in the MS and produces standalone segments of tracks. Then the standalone track segment is extrapolated to the vertex while a vertex constraint is used to determine the track parameters. This algorithm requires $|\eta| > 2.5$ and the MS track must have at least three hits in precision tracking stations (MDT, CSC).
- Muid tagged algorithm identifies muons by association an inner detector track with MS segments. Tagged muons must have at least two hits or less than six miss-hits in precision tracking stations.

The MS has a dead region in $|\eta| < 0.1$. To recover the muons in this MS inefficient region, calorimeter muon algorithm is additionally applied. Calorimeter muon algorithm reconstructs and selects well isolated tracks associated to the primary vertex, then calculates the energy deposit in the hadronic calorimeter. If the deposit energy is consistent with that of a minimum ionising particle, such a track is identified as a muon. Same as for electrons, three categories (loose, medium and tight) of muons are defined. Following selections are required to the loose muons. Combined muons and tagged muons are required to have ID hits and satisfy impact parameter selection. Muid muons are required to have a transverse momentum $p_T > 7$ GeV and $|\eta| < 2.7$. Muid muons have to satisfy tight muon identification criterion. Track-based isolation is calculated using all track ($p_T > 1$ GeV) momenta within $\Delta R = 0.2$ except muon itself. We require Σp_T must be less than 10% of muon p_T. The calorimeter-tagged muons are also required to have ID hits and pass impact parameter and track-based isolation requirements with p_T threshold increased to $p_T > 20$ GeV and η in a MS inefficient region $|\eta| < 0.1$. The calorimeter-tagged muons must pass tighter identification criterion and have a high calorimeter-muon likelihood value. Medium muons are reconstructed by the Muid combined algorithm or Muid tagged

algorithm for $p_T > 25$ GeV. For the tight muons, same as for electron case, track-based isolation requirements are tightened and calorimeter-based isolation is required. The measured muon momentum and efficiency are calibrated using Z$\rightarrow \mu\mu$, W$\rightarrow \mu\nu$ and J/$\psi \rightarrow \mu\mu$ [66]. The systematic uncertainties are considered on muon momentum resolution (independently for ID and MS), isolation and identification selections.

5.5 Jets

The jet reconstruction starts from building three-dimensional topological clusters.

- Find a seed cell which has signal to noise ratio (S/N: energy over noise) greater than a seed threshold (t_{seed}) [63].
- If a neighbouring cell has, if it is not another seed, S/N$> t_{\text{neighbour}}$, the neighbouring cell is added to the seed cell.
- If a neighbouring cell has $t_{\text{cell}} <$S/N$< t_{\text{neighbour}}$, the cell is added but the cluster finding procedure is terminated.
- Repeat the neighbouring cell search until the cluster is surrounded by low S/N cells (S/N$> t_{\text{cell}}$).
- Clusters with multiple local maxima are split into subclusters.

The three thresholds are chosen as $(t_{\text{seed}}, t_{\text{neighbour}}, t_{\text{cell}}) = (4,2,0)$ for jets ((6,3,3) for photons and electrons). The energy deposited in the clusters are calibrated for the electromagnetic scale extracted from Z$\rightarrow$ee and electron test beam results. The jets are reconstructed using the anti-k_T algorithm [67] with radius $R = 0.4$. The anti-k_T algorithm uses distances:

$$d_{ij} = min\left(k_{ti}^{-2}, k_{tj}^{-2}\right)\frac{\Delta_{ij}^2}{R^2}, \tag{5.1}$$

$$d_{iB} = k_{ti}^{-2}, \tag{5.2}$$

where $\Delta_{ij}^2 = (y_i - y_j)^2 + (\phi_i - \phi_j)^2$ and k_{ti}, y_i and ϕ_i are the transverse momentum, rapidity and azimuth of particle i, respectively. The procedure is following.

- Calculate d_{ij} and d_{iB} for all topological clusters.
- If the minimum value is d_{ij}, combine the clusters i and j.
- If the minimum value is d_{iB}, i is defined as a jet
- Repeat the above processes

Then, reconstructed EM scale jet is corrected to the jet (hadron) energy scale by a numerical inversion procedure. Finally, jet level calibrations (pileup, jet energy and direction corrections) are applied. In 2012, two new calibration techniques are employed, jet-area-based calibration and global sequential calibration. Jet-area based calibration corrects for the contribution of pileup interaction. Global sequential calibration corrects for the jet response dependent on the fraction of energy deposited in the first segment of the tile calorimeter, the one deposited in the third segment of the EM calorimeter, the track multiplicity and the track width of the jet [68], defined as

$$w_{track} = \frac{\sum_{all\ tracks} p_T^{trk} \Delta R(jet, trk)}{\sum_{all\ tracks} p_T^{trk}}. \tag{5.3}$$

Two types of jets are defined to maximize the sensitivity, the signal jets are optimized to reconstruct jets from higgs and the veto jets are optimized to veto forward jets to remove $t\bar{t}$ background. The signal jets are required to have a calibrated transverse momentum $p_T > 20$ GeV for $|\eta| < 2.5$. The veto jets are required to have a momentum $p_T > 30$ GeV for $2.5 < |\eta| < 4.5$ adding to the signal jets. To reduce the pileup originate jets, Jet-Vertex Fraction (JVF) is calculated by combining tracks and their primary vertices associated with calorimeter

jets [69]. The JVF is defined as the ratio of the scalar sum of the transverse momenta of all tracks matched to the jet and the sum of those originating from the primary vertex. If the jets satisfy $p_T < 50$ GeV and $|\eta| < 2.5$ and have associated tracks, JVF>0.5 is required to remove pileup jets. Uncertainty on jet energy scale (JES) has been broken down to 18 components in 2012, the mythology being similar to the one in 2011 [70]. The 47 uncertainties from in-situ calibration (Z+jets, γ+jets and multi-jet p_T balance) are combined into 6 parameters. We add two components for η-inter-calibration (Pythia-Herwig comparison). After the calibration, the jet energy and p_T response still show slight deviations from unity at low p_T (non-closure). This is mainly due to the application of the same correction factor for the jet energy with respect to p_T. Additional one components is due to the MC non-closure, and four components are related to the pileup. Additional four components are considered taking uncertainties for jet flavour. Two are for the b-jet response and μ/ν energy from the b-jet (only for the truth b-jet) and other two are for the light jet fraction and response (only for the non truth b-jet). Two uncertainties on jet energy resolution are considered. One is for the jet energy resolution and additional uncertainty for b-jet resolution (only for the truth b-jet). The JVF efficiency uncertainty is also considered.

5.6 Overlap removal

The reconstruction algorithms is applied independently to identify electron, muon and jet. Occasionally the same detector signal is reconstructed as more than one object. For example, a b-jet can decay into muons, and such a b-jet is reconstructed as a jet and also as a muon. In this case, the muon is a part of the b-jet, thus we define it is a jet.

- if there is a jet close to an electron within $\Delta R < 0.4$, the object is regarded as an electron.
- if there is a jet near a muon within $\Delta R < 0.4$, the object is regarded as a muon if the jet has less than three tracks of $p_T > 500$ MeV.
- if there is a jet next to a muon within $\Delta R < 0.4$, the object is regarded as a jet if the jet has more than three tracks of $p_T > 500$ MeV.
- if an electron and a muon are separated by $\Delta R < 0.2$, the object is regarded as a muon except if it is a calorimeter-tagged muon, in which case it is regarded as an electron..

Jet-muon overlap removal is crucial in this analysis, since b-quark decays into a muon, which should be considered as a part of the b-jet.

5.7 Missing transverse momentum

The missing transverse momentum, $E_{\mathrm{T}}^{\mathrm{miss}}$ is defined as a momentum imbalance in a transverse (x-y) plane. It is calculated as the negative vector sum of all fully calibrated objects (jet, electrons, muons, τ leptons and photons) and topological clusters which are not associated to the reconstructed objects. The object selection and overlap removal for $E_{\mathrm{T}}^{\mathrm{miss}}$ calculation is re-optimised to maximise the performance. Electron and muon calibrations are propagated. Jet calibration is slightly changed such that jets are calibrated by the local hadron calibration with area correction. The contributions of the clusters outside the object (soft term) are additionally considered [71]. All the systematic variations related to the physics objects are propagated. They are two additional uncertainties on the resolution and scale of a soft term.

5.7.1 Track-based missing transverse momentum

$E_{\mathrm{T}}^{\mathrm{miss}}$ is calculated using clusters and physics objects. The track-based missing transverse momentum ($p_{\mathrm{T}}^{\mathrm{miss}}$) is calcualted using selected tracks (it doesn't have cluster information). The tracks are required to have $p_{\mathrm{T}} >$ 0.5 GeV, $|\eta| < 2.4$, at least one pixel hits, at least six SCT hits, d_0 <1.5 mm and $z_0 \sin(\theta)$ <1.5 mm. The $p_{\mathrm{T}}^{\mathrm{miss}}$is calculated as a vector sum of all selected tracks.

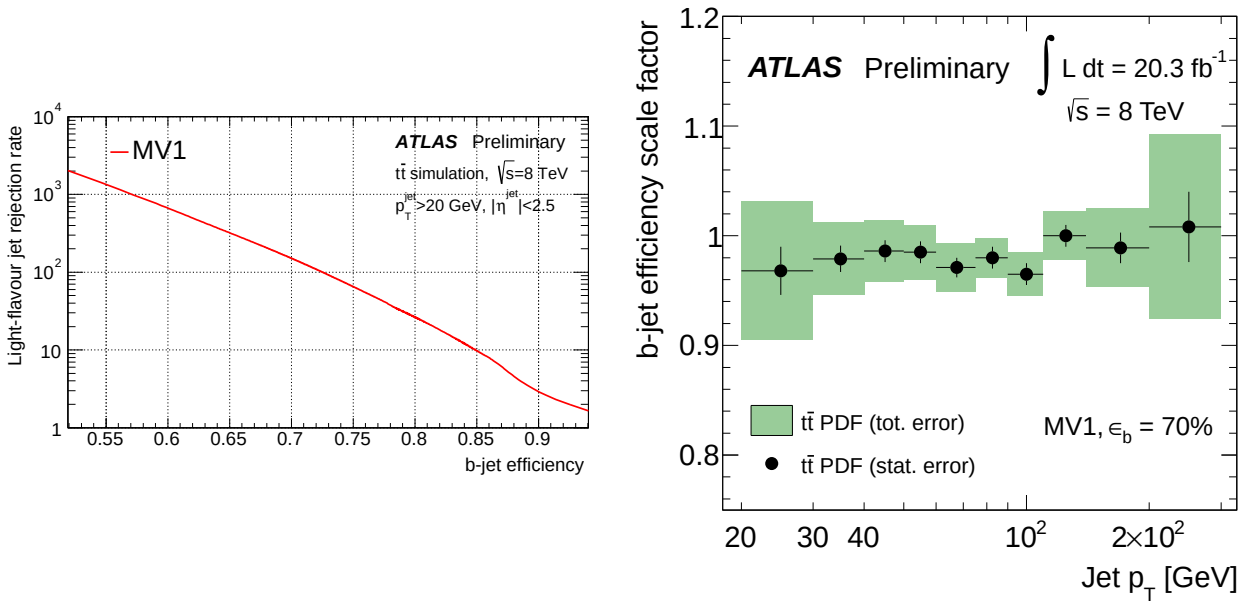

Figure 5.1: The light-flavour rejection factor with respect to the b-jet tagging efficiency (left) [72] and the b-tag efficiency scale factor with the 70% tagging efficiency (right) [73]. The scale factor is measured with a combinatorial likelihood approach.

5.8 Flavor tagging

Bottom quark has unique features. B-hadrons have lifetime of $c\tau_{\mathrm{b-hadrons}} \sim 450\ \mu$m and large mass ($m_b = 4.2$ GeV). Due to such a specific nature, b-hadrons leave a characteristic trace on the tracking system. In the ATLAS experiment, several b-tagging algorithms have been developed to tag the b-quark origin jet (b-jet). They range from relatively simple algorithms based on three dimensional impact parameter (IP3D) and secondary vertex information (SV1) to more refined JetFitter algorithm. JetFitter accesses the topology of weak b- and c-hadron cascade decays inside the jet. It finds a common flight line for the B and D hadrons on which the primary vertex, secondary and tertiary vertices are fitted using a Kalman filter. It gives an approximated flight path for the b-hadron. The log-likelihood ratio using above information defines the "b-tagging weight". To improve the b-tagging efficiency and light jet rejection, obtained log-likelihood ratios are combined using a multivariate technique. JetFitter and IP3D tagger outputs are combined using artificial neural network techniques (JetFitterCombNN). Most advanced algorithm "MV1" is a neural network-based algorithm that uses the IP3D, SV1 and JetFitterCombNN as inputs. "MV1c" is used in this analysis [74–76], which is technically similar to "MV1", by it is trained also against c-jet. It achieves improved c-jet rejection and comfortable light-jet rejection for a same b-jet tagging efficiency. Four b-tagging operation points are defined, corresponding to average b-jet tagging efficiencies of 80%, 70%, 60% and 50% for selected jets in $t\bar{t}$ Monte Carlo (MC) events. Figure 5.1 shows the performance of the MV1 b-tagging algorithm. The MV1c b-tagging algorithm shows enough performance for the light jet rejection and better performance for the charm jets. The better charm jet rejection supresses the impact of larger systematic uncertainty of charm jet tagging rate. In this analysis, 80%, 70% and 50% operating points are denoted loose, medium and tight. Rejection factors at these three working points are 29.12, 135.76 and 1388.28 for light jets and 3.04, 10.45 and 26.22 for charm jets, respectively. The b-tagging efficiencies for b-jets and c-jets and mistag rate for light jets are measured in both data and simulation using dedicated event samples. The b-jet tagging efficiency is measured using $t\bar{t}$ events [73]. For the c-jet tagging efficiency, reconstructed D* mesons are used. For the mistag rate for light-jets is measured by negative tag method in an inclusive QCD jet sample [72]. The flavour inclusive negative tag rate obtained by reversing the sign of impact parameter and decay length for the MV1c tagging weight calculation. The mistag rate is calculated using the flavour inclusive negative tag rate $\varepsilon_l = \varepsilon_l^{neg} k_{\mathrm{hf}} k_{\mathrm{ll}}$. The two correction factors, $k_{\mathrm{hf}} = \varepsilon_l^{neg}/\varepsilon_{inc}^{neg}$ and $k_{\mathrm{ll}} = \varepsilon_l/\varepsilon_l^{neg}$ are estimated using simulation, where ε_l^{neg} is the negative tag rate for light jets and ε_l is the light jet mistag rate. Then the difference between data and simulation is corrected by the scale factors within intervals between two operating points (Figure 5.1). The uncertainties on b-tag scale factors are considered separately for b-jets,

c-jets and light-jets. These uncertainties are the mixture of all experimental errors such as jet energy scale uncertainties, theoretical errors and statistical errors. Most significant 10, 15 and 10 uncertainty components are considered for b-jets, c-jets and light-jets, respectively. Other small uncertainties are negligible. A MC generator dependence on b-jet efficiencies is observed. To correct the generator dependence on b-jet efficiencies, additional scale factors and their uncertainties are applied for Sherpa and Pythia8 samples (Pythia6 taken as nominal).

5.8.1 Truth tagging

In this analysis as explained in Chapter 6, signal events are required to have two b-tagged jets. The miss-tag rate for two light jet events are $\approx 0.1\%$. The b-tagging weight for simulation is calculated from simulated track information same as data (*Direct tagging*). Untagged events are discarded at the event selection. In this method, 99.9% of the produced light jet events do not contribute to fall in the signal region. On the other hand, light jet events have a larger cross section compared to the heavy flavor jet events. Therefore it is difficult to produce MC sample with enough number of events, and samples with poor simulation statistics result in a big statistical fluctuation and some spikey distributions which does not allow meaningful evaluation of the uncertainty. To solve this problem, *Truth tagging* method is employed. *Truth tagging* tags method provide a event weight instead of tagging the jet. The tagging efficiency is prepared as a function of p_T and η. All the events pass the b-tag requirement and are applied the weight calculated from the tagging efficiency.
For instance, if we prepare 1000 two light jet events, only one event satisfy two b-tag requirement with direct tagging, on the other hand, 1000 events pass the b-tag requirement but all events weighted to 0.001 with truth tagging.
This method shows some bias on the $\Delta R(j,j)$ distribution for two-c-jet events. Correction is applied to compensate this bias with half the correction magnitude taken as the systematic uncertainty.

5.9 b-jet energy correction

Semileptonic b-quark decay could produce a muon. Jet reconstruction algorithm does not consider the muon contribution. The "mu-in-jet correction" improves the b-jet energy resolution and its scale. The following muon selection has been applied to the muons reconstructed inside a jet.

- $p_T > 4$ GeV
- $\Delta R(\mu, \text{jet}) < 0.4$
- tight muon identification criterion
- standard tracking requirements

If the muon satisfies the above criteria, the muon momentum vector is added to the jet vector. The energy deposited by the muon in the calorimeter is removed to avoid double counting. Additionally, "p_T-*reco*" correction is applied to compensate for the bias caused by energy migration in reconstruction of energy. In the two-lepton channel, kinematic likelihood fitting is performed to improve the di-jet mass resolution. The four momenta of two leptons and two jets are used in the kinematic fit. Intrinsically, the vector sum of the above four objects is zero (balanced) where lepton energy resolution is much better than the jet. Kinematic fit constrains the jet energy using the four momentum of leptons. The mu-in-jet plus "p_T-*reco*" and the kinematic likelihood fit improve the di-jet mass resolution by 14 % and 30 %, respectively.

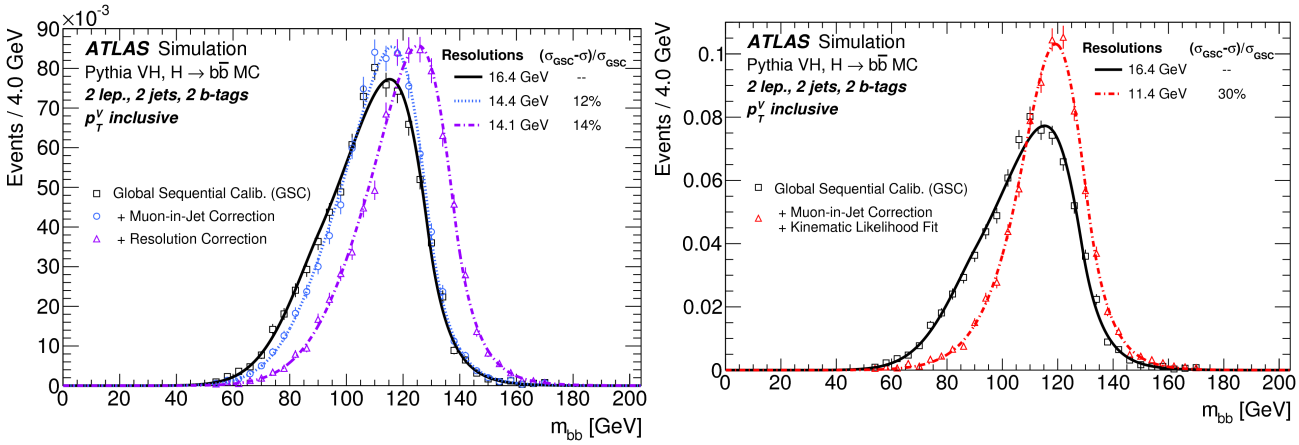

Figure 5.2: The mu-in-jet plus "p_T-*reco*" (left) and the kinematic likelihood fit (right) improve the di-jet mass resolution by 14 % and 30 %, respectively.

object	p_T(GeV)	η_{max}	identification	calo/track isolation	comment
Loose electron	>7	2.47 (cluster)	VeryLoose LH	$<0.1/-$	
Medium electron	>25	2.47 (cluster)	VeryLoose LH	$<0.1/-$	
Tight electron	>25	2.47 (cluster)	VeryTight LH	$<0.04/0.04$	
Loose muon	>7	2.7	Tight	$<0.1/-$	ID hits, d_0 and z_0
Calo muon	>20	0.1	CaloID	$<0.1/-$	ID hits, d_0 and z_0
Medium muon	>25	2.5	Tight	$<0.1/-$	ID hits, d_0 and z_0
Tight muon	>25	2.5	Tight	$<0.04/0.04$	ID hits, d_0 and z_0
Signal jet	>25	2.5	-	$\|$JVF$\|<0.5$	
Veto jet	>30	$2.5-4.5$	-	$\|$JVF$\|<0.5$	+signal

Table 5.1: Summary of the reconstructed objects. The transverse momentum threshold and η range, object identification categories and isolation thresholds are summarised.

Chapter 6

Event selection

6.1 Common event cleaning

To remove problematic events from the data/MC, certain cleaning cuts are applied. For the data, good quality data quality (DQ) flag is required. This flag ensures that all sub-detectors including all trigger systems are operated soundly. Events are required to have a main primary vertex reconstructed from at least 3 tracks. Any events containing unphysical jets with $p_{\mathrm{T}} > 20$ GeV in $|\eta| < 4.5$ (without JVF cut) are removed. Unphysical jets arise due to hardware problems (HEC spikes and EM coherent noise), LHC beam instability and cosmic-ray showers. Such unphysical jets produce a fake $E_{\mathrm{T}}^{\mathrm{miss}}$. In the data taking periods B1 and B2 in 2012, there was a hot tile calorimeter cell that had not been masked in the reconstruction. Those events with such spurious jets are removed. There were a noise burst in the LAr calorimeter and HV trips in a few tile calorimeter channels. Affected bad events and corrupted events are rejected. MC events are normalised to the data luminosity. The amount of discarded events by data cleaning is considered in the luminosity calculation.

6.2 Search channel definition

To maximise the sensitivity to the signal, events are separated into three channels depending on the number of loose leptons in the events. The cut values to define the event samples are summarised in Table 6.1 for both cut-based analysis and MVA analysis, which are described to detail in the following. Loose lepton rejects $t\bar{t}$ background from zero-lepton event sample and maximises the acceptance for the two-lepton channel. The selection for zero, one and two lepton channels are optimised using $Z^0H \to \nu\bar{\nu}b\bar{b}$, $W^{\pm}H \to \ell^{\pm}\nu b\bar{b}$ and $Z^0H \to \ell^+\ell^- b\bar{b}$ signals. Each lepton category is divided into several sub-categories. The number of jets in event is exactly two at the tree level signal diagram. The fraction of three-jet final state is non negligible. Third jet is produced due to initial state radiation (ISR) and final state radiation (FSR). Two-jet and three-jet events are analysed separately. Transverse momentum of vector boson p_{T}^V is also important to optimise the event selection, since the S/N and m_{bb} resolution are improved with increasing p_{T}^V. For the MVA analysis, high p_{T}^V ($p_{\mathrm{T}}^V > 120$ GeV) and low p_{T}^V ($p_{\mathrm{T}}^V < 120$ GeV) event samples are defined. For the cut-based analysis, 5 p_{T}^V bins are defined to optimise $\Delta R(jet_1, jet_2)$ cut. Additionally, the flavors of the leading and sub-leading jets are used to define the sub-categories: one-b-tagged events are used to evaluate the flavor fraction in the two-b-tagged region. Two-b-tagged events are divided into 3 b-tag categories: tight-tight (TT), medium-medium (MM) and loose-loose (LL). These b-tag categories are exclusively defined to each others. If both two b-jets satisfy 50% efficiency b-tagging working point, the event is categorised as TT. The remaining events with 2 b-jets satisfying 70% efficiency b-tagging working point are categorised as MM. Remaining two b-jets events are categorised as LL. If the third leading jet is b-tagged, such a three-b-tagged events are discarded to remove $t\bar{t}$ background, since charm jet from $t\bar{t}$ decay can also be mistakenly b-tagged.

6.3 Event selection for cut-based analysis

6.3.1 Zero-lepton channel

In the zero-lepton channel, the event level selection aims at suppressing the multi-jet background. Track-based missing transverse momentum cut $p_{\mathrm{T}}^{\mathrm{miss}} > 30$ GeV is very useful to remove beam-induced backgrounds.

Intrinsically, multi-jet background does not exhibit significant $E_{\mathrm{T}}^{\mathrm{miss}}$, so reconstructed $E_{\mathrm{T}}^{\mathrm{miss}}$ is due to mis-measurement by the calorimeter and/or contribution from pileup interactions. On the other hand, $p_{\mathrm{T}}^{\mathrm{miss}}$ is measured by the tracker which has a better spatial resolution compared to the calorimeter (of course neutral component is missed). The azimuthal angle of well measured $E_{\mathrm{T}}^{\mathrm{miss}}$ should be close to the azimuthal angle of $p_{\mathrm{T}}^{\mathrm{miss}}$. The azimuthal angle cut between $E_{\mathrm{T}}^{\mathrm{miss}}$ and $p_{\mathrm{T}}^{\mathrm{miss}}$ cut $\Delta\phi(E_{\mathrm{T}}^{\mathrm{miss}}, p_{\mathrm{T}}^{\mathrm{miss}}) < \pi/2$ removes multi-jet background without loosing signal events. For the high p_{T}^{V} category, following cuts are applied to remove multi-jet background. In real $E_{\mathrm{T}}^{\mathrm{miss}}$ ($Z^0 \to \nu\overline{\nu}$) case, $E_{\mathrm{T}}^{\mathrm{miss}}$ is measured in the opposite direction of two jets. In fake $E_{\mathrm{T}}^{\mathrm{miss}}$ case, mis-measured jet is observed close to the $E_{\mathrm{T}}^{\mathrm{miss}}$ direction. Since the signal events have 2 or 3 jets, the azimuthal angle between $E_{\mathrm{T}}^{\mathrm{miss}}$ and each jet is calculated. Then the events having a jet with $\Delta\phi(E_{\mathrm{T}}^{\mathrm{miss}}, p_T^{\mathrm{jet}}) < 1.5$ are removed. Also $\Delta\phi(E_{\mathrm{T}}^{\mathrm{miss}}, \text{di-jet}) > 2.8$ is required. For the low p_{T}^{V} category, multi-jet background rejection is re-optimised. The $\Delta\phi(E_{\mathrm{T}}^{\mathrm{miss}}, \text{di-jet})$ cut threshold is loosened to 2.2 and additionally $\Delta\phi(\mathrm{jet}_1, \mathrm{jet}_2) < 2.7$ and $E_{\mathrm{T}}^{\mathrm{miss}}$ significance > 7.0 are required, E_T^{miss} significance is defined as the ratio of $E_{\mathrm{T}}^{\mathrm{miss}}$ to the square root of the sum of leading two jet transverse momenta. Above selection effectively suppresses the multi-jet background without loosing signal. But the remaining multi-jet contamination is non-negligible at this level. A likelihood technique is employed to remove remaining multi-jet background. Likelihood ratio is calculated using the following variables:

- $p_{\mathrm{T}}^{\text{di-jet}}$: vector sum of 2 jet (leading jet and second leading jet) transverse momenta
- $p_{\mathrm{T}}^{\text{di-jet}}/(p_{\mathrm{T}}^{jet_1} + p_{\mathrm{T}}^{jet_2})$: ratio between vector sum and scalar sum of leading 2 jet momenta
- $\Delta\phi(E_{\mathrm{T}}^{\mathrm{miss}}, \text{di-jet})$: azimuthal angle between $E_{\mathrm{T}}^{\mathrm{miss}}$ and vector sum of 2 jets
- $\Delta\phi(\mathrm{jet}_1, \mathrm{jet}_2)$: azimuthal angle between leading jet and second leading jet
- cos(helicity): cosine of helicity angle in the di-jet rest frame

The modelling of likelihood ratio distribution is confirmed using multi-jet control region ($\Delta\phi(E_{\mathrm{T}}^{\mathrm{miss}}, p_{\mathrm{T}}^{\mathrm{miss}}) > \pi/2$). Likelihood cut threshold is also optimised using the same multi-jet control region. Remaining events are imposed likelihood ratio $LH > 0.5$.

6.3.2 One lepton Channel

For high p_{T}^{V}category, large $E_{\mathrm{T}}^{\mathrm{miss}}$ is required to suppress multi-jet background. The threshold is optimised depending on p_{T}^{V}, Requirements are $E_{\mathrm{T}}^{\mathrm{miss}} > 20$ GeV for $p_{\mathrm{T}}^{V} > 120$ GeV and $E_{\mathrm{T}}^{\mathrm{miss}} > 50$ GeV for $E_{\mathrm{T}}^{\mathrm{miss}} > 200$ GeV. For low p_{T}^{V}category, $H_T > 180$ GeV is required, where H_T is defined as the scalar sum of momenta of all visible and invisible objects, $H_T = E_{\mathrm{T}}^{\mathrm{miss}} + p_T^{lep} + p_T^{1st\,jet} + p_T^{2nd\,jet}$. The transverse mass, $m_{\mathrm{T}}^{W} = \sqrt{2p_T^l E_{\mathrm{T}}^{\mathrm{miss}}(1 - cos\Delta\phi(l, E_{\mathrm{T}}^{\mathrm{miss}}))}$, requirement of $m_{\mathrm{T}}^{W} < 120$ GeV is required to suppresses $t\bar{t}$ background. For low p_{T}^{V} category, only muon sub-channel is analysed due to that multi-jet modelling in electron sub-channel is difficult.

6.3.3 Two-lepton channel

Two-lepton channel is the most clean channel in this analysis. In Z boson events (ZH(llbb), Z+Jets, ZZ(llqq)) a sharp Z mass peak with Breit-Wigner shape is in the invariant mass distribution of two leptons (m_{ll}) is distinctive to supress the background. A Z mass window cut $83 < m_{ll} < 99$ GeV is applied to remove non Z background ($t\bar{t}$, single top and multi-jets). $E_{\mathrm{T}}^{\mathrm{miss}} < 60$ GeV is also required to remove $t\bar{t}$ background.

6.4 Event selection for multivariate (MVA) analysis

Event selection is re-optimised for MVA analysis. Such that MVA technique gives us better signal to background separation compared to the cut-based analysis. Basic strategy is that the event level selection is loosen to maximise the acceptance and increased backgrounds are separated using MVA. Multi-Jet rejection cuts are kept the same since multi-jet component has a larger uncertainty compared to the other background processes. Several selections are removed or modified to loosen the threshold.

6.4.1 Zero-lepton channel

Zero lepton MVA selection is exactly same as the cut-based selection. In low p_{T}^{V} (0-120 GeV) region in zero lepton channel is not used in the MVA analysis. The cut-based $100 < p_{\mathrm{T}}^{V} < 120$ GeV result is added into MVA high p_{T}^{V}(120-) result.

6.4.2 One-lepton channel

The m_{T}^{W} cut is removed but m_{T}^{W} is used as an input variable in MVA. $E_{\mathrm{T}}^{\mathrm{miss}}$ threshold for events with $p_{\mathrm{T}}^{V} >$ 200 GeV is lowered from 50 GeV to 20 GeV.

6.4.3 Two-lepton channel

$E_{\mathrm{T}}^{\mathrm{miss}}$ cut is removed but $E_{\mathrm{T}}^{\mathrm{miss}}$ is used as an input variable in MVA. The Z mass cut is modified to cover the wider range 71-121 GeV.

Table 6.1: Event topological and kinematic selections. NU stands for 'Not Used'. $(*)$ In the 0-lepton channel, the lower bin edge of the second p_{T}^{V} interval is set at 100 GeV instead of 90 GeV.

Variable	Di-jet-mass analysis					Multivariate analysis	
	Common selection						
p_{T}^{V} (GeV)	0-90	90$^{(*)}$-120	120-160	160-200	> 200	0-120	> 120
$\Delta R(\mathrm{jet}_1, \mathrm{jet}_2)$	0.7-3.4	0.7-3.0	0.7-2.3	0.7-1.8	< 1.4	> 0.7 (p_{T}^{V}<200 GeV)	
	0-lepton selection						
$p_{\mathrm{T}}^{\mathrm{miss}}$ (GeV)	NU	> 30	> 30			NU	> 30
$\Delta\phi(\boldsymbol{E}_{\mathrm{T}}^{\mathrm{miss}}, \boldsymbol{p}_{\mathrm{T}}^{\mathrm{miss}})$		$< \pi/2$	$< \pi/2$				$< \pi/2$
$\min[\Delta\phi(\boldsymbol{E}_{\mathrm{T}}^{\mathrm{miss}}, \mathrm{jet})]$		–	> 1.5				> 1.5
$\Delta\phi(\boldsymbol{E}_{\mathrm{T}}^{\mathrm{miss}}, \text{di-jet})$		> 2.2	> 2.8				> 2.8
$\sum p_{\mathrm{T}}^{\mathrm{jet}_i}$ (GeV) for $N_{\mathrm{jet}} = 2$ (3)		> 120 (NU)	> 120 (150)				> 120 (150)
$E_{\mathrm{T}}^{\mathrm{miss}}$ (GeV)		> 100	–				–
		See text	–				–
	1-lepton selection						
m_{T}^{W} (GeV)	< 120					–	
H_{T} (GeV)	> 180		–			> 180	–
$E_{\mathrm{T}}^{\mathrm{miss}}$ (GeV)	–		> 20		> 50	–	> 20
	2-lepton selection						
$m_{\ell\ell}$ (GeV)	83-99					71-121	
$E_{\mathrm{T}}^{\mathrm{miss}}$ (GeV)	< 60					–	

Chapter 7

Background modelling

This section describes the modelling of individual backgrounds. Multi-jet contamination is estimated from the data, since the accuracy of the QCD prediction is limited Other EWK backgrounds are estimated using theoretical calculation. Mis-modelling in simulations are corrected using the data. ATLAS Monte Carlo (MC) simulation can describe the data distribution to the great details thanks to the huge effort in the code development and tuning, and to the powerful computing system. To improve the modelling of background estimation, the data distribution is fitted by a binned likelihood method with simulated background and signal distributions while constraining their normalisations and shapes.

7.1 Multi-jet background

7.1.1 Zero-lepton channel

Zero-lepton multi-jet contamination is estimated by so called ABCD method. Multi-jet background in this channel is caused due to mis-measurement of jet momentum (resolution effect etc.). First, four regions are defined splitting a 2D phase space constructed by 2 criteria to obtain a signal-like region and background-like region. The value $\min(\Delta\phi(E_T^{\mathrm{miss}}, jet))$ separates the data set vertically between A or B group and C or D group and $\Delta\phi(E_T^{\mathrm{miss}}, p_T^{\mathrm{miss}})$ variable separates horizontally between A or C group and B or D group. Regions B, C and D are multi-jet control regions. $\min(\Delta\phi(E_T^{\mathrm{miss}}, jet))$ and $\min(\Delta\phi(E_T^{\mathrm{miss}}, jet))$ are uncorrelated to each other. The prediction for multi-jet events in the signal region N_A is given by $N_A = N_B/N_D \times N_C$. The background shape iz the signal region A is assumed to be identical to that in region C. The statistics of the control regions are very limited after b-tag requirement. Therefore the b-tagging requirement is dropped in B, C and D regions, and b-tagging normalisation factors ares applied to the so obtained template distributions. For the low p_T^V region, a likelihood value for multi-jet rejection is used instead of $\min(\Delta\phi(E_T^{\mathrm{miss}}, jet))$.

7.1.2 One-lepton channel

Multi-jet contamination in the one-lepton channel is estimated by a lepton isolation inversion method, where we consider multi-jet background fakeing a lepton. The reason of creating fake leptons is different in the muon channel and in the electron channel. Therefore the multi-jet background is determined separately for the muon channel and the electron channel, while estimation methods for the two channels are exactly same.

- New lepton selection (MJ-CR lepton) is defined to enhance the fraction of fake leptons by taking degraded isolation requirement (isolation inversion).
- Multi-jet control region (MJ-CR) is defined using MJ-CR leptons. The events which have a signal lepton are removed from MJ-CR region.
- Multi-jet template faking the signal signature is obtained for MJ-CR
- Normalisation is obtained by a template fit using $E_{\mathrm{T}}^{\mathrm{miss}}$ distribution in the signal region.

Isolated single-lepton triggered events are used in this study. The isolation requirements for MJ-CR leptons are designed to define exclusive leptons to the MJ-CR leptons. A certain fraction of signal candidates are also included in the MJ-CR events. To avoid overlap issue, the events selected as signal candidates are vetoed before

MJ-CR lepton selection. As mentioned above the track-based isolation fraction $\sum_{\Delta R<0.2} p_T^{\text{track}}/p_T^{\text{lepton}}$ is inverted from <4% to 5-50% for electron channel and 7-50% for muon channel. The calorimeter-based isolation fraction $\sum_{\Delta R<0.2} p_T^{\text{cluster}}/p_T^{\text{lepton}}$ is relaxed to 7%. In the MJ-CR selection, MJ-CR lepton is used instead of signal lepton. Other event level selections are exactly same as event selection for the signal. The statistics in the obtained 2-tag template is still very low. Events with 1-tag are used to increase the statistics, since kinematic and BDT output distributions of 1-tag MJ-CR are similar to those of the 2-tag MJ-CR. B-tag weight of un-tagged jet is emulated from b-tag weight map obtained from actual 2-tag events. Residual small discrepancy between 1-tag and 2-tag is reweighted depending on b-tag weight, and for the electron channel, also depending on ΔR and p_T^W. EWK background contribution in MJ template is subtracted using simulation with improved normalisation. Fitting is performed separately in the 2- and 3-jets, 1- and 2-tag categories namely in all b-tag categories inclusively (Figure 7.1.2).

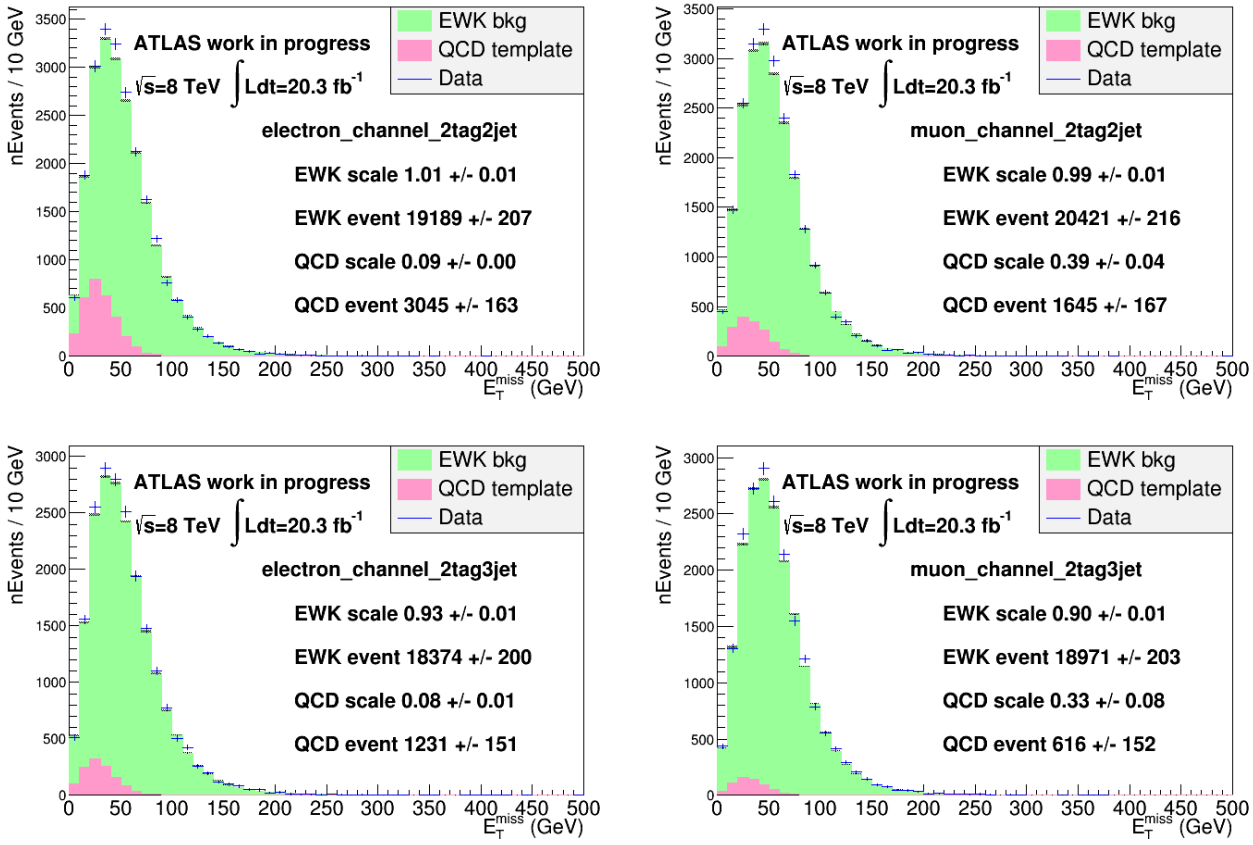

Figure 7.1: Template fit for multi-jet background estimation is performed using $E_{\text{T}}^{\text{miss}}$ distribution. Electron channel 2-b-tag 2 jets (top left), muon channel 2-b-tag 2 jets (top right), electron channel 2-b-tag 3 jets (bottom left) and muon channel 2-b-tag 3 jets (bottom right) fit results are shown. EWK scale corresponds to the overall scale factor for simulated electroweak background in signal region. QCD scale corresponds to the scale factor for obtained QCD template.

7.1.3 Two-lepton channel

For the two-lepton channel, multi-jet background for electron channel is estimated in a similar way to the one-lepton multi-jet estimation. Lepton identification and isolation requirements are loosened to obtain a multi-jet template. The normalisation is estimated by a fit to the di-lepton mass distribution. Multi-jet contamination in muon channel is negligible.

7.2 Corrections and systematic uncertainties in the simulation

This section describes all the systematic uncertainties in the simulation. The summary is listed in Table 7.2.

7.2.1 Signal processes

Signal simulation events are produced with a LO calculation pythia [77] and it is normalised to the NNLO QCD and NLO EWK cross sections. The scale uncertainty on cross section calculation is 1% for the qqWH process and 3% for the ZH process (qq+gg inclusive). Additional 2% for ZH process is due to the ggZH process. It is assumed that the scale uncertainty for qqZH process is same as qqWH process and the scale uncertainty for ggZH process is taken to be consistent with the inclusive scale uncertainty. The scale uncertainty for qqZH process is 1% and the one for ggZH process is 50%. The PDF uncertainty on cross section calculation is similarly estimated as 2.4% for qqWH/ZH and 17% for ggZH. The relative uncertainty on the $H \to bb$ ($m_H = 125$ GeV) branching ratio is 3.3%. The acceptance and p_T^V uncertainties due to the choice of QCD renormalisation scale factor (μ_R) and factorisation scale factor (μ_F) are also estimated using truth level information available in the simulated samples. The signal samples are generated with POWHEG and shower is calculated with PYTHIA8, μ_R and μ_F varied independently by scaling with a factor of 0.5 to 2. The Stewart-Tackmann method [78] is deployed to treat correlations between the 2- and 3-jets regions. The uncertainties are estimated as 3.0%, 3.4% and 1.5% for qqWH, qqZH and ggZH, respectively, for 2- and 3-jets inclusive dataset. The relative uncertainty for 3-jets exclusive dataset are 4.2%, 3.6% and 3.3%. The p_T^V distributions uncertainties are derived. The PDF uncertainty on the acceptance is estimated similarly. The signal samples are generated using MSTW2008NLO68CL [79] and NNPDF23_NLO_AS_0120 [80] pdf sets, while the nominal sample is CT10NLO [81]. The cross section is calculated to NLO for electroweak interactions but the result shows a strong dependence on p_T^V. Therefore, p_T^V dependent relative NLO EWK correction is applied to improve the p_T^V modelling in the qqVH simulation. A differential NLO EWK cross section is calculated using a HAWK MC program [82]. The NNLO QCD contribution is expresses as Δ^2_{NLO}. The uncertainty due to this signal p_T^V correction is assigned to be larger one of 2% or Δ^2_{NLO}. The parton shower uncertainty is estimated using the signal sample where Herwig is used for the parton shower.

7.2.2 Z+jets backgrounds

The 0=b-tag Z($\to$ll)+jets sample is a good control region for Z+jets background. It has a huge statistics and pure Z+jets sample is obtained using the di-jet mass analysis cut. In the 0-b-tag Z+jets control region, the mismodelling is examined in $\Delta\phi(\text{jet}_1,\text{jet}_2)$ distribution. This disagreement is not seen in 2-b-tag region with a Higgs mass window veto ($100 < m_{bb} < 150$ GeV). The mismodelling is significantly larger in the low p_T region. The $\Delta\phi(\text{jet}_1,\text{jet}_2)$ correction is applied to the Z+light jet background in the low p_T and in the high p_T separately. One half of the difference is applied as a correction to Z+light jets background. For the Z+cl/hf (hf=cc, bl, bc and bb) jets, full of the correction is assigned as a systematic uncertainty instead of correction. After the $\Delta\phi(\text{jet}_1,\text{jet}_2)$ correction, simulation-data agreement of p_T^Z distributions is checked. There remains obviously a mismodelling in p_T^Z distribution and it increases as more b-tags are required. The p_T^Z correction is applied to only for the Z+cl/hf jets backgrounds. The correction is derived from 2-b-tag region and half the correction is applied to Z+light jets and Z+cl/hf jets backgrounds. Even in a multivariate technique based analysis, m_{bb} is the most important variable in the H$\to$bb analysis. Finally, m_{bb} distribution is checked and disagreement between data and simulation is assigned as a systematic uncertainty. m_{bb}, p_T^Z and $\Delta\phi(\text{jet}_1,\text{jet}_2)$ distributions are cross checked using different generator, ALPGEN [83]. Normalisation factor to the Z+light jet background is obtained by the data-MC comparison in 0-b-tag region. Also Z+3jet to Z+2jet cross section ratio for Z+light jet background is obtained. The uncertainties for normalisation and 3to2 ratio are 5%. The normalisations of Z+cl and Z+hf backgrounds are determined in a global likelihood fit. Uncertainties for Z+cl and Z+hf normalisation are estimated using simulation data generated with ALPGEN.

7.2.3 W+jets backgrounds

The corrections and uncertainties for W+jets background are estimated using similar method employed for the Z+jets background estimation. But the 0- and 1 b-tag regions are contaminated by multi-jet background and the

Figure 7.2: Summary of the systematic uncertainties.

Signal	
Cross section (scale)	1% ($q\bar{q}$), 50% (gg)
Cross section (PDF)	2.4% ($q\bar{q}$), 17% (gg)
Branching ratio	3.3 %
Acceptance (scale)	1.5%–3.3%
3-jet acceptance (scale)	3.3%–4.2%
p_{T}V shape (scale)	S
Acceptance (PDF)	2%–5%
p_{T}V shape (NLO EW correction)	S
Acceptance (parton shower)	8%–13%
Z+jets	
Zl normalisation, 3/2-jet ratio	5%
Zcl 3/2-jet ratio	26%
Z+hf 3/2-jet ratio	20%
Z+hf/Zbb ratio	12%
$\Delta\phi(\mathrm{jet}_1,\mathrm{jet}_2)$, p_{T}V, m_{bb}	S
W+jets	
Wl normalisation, 3/2-jet ratio	10%
Wcl, W+hf 3/2-jet ratio	10%
Wbl/Wbb ratio	35%
Wbc/Wbb, Wcc/Wbb ratio	12%
$\Delta\phi(\mathrm{jet}_1,\mathrm{jet}_2)$, p_{T}V, m_{bb}	S
$t\bar{t}$	
3/2-jet ratio	20%
High/low-p_{T}V ratio	7.5%
Top-quark p_{T}, m_{bb}, $E_{\mathrm{T}}^{\mathrm{miss}}$	S
Single top	
Cross section	4% (s-,t-channel), 7% (Wt)
Acceptance (generator)	3%–52%
m_{bb}, $p_{\mathrm{T}}^{b_2}$	S
Diboson	
Cross section and acceptance (scale)	3%–29%
Cross section and acceptance (PDF)	2%–4%
m_{bb}	S
Multijet	
0-, 2-lepton channels normalisation	100%
1-lepton channel normalisation	2%–60%
Template variations, reweighting	S

contribution of $t\bar{t}$ background in 2 b-tag region is comparable to the W+jets background. In the 0-b-tag W+jets control region, the mismodelling is examined in $\Delta\phi(\text{jet}_1, \text{jet}_2)$ distribution (See figure 7.3). As mentioned, the modelling of multi-jet background contribution is remarkably difficult, but the general trend is similar to the Z+jets. The mismodelling is determined separately for the electron channel and muon channel which has less multi-jet background. The only difference compared to the Z+jets case is that the mismodelling in the 1-tag distribution is larger than the Z+jets with dominant W+jets flavor component in 1-tag being W+cl. Therefore, $\Delta\phi(\text{jet}_1, \text{jet}_2)$ correction is applied to the W+light jets background and the W+cl jets background. As same as in the Z+jets case, half the correction for the W+light/cl and full correction for the W+hf background are assigned as a systematic uncertainty. In the W+jets background, p_T^Z correction is not applied, since there is no significant mismodelling. The uncertainty for the p_T^Z and m_{bb} distribution is estimated by generator comparison described below. W+light normalisation and 3to2 jet ratio for W+ll and W+cl are taken from the profile likelihood fit including the 0-b-tag region. Their uncertainties are 10%. The normalisations for W+cl and W+hf are determined in the global fit. The uncertainties for W+hf are estimated using the simulations, since there is no good control region for W+hf backgrounds. The nominal generator, Sherpa, is compared to the various generators, POWHEG+PYTHIA8 [77, 84–86], aMC@NLO+HERWIG++ [87, 88] and ALPGEN+HERWIG [83, 88]. The 3to2 jet ratio for W+bb and relative heavy flavour composition (W+bl to W+bb, W+bc to W+bb and W+cc to W+bb) are also estimated using simulations. Same as in the signal simulation, the uncertainties due to the choice of QCD factorisation scale, renormalisation scale and PDFs (CT10, MSTW2008NLO and NNPDF2.3 examined) are estimated using aMC@NLO+HERWIG++ simulations.

7.2.4 $t\bar{t}$ backgrounds

The simulated top quark $p_T(p_T^{top})$ distribution is too hard compared to the data, which is already reported by ATLAS $t\bar{t}$ analysis of 7 TeV data. The generator level top quark p_T is reweighted using the unfolded 7 TeV distribution (e.g. detector effects are corrected) and half the correction is assigned as a systematic uncertainty. The variables which are used as input variables to define the analysis regions, and selections are checked after p_T reweighting. The nominal generator, Powheg+Pythia, is compared to the various generators same as in the W+bb case. The $t\bar{t}$ background is a dominant background in the one-lepton region, all the comparison is performed with the one-lepton analysis selections applied. The list of generators used to estimate the uncertainty is summarised as following:

- POWHEG+PYTHIA with P2012: nominal simulation
- ALPGEN+PYTHIA with P2012: higher order contribution (ALPGEN is a LO generator, POWHEG is an NLO generator)
- POWHEG+HERWIG with CT10: parton showering and hadronisation model
- AcerMC [89] with more or less Parton Shower (PS) CTEQ6: increasing/decreasing initial state radiation and final state radiation (ISR/FSR). (morePS-lessPS)/2 is considered as a uncertainty due to the PS modeling
- aMC@NLO with CT10: matrix element calculation and matching scheme
- POWHEG+PYTHIA with HeraPDFs: choice of PDF (HERA PDF well describe the ATLAS data, resulting in a better p_T^{top} modelling)

POWHEG-ALPGEN comparison gives a largest difference which is assigned as systematic uncertainty. Other effects are also covered by this comparison. Considered systematic uncertainties are high/low p_T^V ratio, 3to2 jet ratio. Shape uncertainty is assigned to p_T^V, m_{bb}, $p_T^{leading\,jet}$ and E_T^{miss} distributions.

7.2.5 Single top quark backgrounds

Three channels of single top production processes (s-channel, t-channel and Wt-channel) are considered in this analysis. The systematic uncertainty for these processes are estimated using the various types of simulations similar to the $t\bar{t}$ systematic estimation.

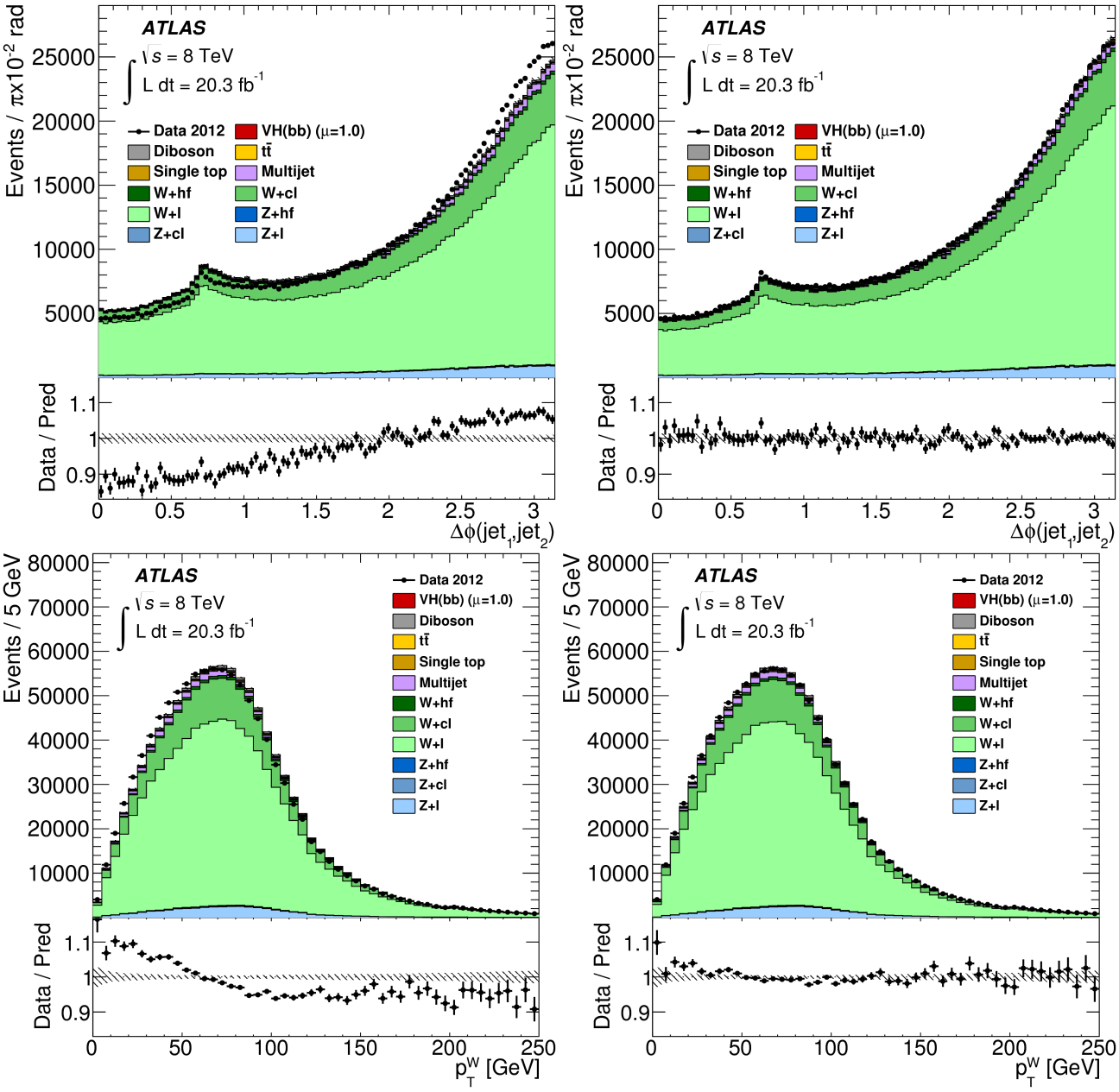

Figure 7.3: $\Delta\phi(\text{jet}_1,\text{jet}_2)$ and p_T^V distributions before (left) and after (right) $\Delta\phi(\text{jet}_1,\text{jet}_2)$ correction. After the $\Delta\phi(\text{jet}_1,\text{jet}_2)$ correction, p_T^V modeling is clearly improved.

s-channel

Nominal generator is an NLO generator, Powheg+Pythia. Higher order effects are estimated by comparison using AcerMC with ISR/FSR effects estimated using more-or-less PS in addition. Cross check is done by MC@NLO (hadronization and showering effects).

t-channel

Nominal generator is AcerMC with Pythia, which is compared to aMC@NLO. Higher effects, hadronisation and showering models are considered. ISR/FSR effects estimated using AcerMC with more or less PS are negligible in this channel.

Wt-channel

Nominal generator is PowhegPythia. Higher order effects are evaluated by AcerMC and hadronisation and showering effects are estimated by PowhegHerwig and MC@NLO. NLO single top Wt process shares the same final states with the LO $t\bar{t}$ process. There are interference effects between these two processes. There are two methods to consider these effects: one is Diagram Removal used in AcerMC and another one is Diagram Subtraction used in Powheg+Pythia. ISR/FSR effects estimated using AcerMC with more or less PS are negligible in this channel.

7.2.6 Diboson backgrounds

The nominal MC is Powheg+Pythia. The contribution of gluon-gluon initial process which is not included in the Powheg cross section calculation is added using the MCFM [90]. The perturbative uncertainties on the fixed-order NLO cross section computation is also estimated using MCFM. MCFM is an NLO generator, hence the NNLO cross sections for 2-jet (VV+0jet) and $\leq$3-jet (VV+1jet) are exclusively calculated and the uncertainties for 2jet bin and 3-jet bin are exclusively estimated using Stewart-Tackmann method to correlate the two processes. The PDF and α_s uncertainties are calculated comparing between MSTW2008 PDF set and nominal (CT10) PDF set using MCFM. The uncertainties on hadronisation and showering models are estimated comparing between Herwig and the nominal generator, Powheg+Pythia.

Chapter 8

Multivariate analysis (MVA)

8.1 Boosted Decision Tree (BDT)

Generally final results such as exclusion limit, significance and signal strength are calculated from the distribution which has a best signal to background separation. For instance, di-jet mass (m_{bb}) distribution is a best variable to obtain the results in this analysis. In a cut-based analysis, selections are applied to maximise the sensitivity on final distribution (m_{bb}). However, other variables like angle between the two b-jets ($\Delta R(b,b)$) have also a good discriminate power and there may exist a certain signal contribution also in the rejected events. If there is a large number of data and simulation events, multi-dimensional likelihood fit is a simple solution. In the real case, the statistical uncertainty does not allow us to apply this method. The MVA technique is a solution for this problem. The multivariate classifier makes a one-dimensional final distribution which has an excellent discrimination power from multi-dimensional distribution constructing using as input variables for training (likelihood function is a simple example). The biggest advantage of this method is that the MVA analysis is able to take the correlation among the variables. Even if one variable does not have any discrimination power it can still contribute to the final distribution. The Toolkit for Multivariate Analysis (TMVA) provides machine learning environment for various multivariate classifiers [91]. The projective likelihoods, artificial neuralnets (ANNs), boosted decision trees (BDTs) and Support vector machines (SVMs) are also available. These multivariate classifiers are automatically trainged through "machine learning". In this analysis, BDT and ANN give a better signal to background separation compared to the likelihood and SVM. Additionally, the training time for BDT classifier is much faster than the ANN training with similar performance. The BDT is used in this analysis.

The decision tree (DT) is a similar method to the cut-based analysis. Define a set of two-choice multiple questions called "node" (Figure 8.1). Each question separates the given events to signal-like events and background-like events. The questions configure a "tree" with several depths. First question separates the events and second question separates further the splitted events by the first question. The latter question depends on the previous question. Then the last node makes the final decision. Single tree decision may not be so accurate and weak. Boosting can build a powerful classifier combining many decision trees. That is the main strategy of the BDT. There are several boosting methods: AdaBoost (adaptive boost) is used in this analysis. The AdaBoost can handle negatively weighted events produced by the generator (MC@NLO and AcerMC). In the AdaBoost, each tree is weighted by *boost weight* α.

$$\alpha = \frac{1-err}{err} \tag{8.1}$$

where err is a misclassification rate. Each tree returns $h(\mathbf{x}) = +1$ or -1 for signal or backgrounds. The boosted event classification $y_{Boost}(\mathbf{x})$ is given by

$$y_{\text{Boost}}(\mathbf{x}) = \frac{1}{N_{\text{collection}}} \sum_{i}^{N_{\text{collection}}} ln(\alpha_i^{\beta}) h_i(\mathbf{x}). \tag{8.2}$$

Small y value indicates a background-like and large y value means a signal-like. The degrees of freedom in BDT classifier like number of trees, number of depths in each tree and number of input variables are optimised depending on the statistic of training sample (half the statistics each in background and signal simulations).

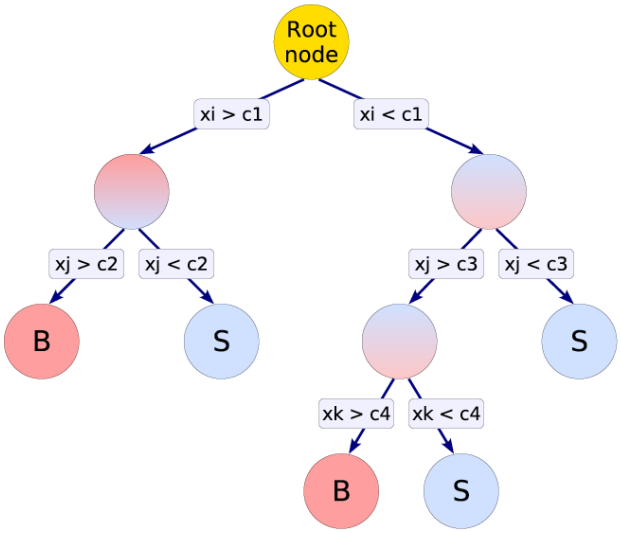

Figure 8.1: Schematic view of a decision tree. Each tree categorises an event into signal or background determined on the nodes. [91]

Table 8.1: Parameters for BDT training

Boosting type	AdaBoost
Number of trees	200
Max depth of trees	4
Min number of events in a node	100
β in AdaBoost	0.15

The parameters for the BDT training is in Table 8.1. General concern on the multivariate analysis with machine training is a "over training". When the classifier is trained, the classifier may have a bias on typical data sample. That is called "over training". In order to confirm that the trained BDT does not have a bias, all simulation dataset is split into two datasets, one for training and another for testing. The BDT outputs for training and testing samples are compared using χ^2 test and Kolmogorov-Smirnov test. Usually this method discards the training sample and only testing sample is used in the analysis. In order to avoid the event loss, another BDT (BDT') is trained using a test sample with exactly same configuration and the result is applied to the training sample. The data is divided into two groups and each data sample is analysed by one of prepared BDTs (BDT and BDT').

8.2 Input variables

The input variables for BDT are selected considering the characteristic of signal and backgrounds. Many of them are imported from the cut-based analysis. For the 3-jet category, $p_T^{jet_3}$ and m_{bbj} are added with the aim of $t\bar{t}$ rejection. The m_{bb} has a biggest contribution to the BDT in all the channels. The $\Delta R(b_1, b_2)$ is also an important variable in all the channels. The truth tagging method is used to maximise the training statistics. The input variables are listed in Table 8.2. The distributions of input variables for the data and MC are compared in Figs**??**. For the MC, contributions of various background sources are shown separately with a contribution of Higgs of 120 GeV/c^2 (the vertical scale is expanded by 50) added. The ratio of the data and MC distribution is also plotted for each variable. The agreement of data and MC distributions of each input variables is confirmed.

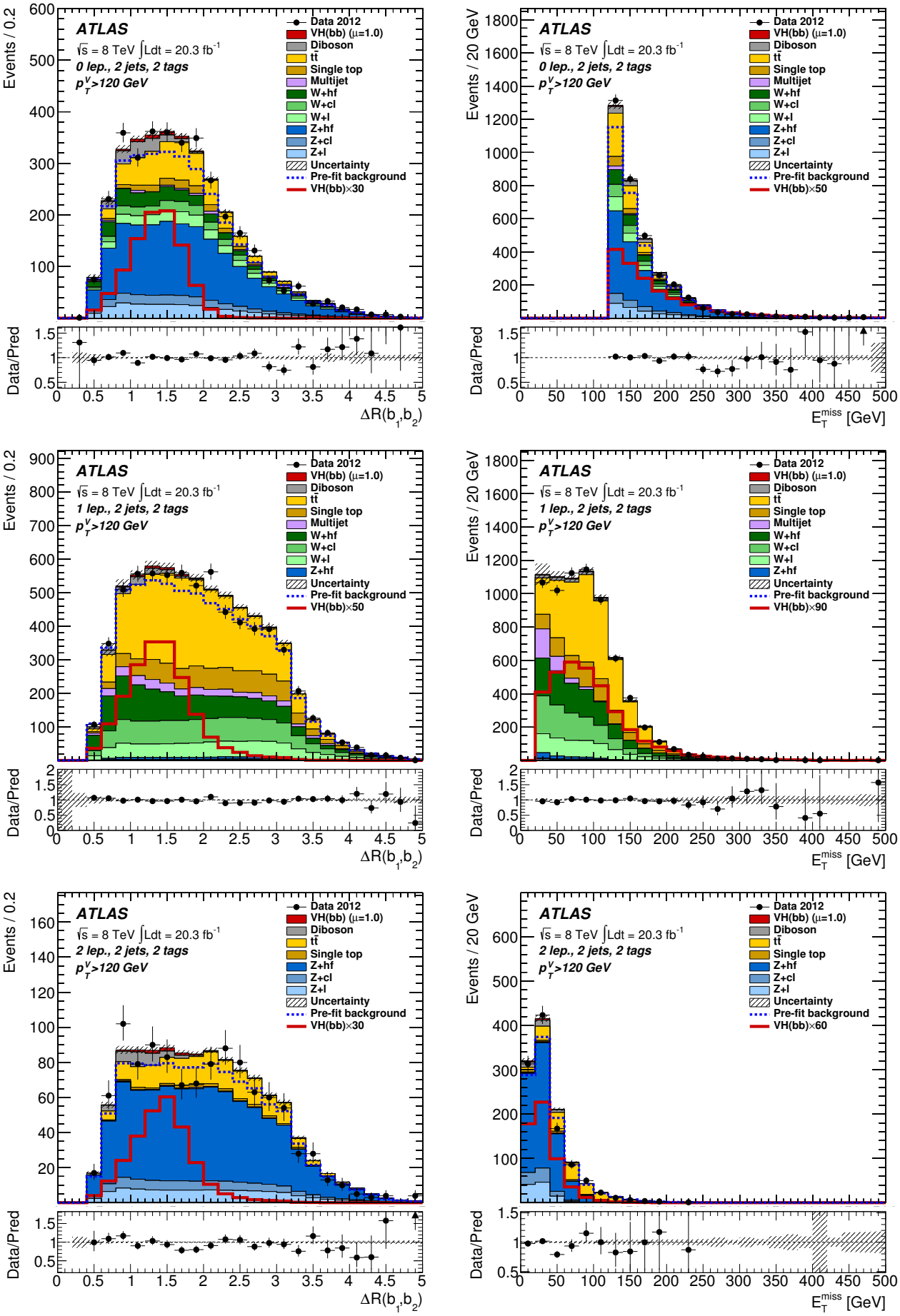

Figure 8.2: ΔR and $E_{\mathrm{T}}^{\mathrm{miss}}$ distributions in 0-, 1- and 2-lepton channel are shown.

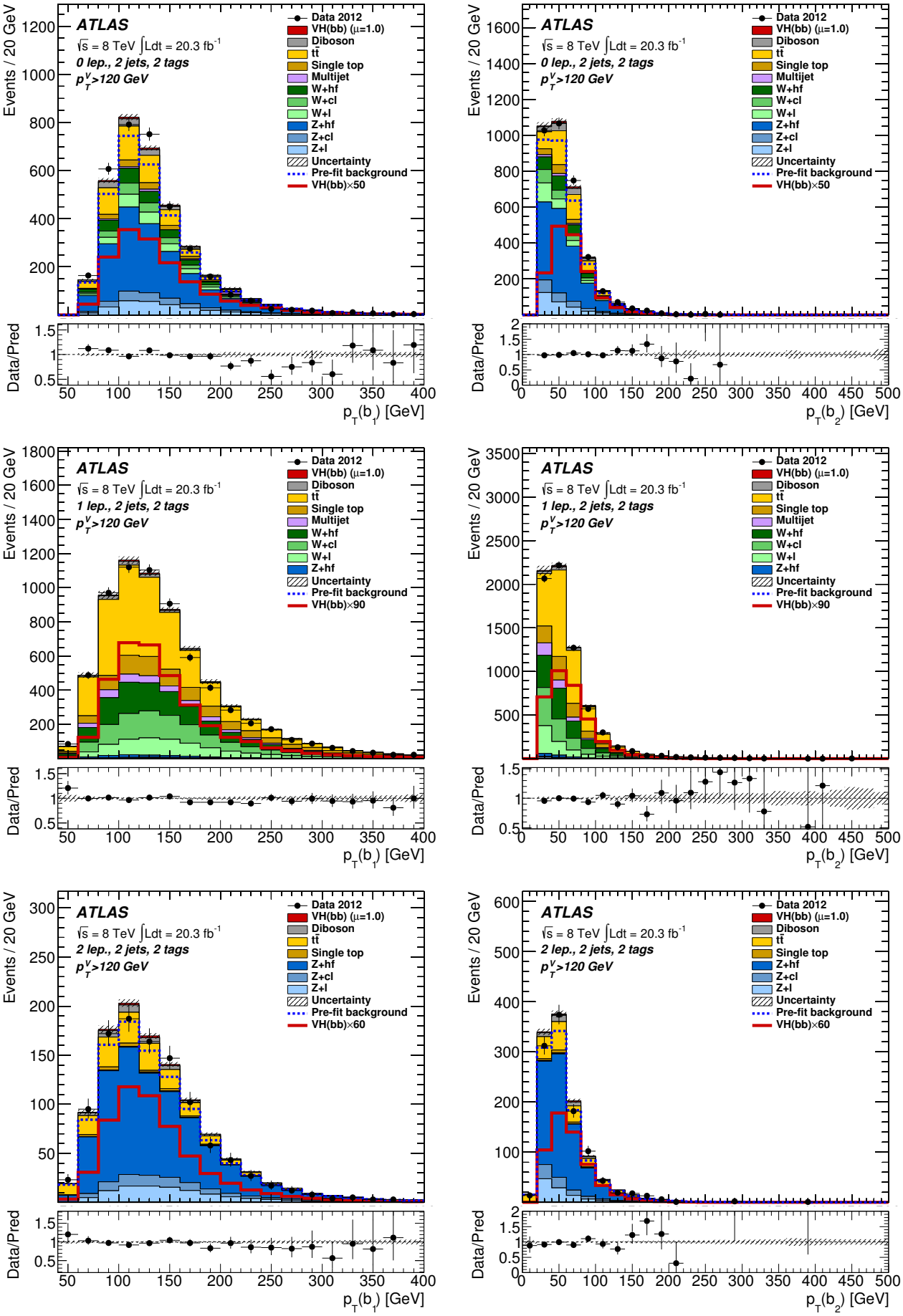

Figure 8.3: p_T^{b1} and p_T^{b2} distributions in 0-, 1- and 2-lepton channel are shown.

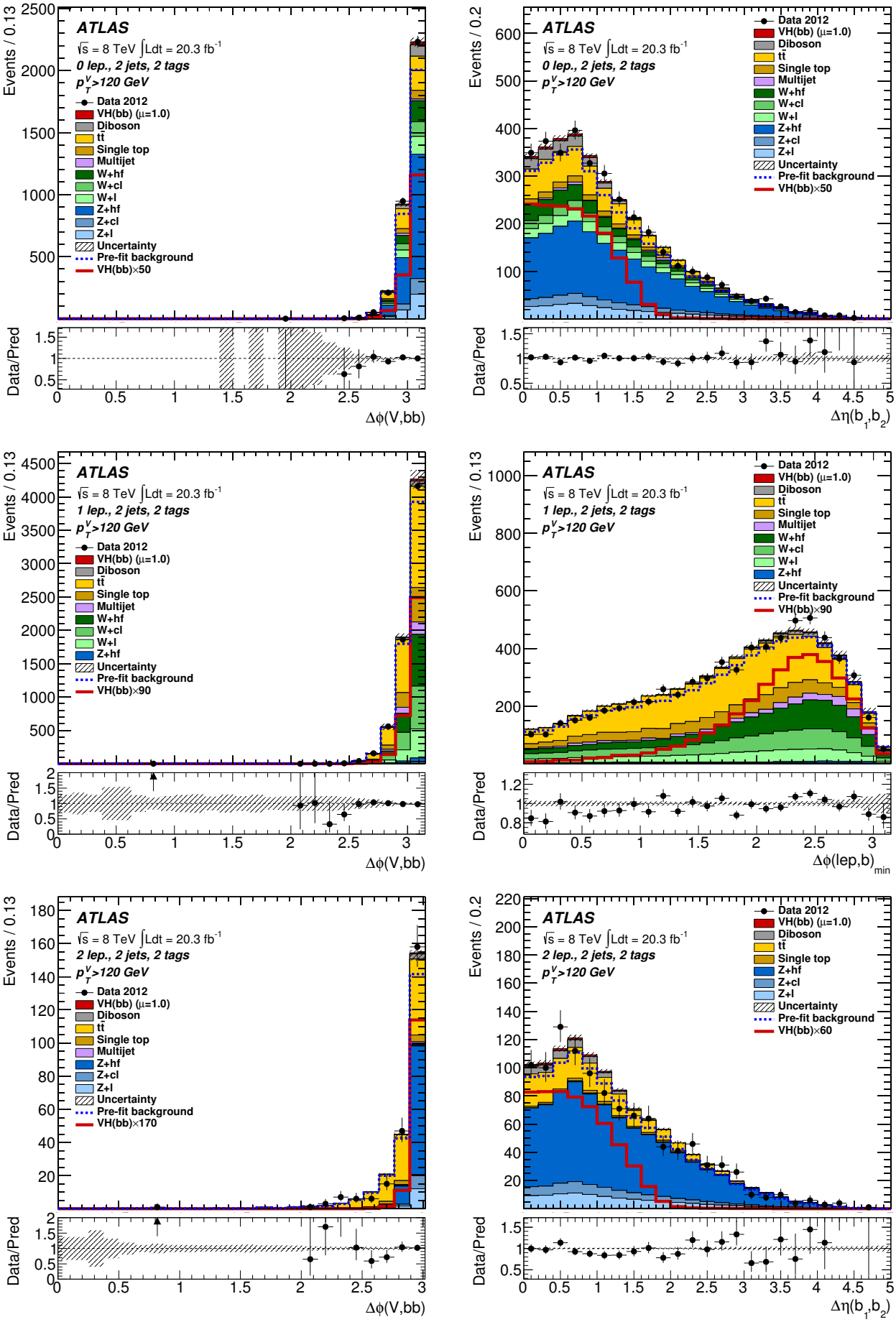

Figure 8.4: $\Delta\phi$(V, bb), $\Delta\eta$(b, b) and min$\Delta\phi$(lep, b) distributions in 0-, 1- and 2-lepton channel are shown.

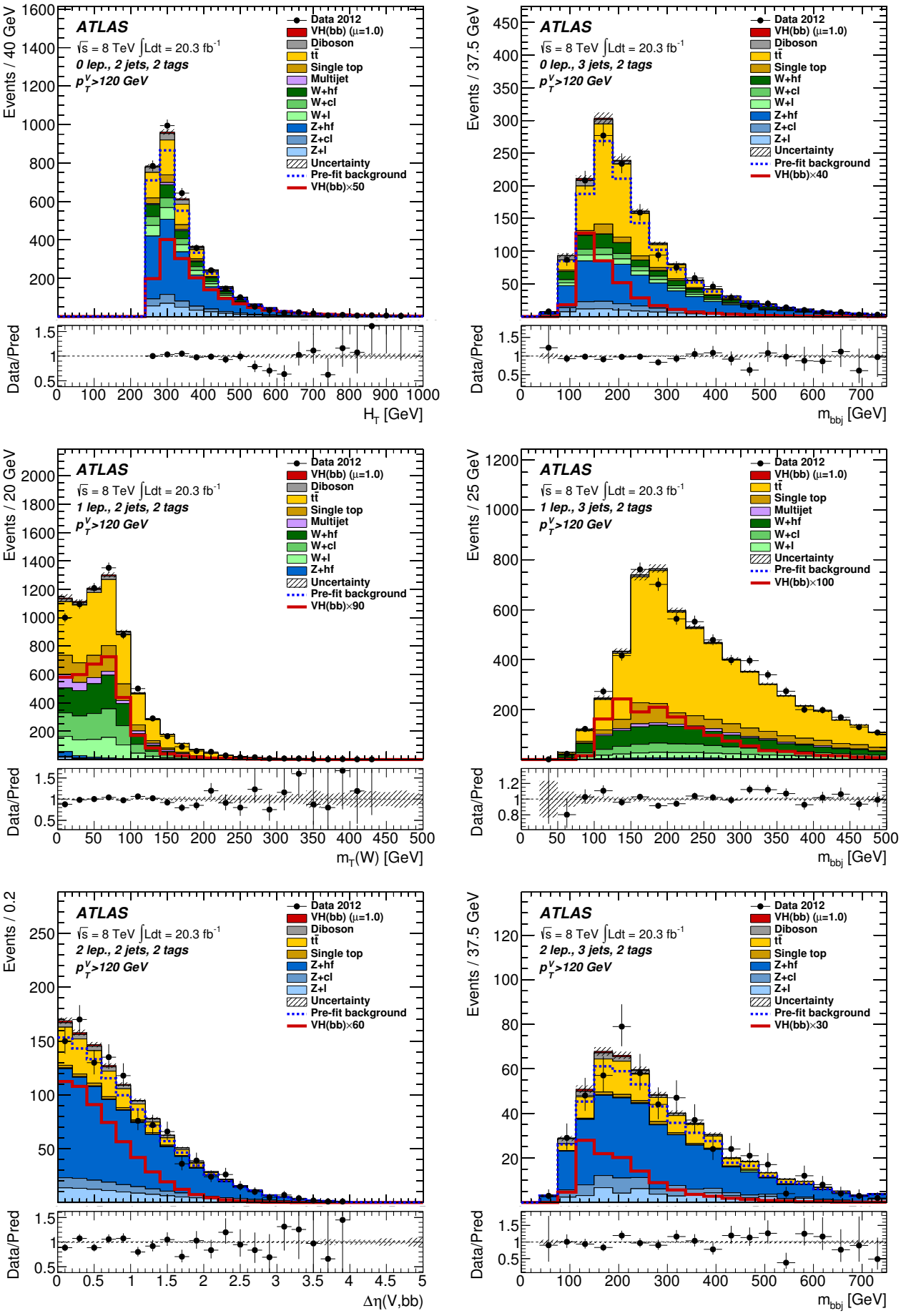

Figure 8.5: HT, m_T^W, $\delta\eta$ (V, bb) and m_{bbj} distributions in 0-, 1- and 2-lepton channel are shown.

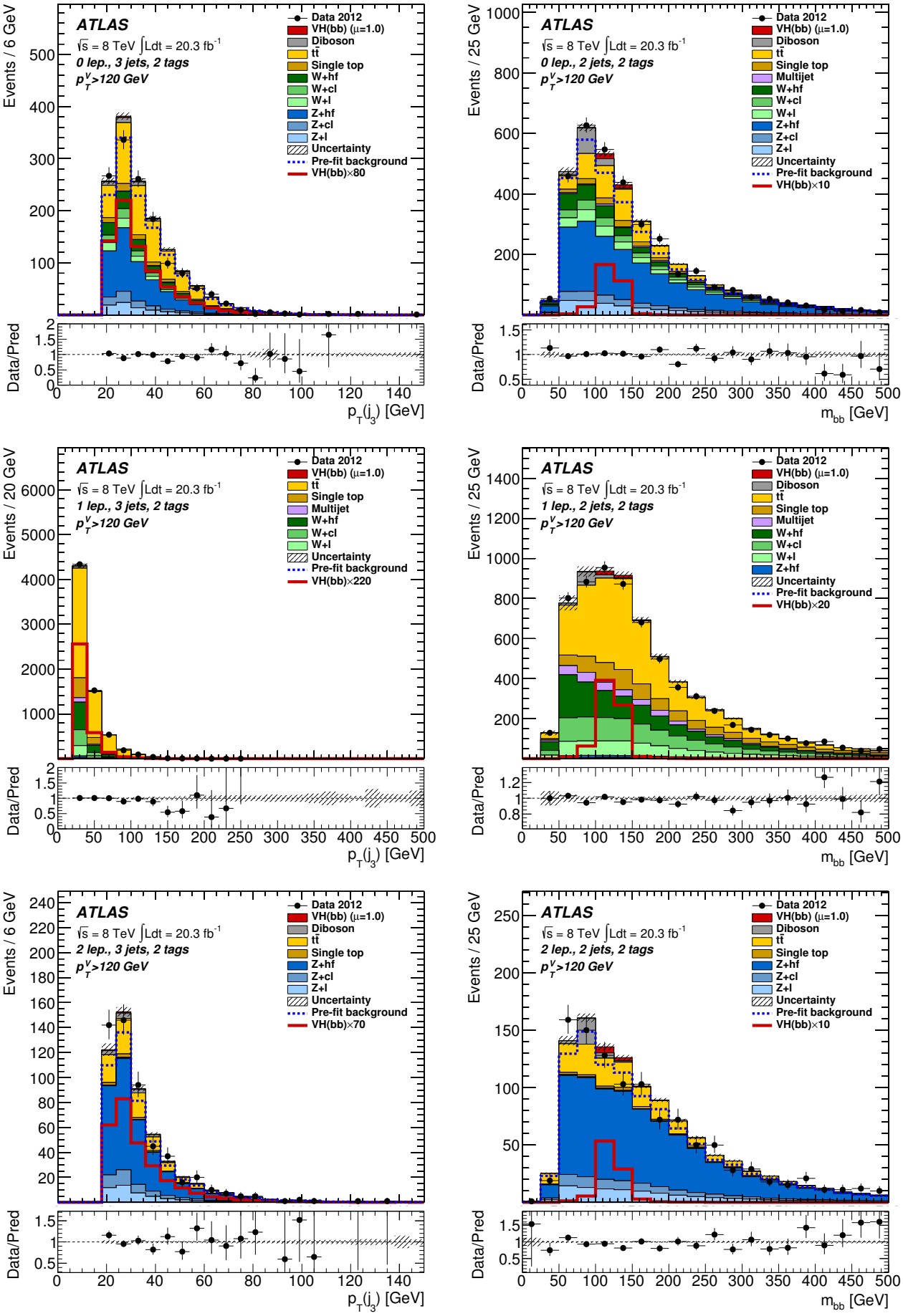

Figure 8.6: p_T^{j3} and m_{bb} distributions in 0-, 1- and 2-lepton channel are shown.

Variable	0-Lepton	1-Lepton	2-Lepton
p_{T}^{V}		×	×
$E_{\mathrm{T}}^{\mathrm{miss}}$	×	×	×
$p_{\mathrm{T}}^{\text{b-}jet_1}$	×	×	×
$p_{\mathrm{T}}^{\text{b-}jet_2}$	×	×	×
$m_{di\text{-}b\text{-}jet}$	×	×	×
$\Delta R(\mathrm{b}_1, \mathrm{b}_2)$	×	×	×
$\lvert\Delta\eta(\mathrm{b}_1, \mathrm{b}_2)\rvert$	×		×
$\Delta\phi(V, \text{di-b-jet})$	×	×	×
$\lvert\Delta\eta(V, \text{di-b-jet})\rvert$			×
H_{T}	×		
$\min[\Delta\phi(\ell, \mathrm{b})]$		×	
m_{T}^{W}		×	
$m_{\ell\ell}$			×
$MV1c(\mathrm{b}_1)$	×	×	×
$MV1c(\mathrm{b}_2)$	×	×	×
	Only in 3-jet events		
$p_{\mathrm{T}}^{\mathrm{jet}_3}$	×	×	×
m_{bbj}	×	×	×

Table 8.2: Variables used in the multivariate analysis for the 0-, 1- and 2-lepton channels.

Chapter 9

Statistical analysis

9.1 Basic technique of statistical analysis

The exclusion limit, significance and signal strength are extracted from m_{bb} and MVA distributions separately using a statistical analysis procedure; a binned maximum likelihood fit. All the histograms in each channel and each region are simultaneously treated in the "global fit". This section describes the basic technique of the "global fit".
The expected number of events in i-th bin is written as

$$E[n_i] = \mu s_i + b_i \tag{9.1}$$

where s_i is the Standard Model expectation for $H \to bb$ (σ_{SM}) in i-th bin and b_i represents the background contribution. The μ is the signal strength meaning that with $\mu = 1$ number of expected signals is equal to the SM prediction. The s_i and b_i are written as

$$s_i = s_{tot} \int_{ith\ bin} f_s(\boldsymbol{\theta}_s) dx, \quad b_i = b_{tot} \int_{i\text{-}th\ bin} f_b(\boldsymbol{\theta}_b) dx \tag{9.2}$$

where s_{tot} and b_{tot} are the total numbers of signal and backgrounds, $f_s()$ and $f_b()$ are the probability density functions (pdfs), and $\boldsymbol{\theta}_s$ and $\boldsymbol{\theta}_b$ are the parameters which describe the shape of pdfs. The dependence of the signal and background predictions on the systematic uncertainties is described by a set of nuisance parameters (NP), $\boldsymbol{\theta}$. Additionally, the data in the control region which does not contain a signal gives a good constraint to the nuisance parameters.

$$E[m_i] = u_i(\boldsymbol{\theta}) \tag{9.3}$$

where u_i are estimated values depending on parameters $\boldsymbol{\theta}$. This information can constrain the parameters corresponding to the background normalisation and/or the background shape. The likelihood function is expressed as a product of Poisson distributions for all bins

$$\mathscr{L}(\mu, \theta) = \prod_{j=1}^{N} \frac{(\mu s_j + b_j)^{n_j}}{n_j!} e^{-(\mu s_j + b_j)} \prod_{k=1}^{M} \frac{u^{m_k}}{m_k!} e^{-u_k} \tag{9.4}$$

where N is the number of bins in signal region and M is a number of bins in the auxiliary measurements. Nuisance parameters are parameterised by Gaussian or log-normal constraint. Log-normal constraints are used for normalisation uncertainties to maintain positive pdfs. The signal strength μ and its error σ_μ are obtained by the fit with maximising this likelihood function. The test statistic q_μ is constructed using the profile likelihood ratio

$$q_\mu = -2\ln\left(\mathscr{L}(\mu, \hat{\hat{\boldsymbol{\theta}}}) / \mathscr{L}(\hat{\mu}, \hat{\boldsymbol{\theta}})\right), \tag{9.5}$$

where $\hat{\mu}$ and $\hat{\boldsymbol{\theta}}$ are the parameters which maximise the likelihood with constraint $0 \leq \hat{\mu} \leq \mu$. and $\hat{\hat{\boldsymbol{\theta}}}$ are the nuisance parameter values that maximise the likelihood for a given μ. The exclusion limit with 95% interval derived with CL_s method is calculated using the test statistics. The compatibility between background-only hypothesis and observed data is calculated from the test statistic without signal ($\mu = 0$), $q_0 = -2\ln\lambda_0$. The probability of the background-only hypothesis (p_0 value) is calculated as

$$p_0 = \int_{q_0, obs}^{\infty} f(q_0, 0) dq_0 \tag{9.6}$$

where q_0, obs is the value of the q_0 observed from the data and $f(q_0, 0)$ denotes the pdf of q_0.

9.2 BDT output transformation

The shape of the BDT output distribution itself is meaningless. The right hand side is signal rich and left hand side acts as a background control region. The constant bin width with default output is not optimal. Since only a few bins on the right hand side have a contribution to the signal sensitivity. Finer bins gives a better sensitivity, on the other hand statistical power is decreased with increasing the number of bins. Thus the best solution to maximise the sensitivity with reasonable number of bins is achievable variable binning width. To make an optimal binning, the histogram is made with very fine binning (number of bins = 1000). The BDT output distribution with fine binning is transformed according to the following procedure. First, the transform function for the cut-based analysis is defined as

$$Z = z_s n_s/N_s + z_b n_b/N_b \tag{9.7}$$

and one for the MVA analysis is defined as

$$Z = \sqrt{z_b n_b/N_b} + \sqrt{z_s llr_s} \tag{9.8}$$

where z_b and z_s are the parameters to optimise the transformation, n_b and n_s are numbers of backgrounds and signals in the interval (new bin), N_b and N_s are total numbers of backgrounds and signals and llr_s is written as

$$llr_s = \Sigma_{i \text{ in interval}} s_i \times \log(1 + s_i/b_i) \tag{9.9}$$

where s_i and b_i are the numbers of signals and backgrounds in i-th bin. The distribution is re-binned with following steps.

- Define the interval between bins: Starting from right most bin in the histogram and adding left side bins into the interval one by one.
- Calculate Z value in the new bin
- If $Z > 0$ or $\sigma_b < 0.10$, rebin all the bins in the interval into one new bin
- Re-define the right most bin and redo the above three processes until the end

Here σ_b is a relative statistical uncertainty on the background. The optimised value for z_b and z_s are summarised at table 9.1. Figures 9.1 show m_{bb} and MVA output distribution before and after output transformation.

Table 9.1: Optimised values for z_b and z_s for MVA and cut based analysis (for 0-, 1-, 2-lepton regions), shown for 2-jet and 3-jet categories.

Region	2-jet	3-jet
MVA	$z_s = 4.5, z_b = 4.5$	$z_s = 4.5, z_b = 4.5$
cut (zero-lepton)	$z_s = 6, z_b = 2$	$z_s = 4, z_b = 2$
cut (one-lepton)	$z_s = 6, z_b = 2$	$z_s = 4, z_b = 2$
cut (two-lepton)	$z_s = 4, z_b = 4$	$z_s = 2, z_b = 2$

9.3 Definition of normalisation factors

Normalisation scales for W+jets, Z+jets and $t\bar{t}$ backgrounds are determined from the fit. For the W+jets and Z+jets, estimation of the flavour fraction in jets has a direct impact on the final result. This section describes the definition of normalisation factors.

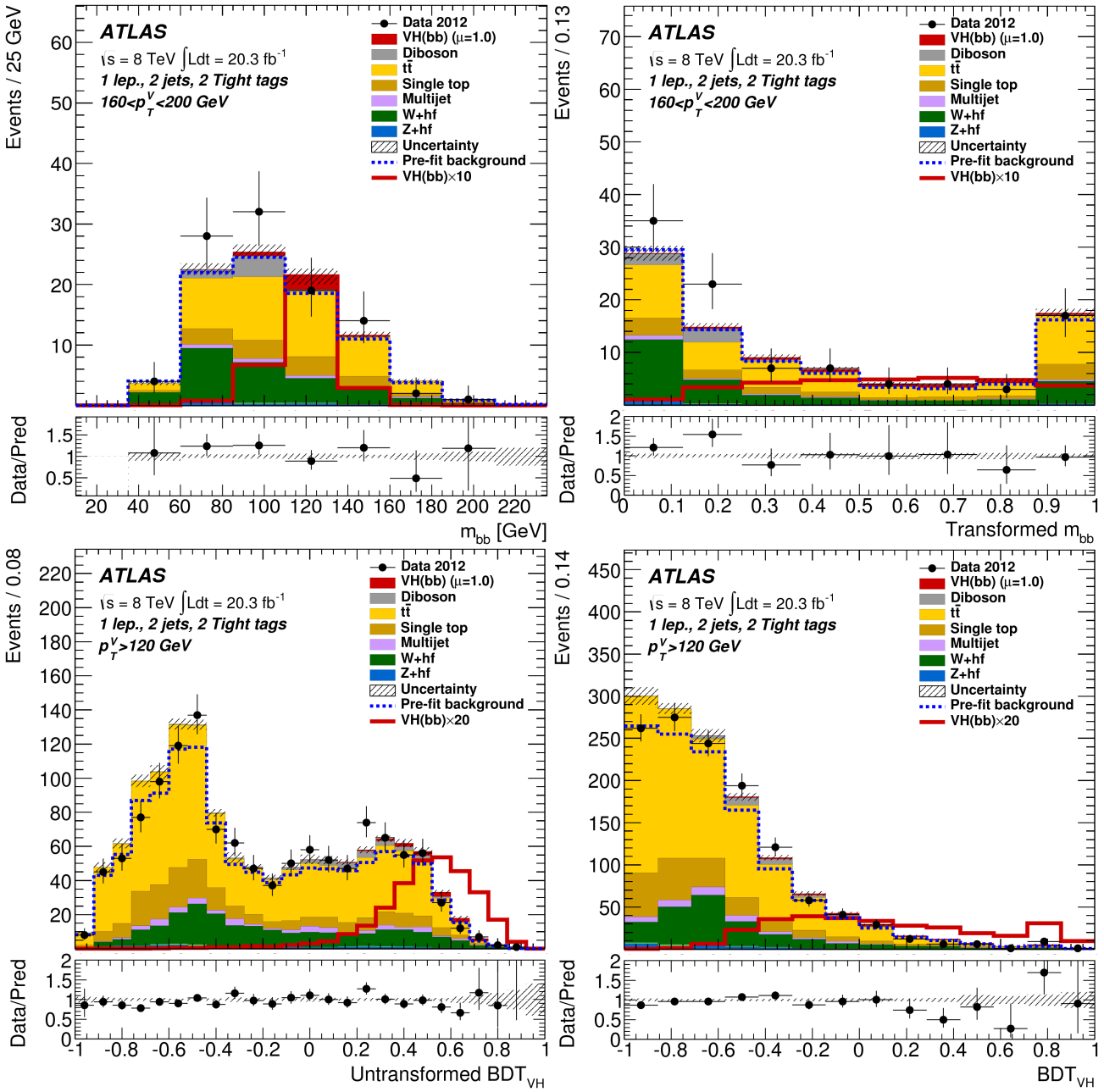

Figure 9.1: Output transformation for di-jet analysis (top) and mva analysis (bottom).

9.3.1 V+Jets

The events in W+jets backgrounds are split into three categories. As we discussed, they are V+light (light flavours = u,d and s), V+cl (charm and light flavour) and V+hf (heavy flavour containing b-jets). The normalisation of V+light is taken from data-MC comparison using the events in the 0-tag control region. The normalisations for V+cl and V+hf are obtained from the fit. The V+hf normalisation is defined as the V+bb normalisation. And V+bc and V+bl are considered using the ratio from V+bc/bl to V+bb estimated using MC. The normalisation factors for 3-jet category is also treated with the ratio of 3-jet and 2-jet. The summary is

$$N_{tot}^{V+jets} = N_{ll} + N_{cl} + N_{hf} \tag{9.10}$$

$$N_{ll} = \eta_{ll} N_{ll}^{2\ jet} + \eta_{ll}\alpha_{3/2} N_{ll}^{3\ jet} \tag{9.11}$$

$$N_{cl} = \alpha_{cl} N_{cl}^{2\ jet} + \alpha_{cl}\alpha_{3/2} N_{cl}^{3\ jet} \tag{9.12}$$

$$N_{hf} = \alpha_{hf} N_{hf}^{2\ jet} + \alpha_{hf}\alpha_{3/2} N_{hf}^{3\ jet} \tag{9.13}$$

$$N_{hf}^{i\ jet} = N_{bb}^{2\ jet} + \eta_{bl/bb} N_{bl}^{2\ jet} + \eta_{bc/bb} N_{bc}^{2\ jet} \tag{9.14}$$

where Ns are the number of events in each flavour, αs are the floating parameters in the fit and ηs are the systematic uncertainties estimated by data-MC comparison or by MC based studies.

9.3.2 $t\bar{t}$

For the $t\bar{t}$ backgrounds, normalisations for the three search channels are separately obtained from the fit, since the contributing decay modes of the $t\bar{t}$ background are different. The dominant $t\bar{t}$ contribution to two-lepton category is $t\bar{t}$ background with di-leptonic decays. On the other hand, the one for one-lepton category is the $t\bar{t}$ background with one-leptonic and one-hadronic decays. For the zero-lepton case, both di-leptonic decays and leptonic/hadronic decays contribute, and the fraction of $t\bar{t}$ decaying into τ lepton is larger than in the other channels. The uncertainty on high p_T^V to low p_T^V ratio and the one on 3-jet to 2-jet ratio are assigned as following

$$N_{tot}^{t\bar{t}} = \alpha_{0lep} N_{0lep} + \alpha_{1lep} N_{1lep} + \alpha_{2lep} N_{2lep} \tag{9.15}$$

$$N_{0lep} = N_{0lep}^{2jet} + \eta_{3/2}^{01lep} N_{0lep}^{3jet} \tag{9.16}$$

$$N_{1lep} = N_{1lep}^{2jet} + \eta_{3/2}^{01lep} N_{1lep}^{3jet} \tag{9.17}$$

$$N_{2lep} = N_{2lep}^{2jet} + \eta_{3/2}^{2lep} N_{2lep}^{3jet} \tag{9.18}$$

$$N_{j\ lep}^{i\ jet} = \left(N_{j\ lep}^{low} + \eta_{high/low} N_{j\ lep}^{high} \right)^{i\ jet} \tag{9.19}$$

The 3-jet to 2-jet ratio for two-lepton channel and one for other channels are separately determined. The reason is similar to the $t\bar{t}$ normalisation factors.

9.4 Definition of signal regions and fit results

For the cut-base analysis, two b-tagged transformed m_{bb} distributions and one b-tagged MV1c b-tagging distributions are used in the cut-based global fit. The m_{bb} distributions are divided into three b-tagging categories, they are LL, MM and TT tag categories. Each b-tagging category has a 5 p_{T}^V bins and two- and three-jet regions. The MV1c distributions give a constraint to V+jets normalisation factors. For the MVA analysis, two b-tagged transformed BDT output distributions and one b-tagged MV1c b-tagging distributions are used in the MVA global fit. The BDT output distributions are divided into three b-tagging categories for one-lepton channel. For zero- and two-lepton channel, LL tag category and MM tag category are combined into one b-tagging category, thus there are two-b-tagging categories in zero- and two-lepton channel. All fit distributions are summarized in Table 9.4. The $t\bar{t}$ normalisation factors for three channels and $V + bb/cl$ normalisation factors are determined by the maximum likelihood fitting. The obtained normalisation factors are summarised in Table 9.4. The $t\bar{t}$ background is normalised separetely in three lepton channels. Huge number of systematic uncertainties are considered in the global fit. Figure 9.2 shows the impact of nuisance parameters on the fitted signal strength.

Table 9.2: List of the distributions used in the maximum likelihood fitting.

		cut-base			MVA		
Channel		0-lepton	1-lepton	2-lepton	0-lepton	1-lepton	2-lepton
	1-tag	MV1c			MV1c		
LL		m_{bb}			BDT		
MM	2-tag	m_{bb}			BDT	BDT	BDT
TT		m_{bb}				BDT	

Table 9.3: The normalisation factors (observed/simulated) obtained by the maximum likelihood fitting.

Process	Scale factor
$t\bar{t}$ 0-lepton	1.36±0.14
$t\bar{t}$ 1-lepton	1.12±0.09
$t\bar{t}$ 2-lepton	0.99±0.04
$W+bb$	0.83±0.15
$W+cl$	1.14±0.10
$Z+bb$	1.09±0.05
$Z+cl$	0.88±0.12

The nuisance parameters are ordered by decreasing order of their impacts. The $\mathrm{W}+\mathrm{b\bar{b}}$, $\mathrm{W}+\mathrm{c\bar{c}}$ m_{jj} shape uncertainty for the $p_{\mathrm{T}}^{V}>120$ GeV region shows the biggest impact. Second, third and fourth ranked systematic uncertainties are also related to the W+hf modeling. The systematic uncertainties for Z+hf modeling are also highly ranked. Since they are dominant background on our signal region despite the difficulty of obtaining the control region in the data.

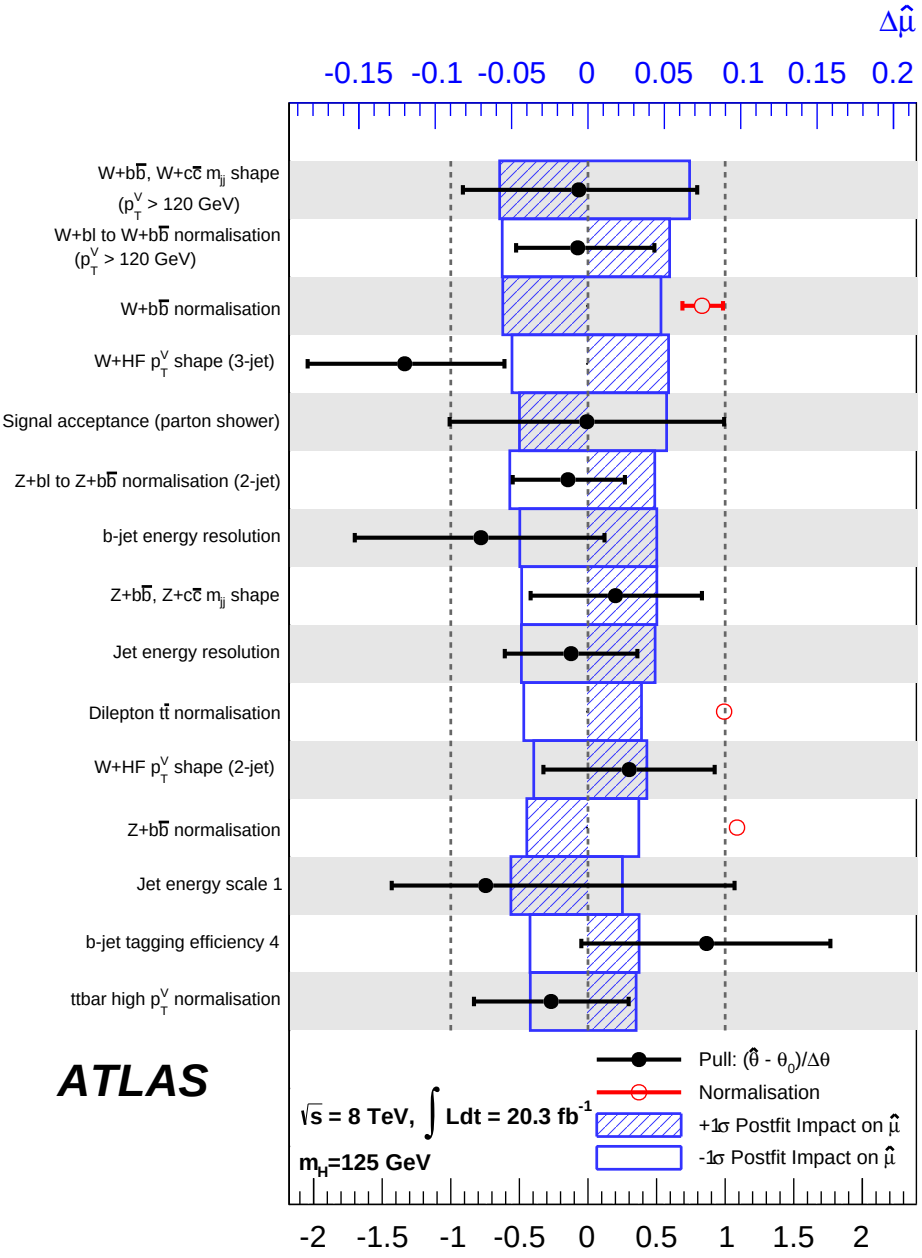

Figure 9.2: Impact of systematic uncertainties on the fitted signal strength μ listed vertically in decreasing order of their impacts for 8TeV MVA analysis. Higher rank nuisance parameters have larger impacts on the signal strength measurement. The black lines with the circle correspond the deviations of the post-fit nuisance parameters $\hat{\theta}$ from pre-fit values θ divided by their pre-fit uncertainties $\Delta\theta$. The red lines with the open circle show the post-fit normalisation scale factors. The boxes show the impact on signal strength μ.

Chapter 10

Results

10.1 m_{bb} distributions for cut-based analysis

The di-bjet mass distributions for cut-based analysis are shown in this section. The numbers of the data and expected backgrounds are shown in the figures in this section.

All backgrounds are constrained by the global fit explained in the previous section. Prefit background shapes are also shown in the plots. The signal strength in the plots are Standard Model expectation ($\mu = 1$). The data and estimated backgrounds show a good agreement within the statistical fluctuation.

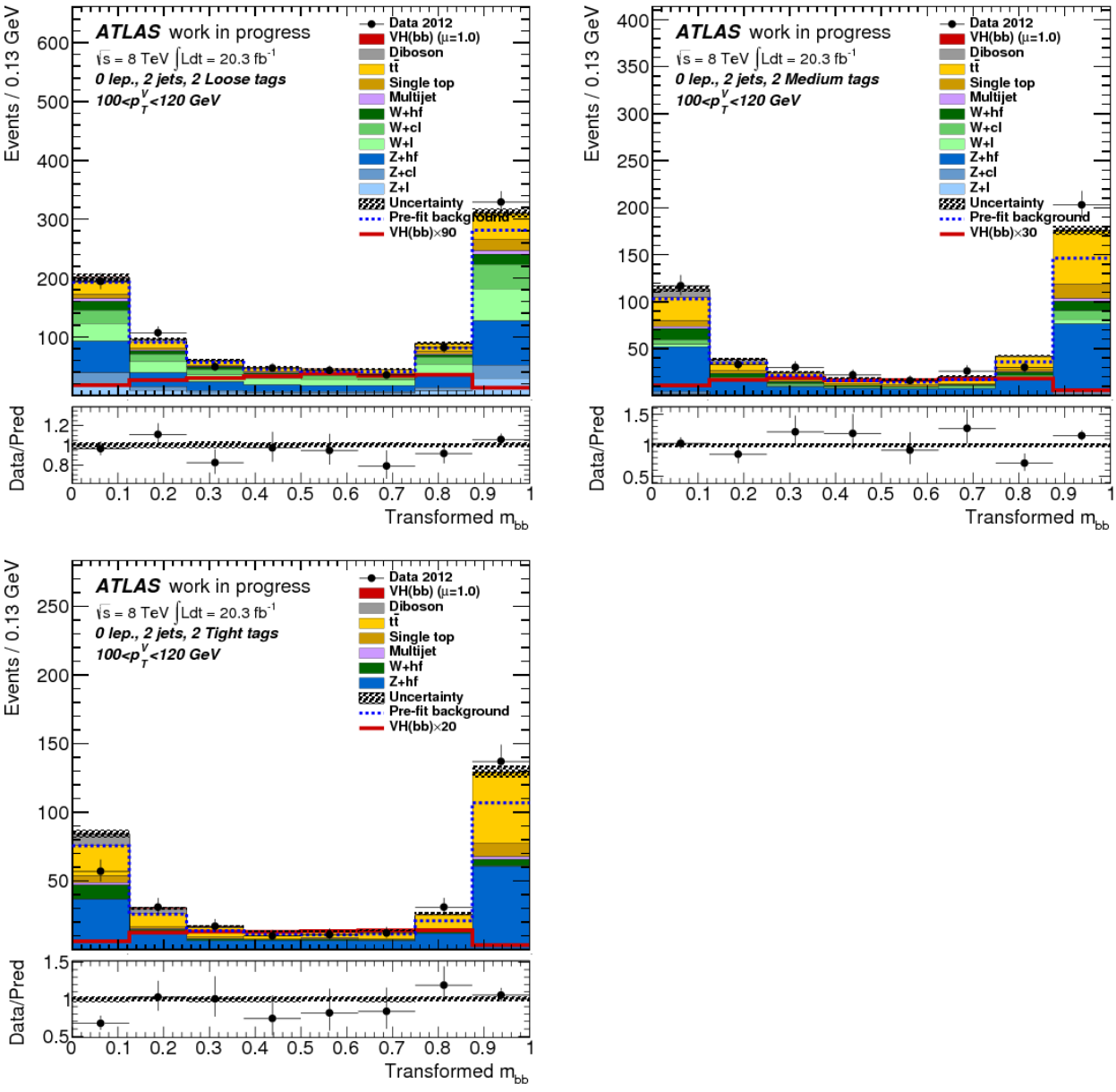

Figure 10.1: Di-jet distribution in zero-lepton channel with 2 b-tagged 2-jets and $100 < p_T^V < 120$ GeV. The two b-tagged jets are in three categories, 2 loose, 2 medium and 2 tight.

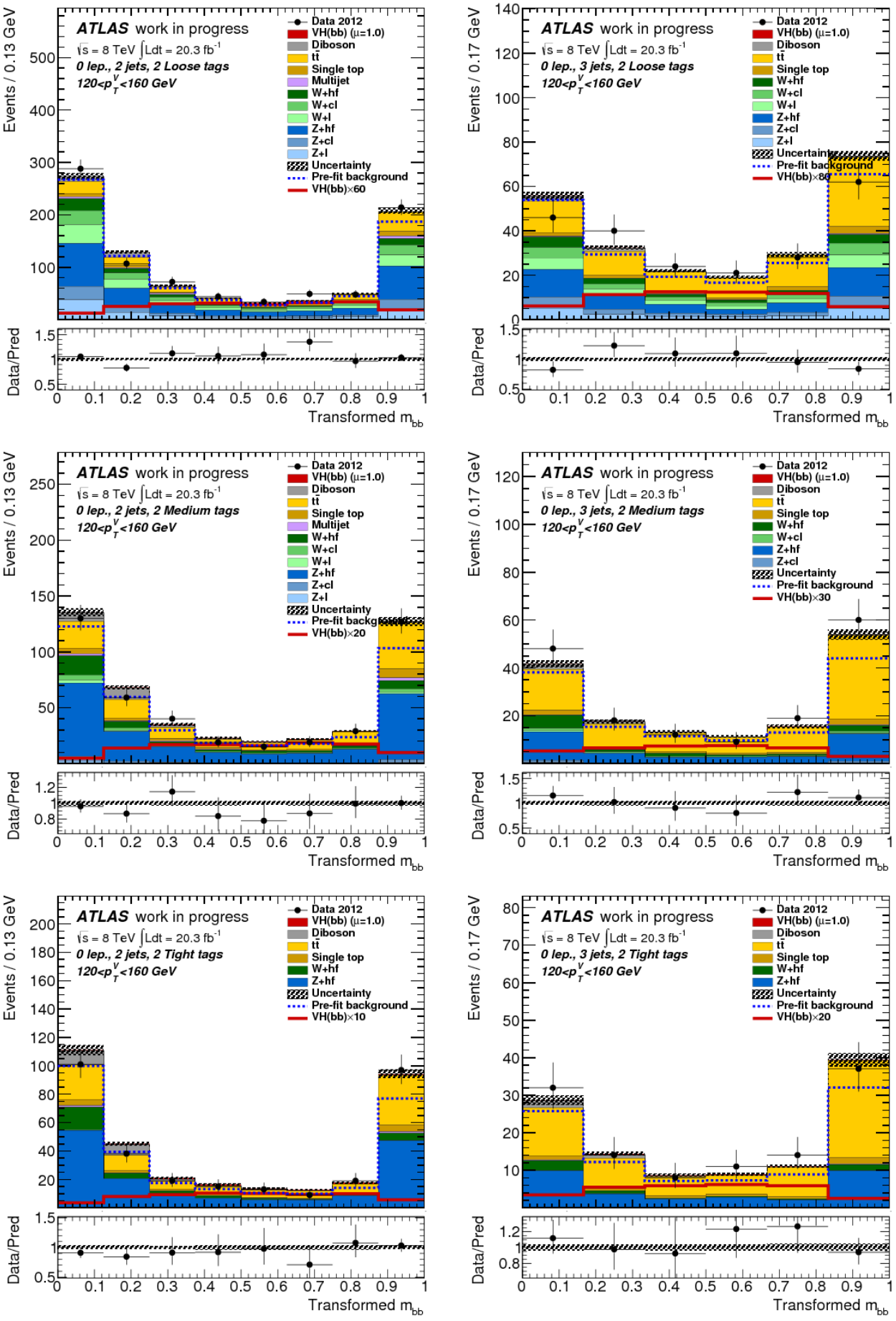

Figure 10.2: Di-jet distribution in zero-lepton channel with 2 b-tagged 2-jets and $120 < p_T^V < 160$ GeV. The two b-tagged jets are in three categories, 2 loose, 2 medium and 2 tight.

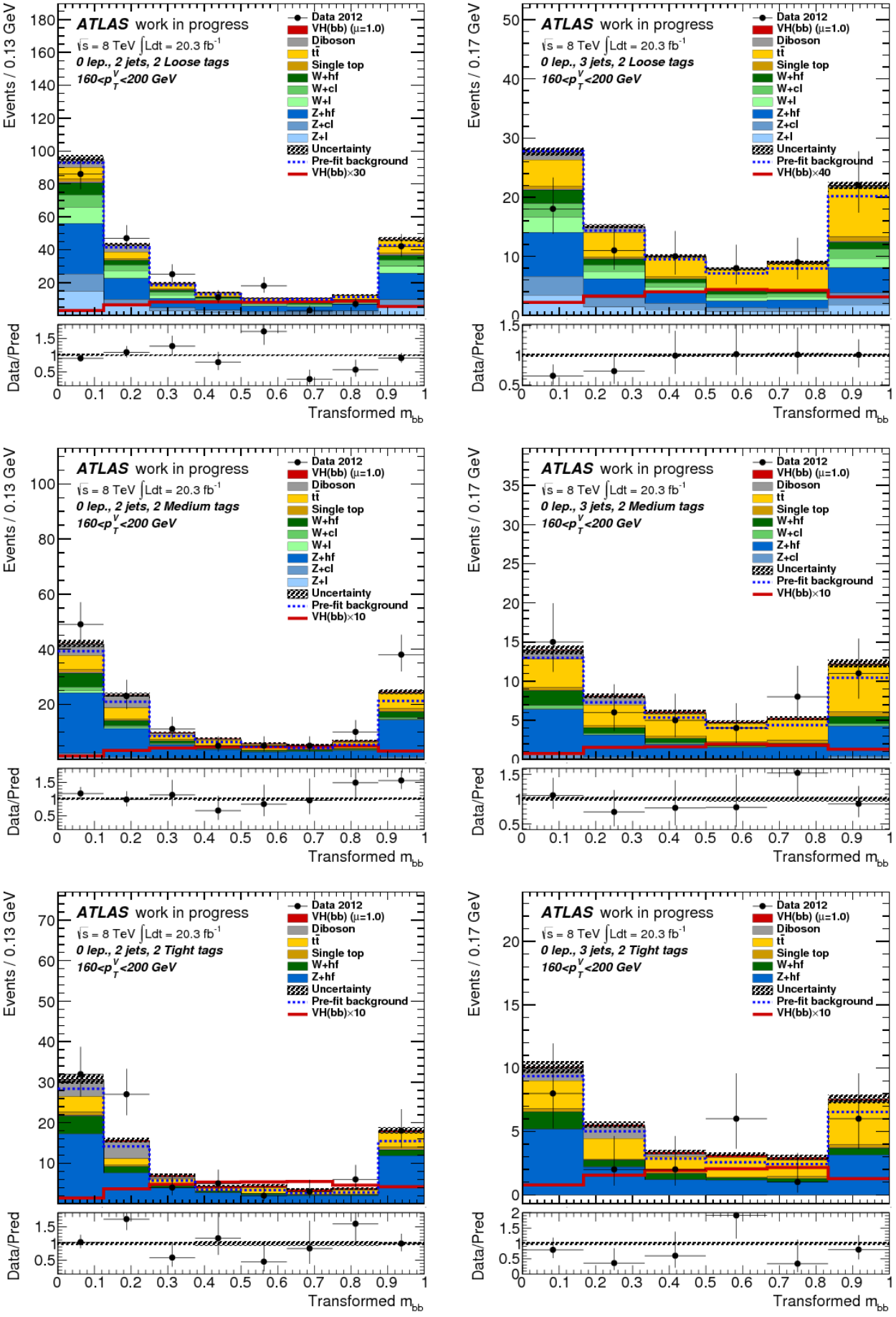

Figure 10.3: Di-jet distribution in zero-lepton channel with 2 b-tagged 2-jets and $160 < p_T^V < 200$ GeV. The two b-tagged jets are in three categories, 2 loose, 2 medium and 2 tight.

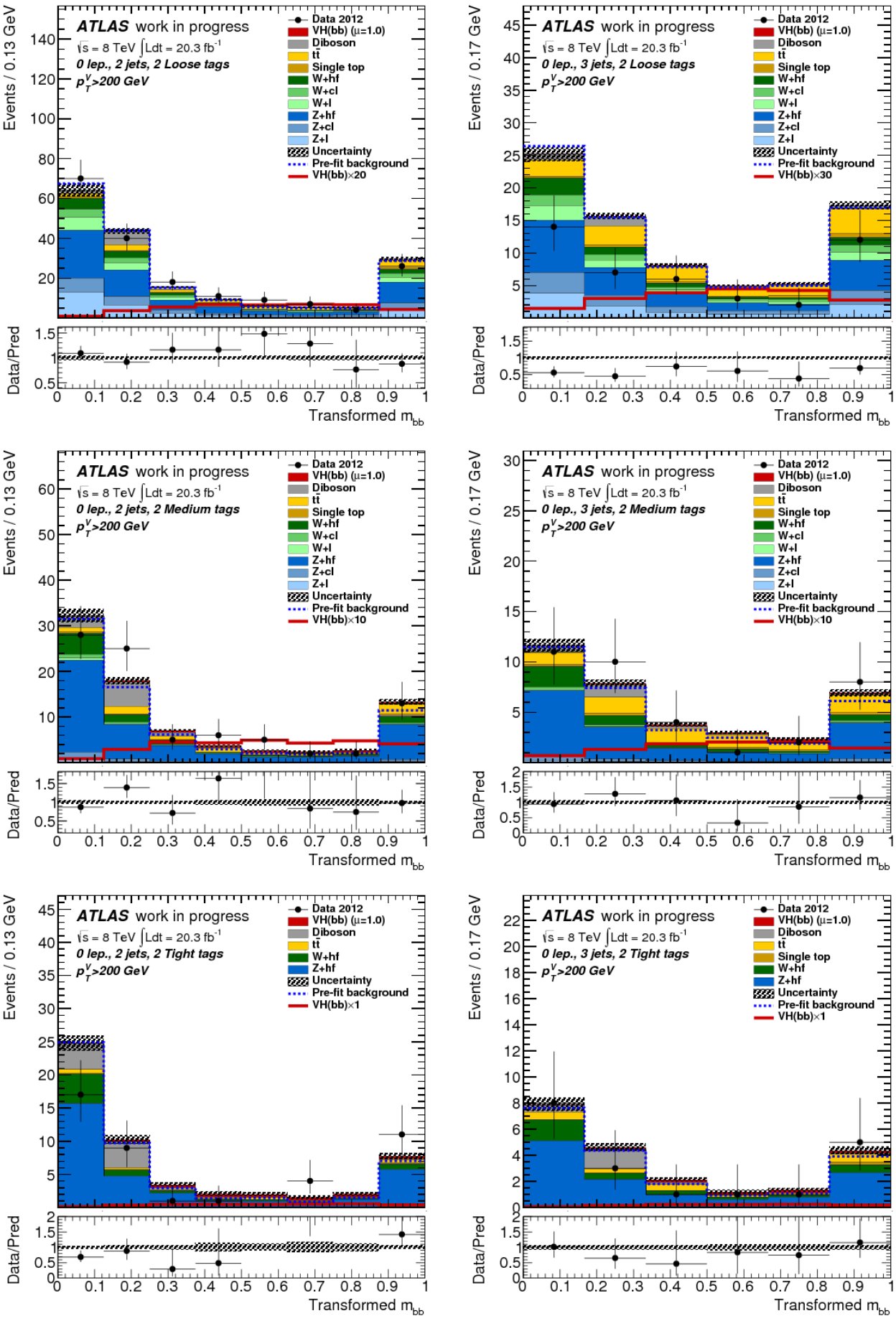

Figure 10.4: Di-jet distribution in zero-lepton channel with 2 b-tagged 2-jets and 200 $> p_T^V$ GeV. The two b-tagged jets are in three categories, 2 loose, 2 medium and 2 tight.

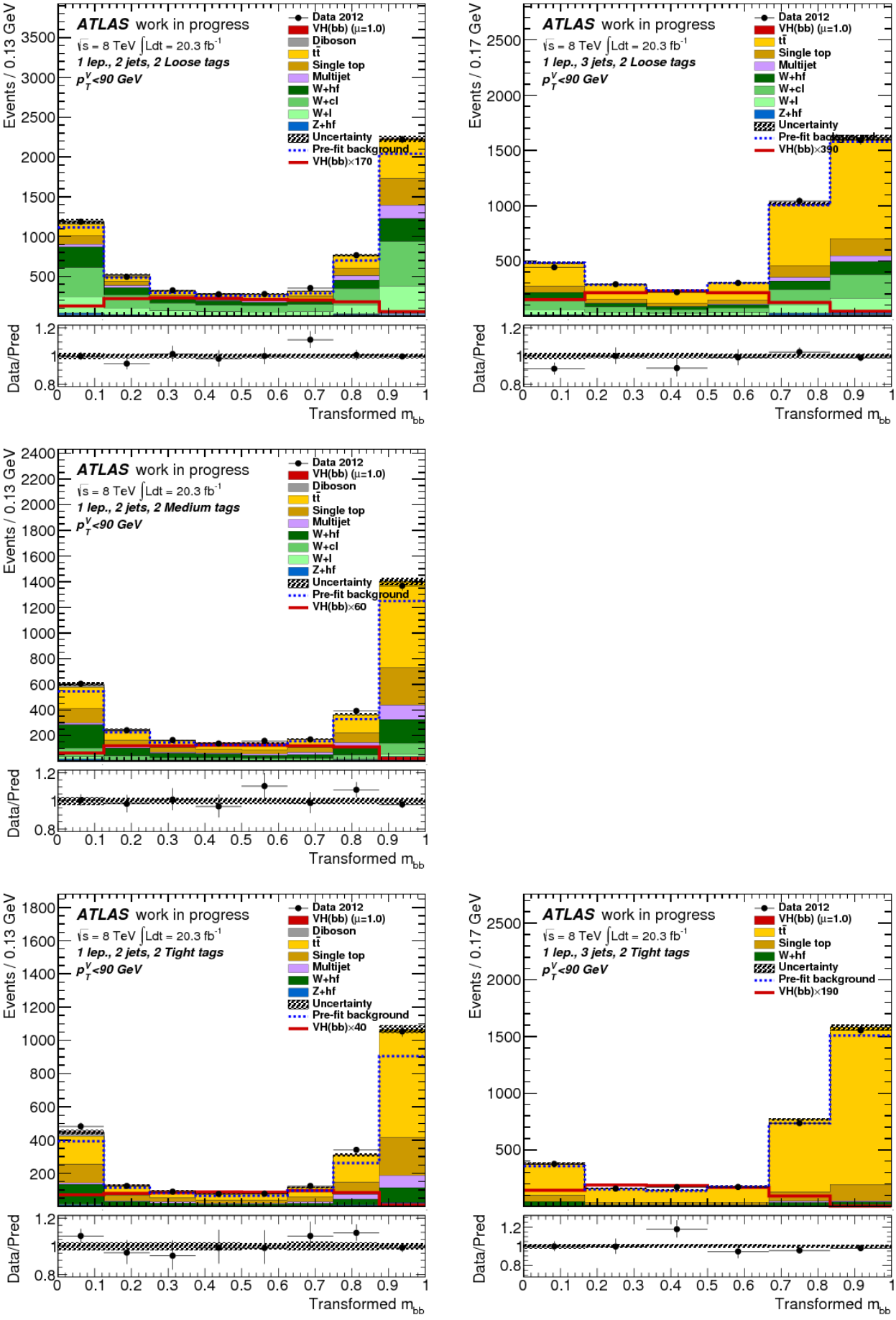

Figure 10.5: Di-jet distribution in one-lepton channel with 2 b-tagged 2-jets and $p_T^V < 90$ GeV. The two b-tagged jets are in three categories, 2 loose, 2 medium and 2 tight.

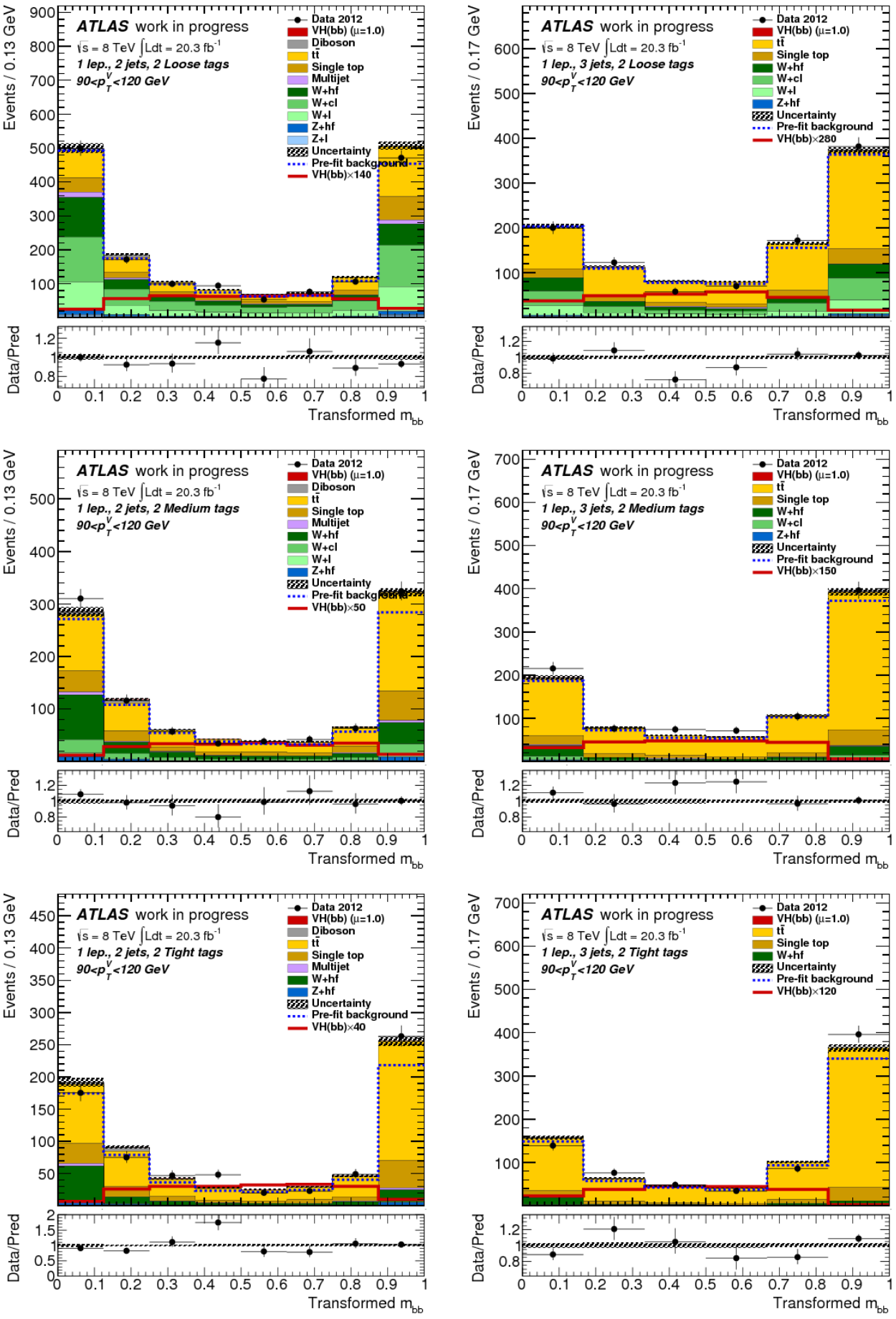

Figure 10.6: Di-jet distribution in one-lepton channel with 2 b-tagged 2-jets and $90 < p_T^V < 120$ GeV. The two b-tagged jets are in three categories, 2 loose, 2 medium and 2 tight.

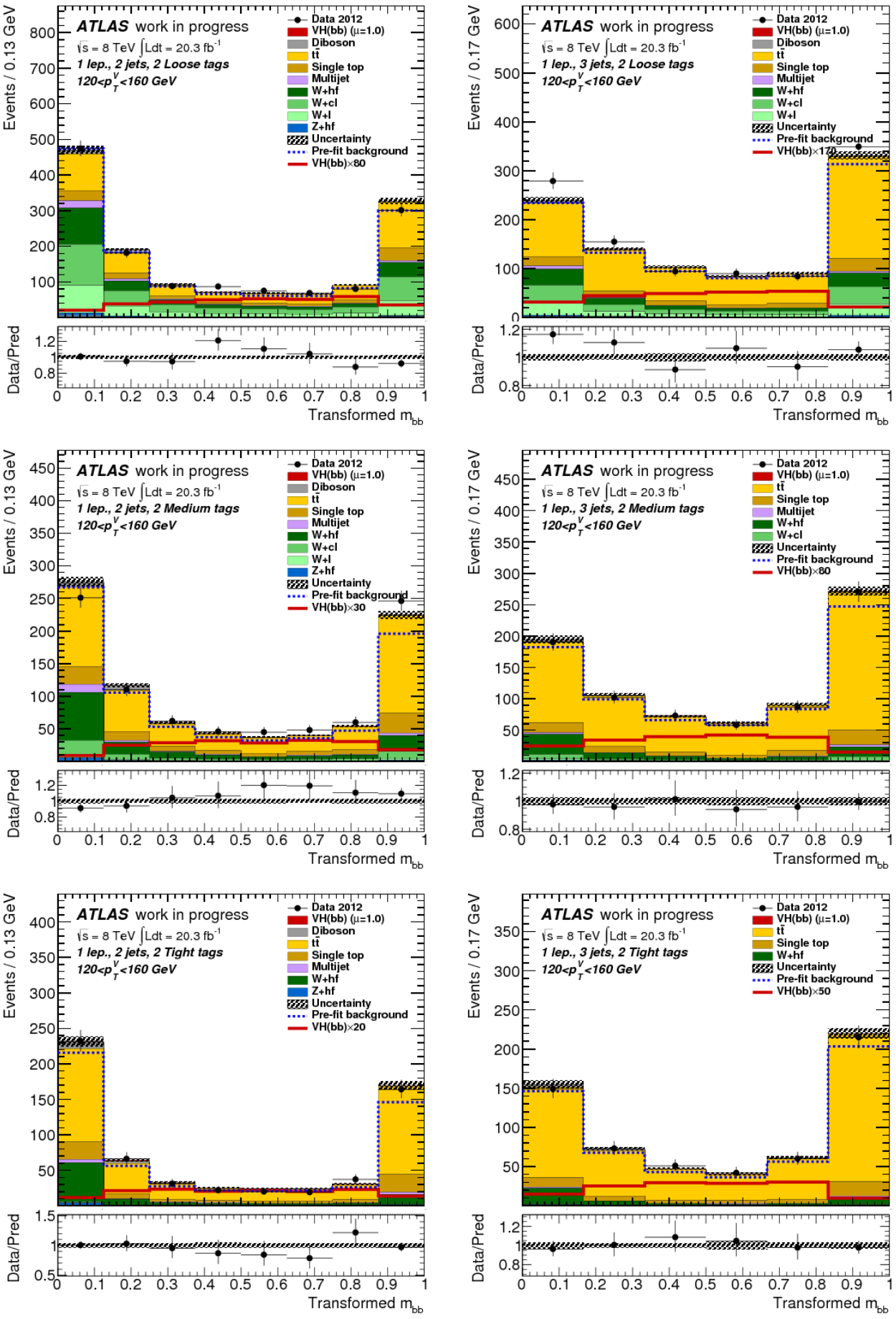

Figure 10.7: Di-jet distribution in one-lepton channel with 2 b-tagged 2-jets and $120 < p_T^V < 160$ GeV. The two b-tagged jets are in three categories, 2 loose, 2 medium and 2 tight.

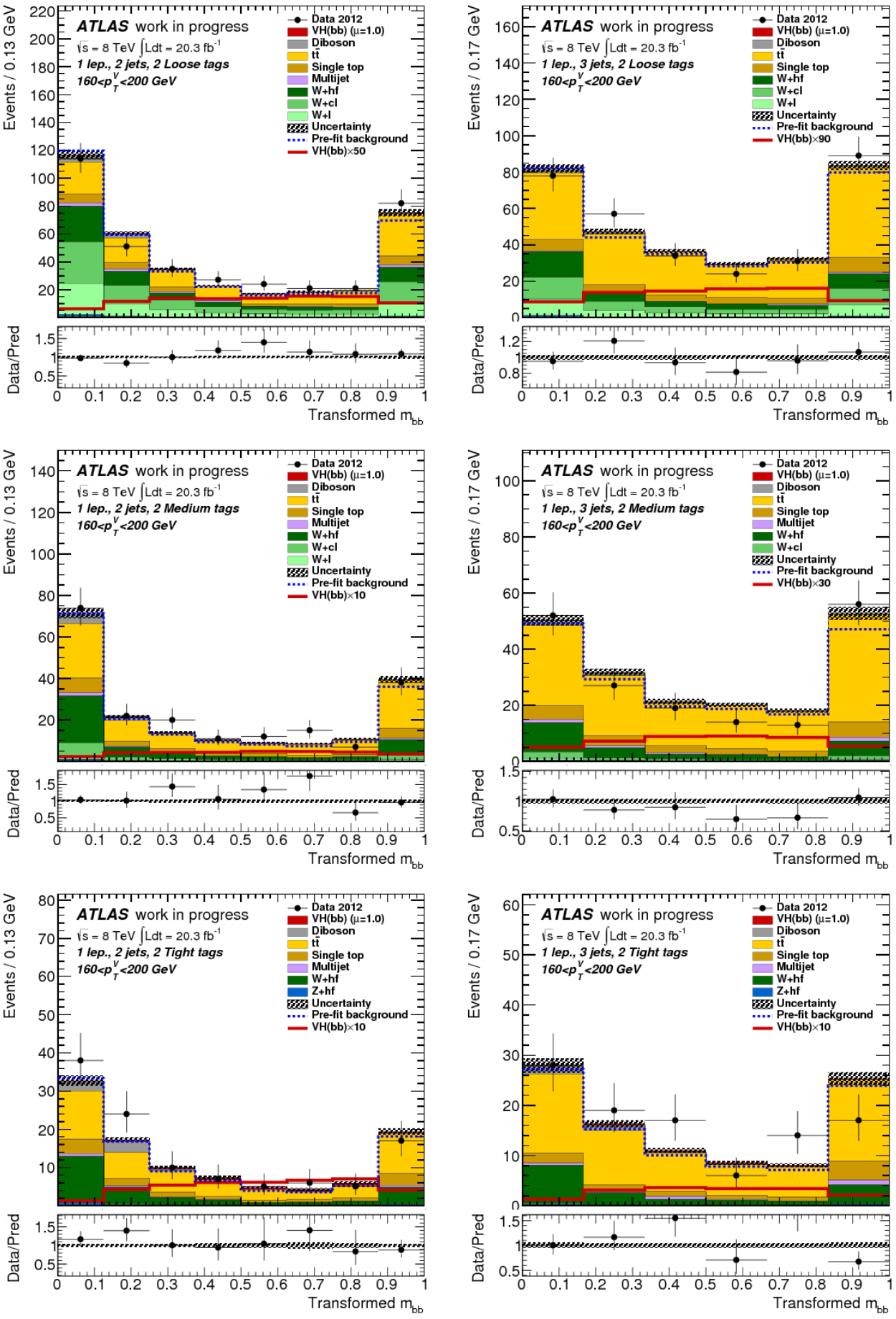

Figure 10.8: Di-jet distribution in one-lepton channel with 2 b-tagged 2-jets and $160 < p_T^V < 200$ GeV. The two b-tagged jets are in three categories, 2 loose, 2 medium and 2 tight.

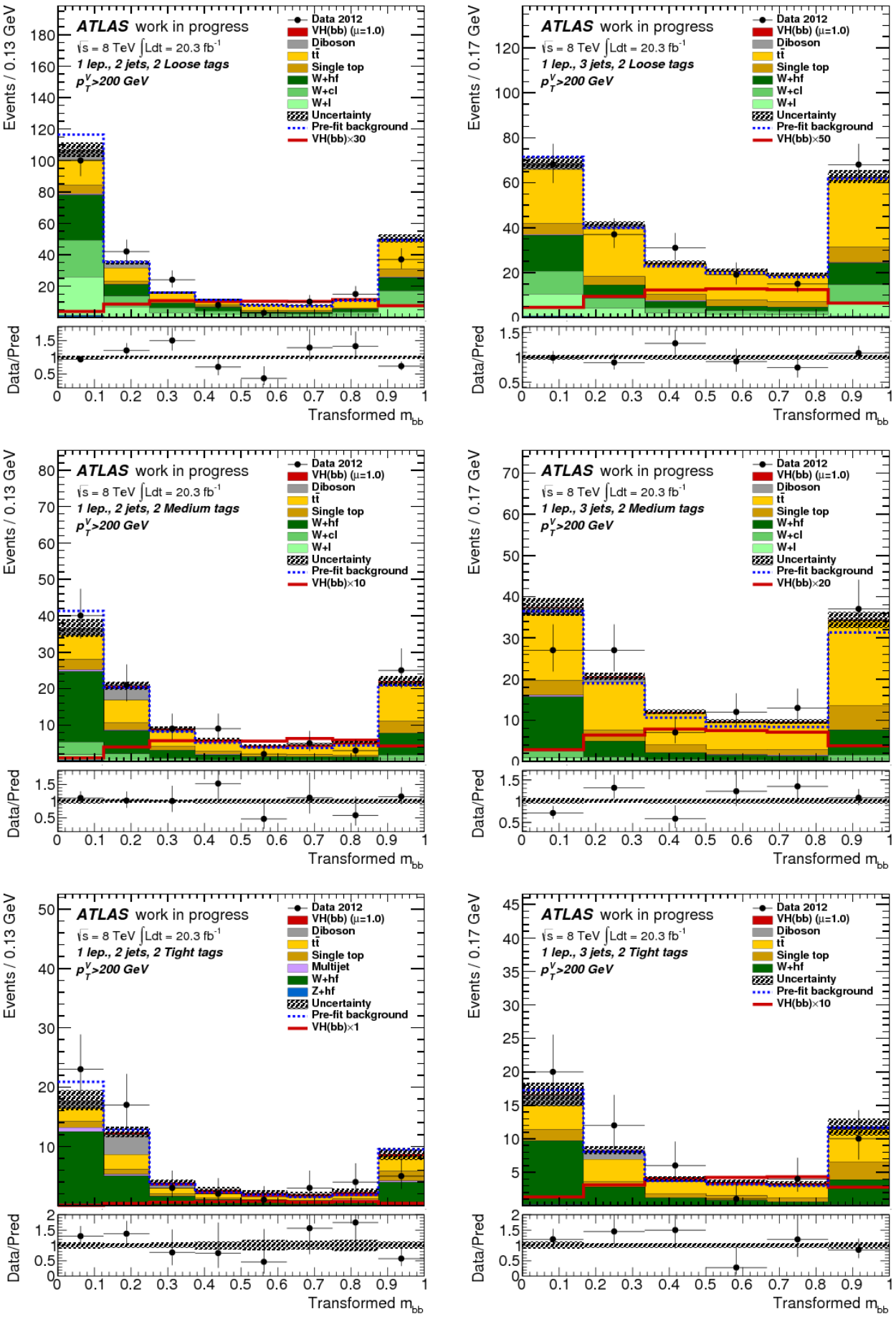

Figure 10.9: Di-jet distribution in one-lepton channel with 2 b-tagged 2-jets and $p_T^V > 200$ GeV. The two b-tagged jets are in three categories, 2 loose, 2 medium and 2 tight.

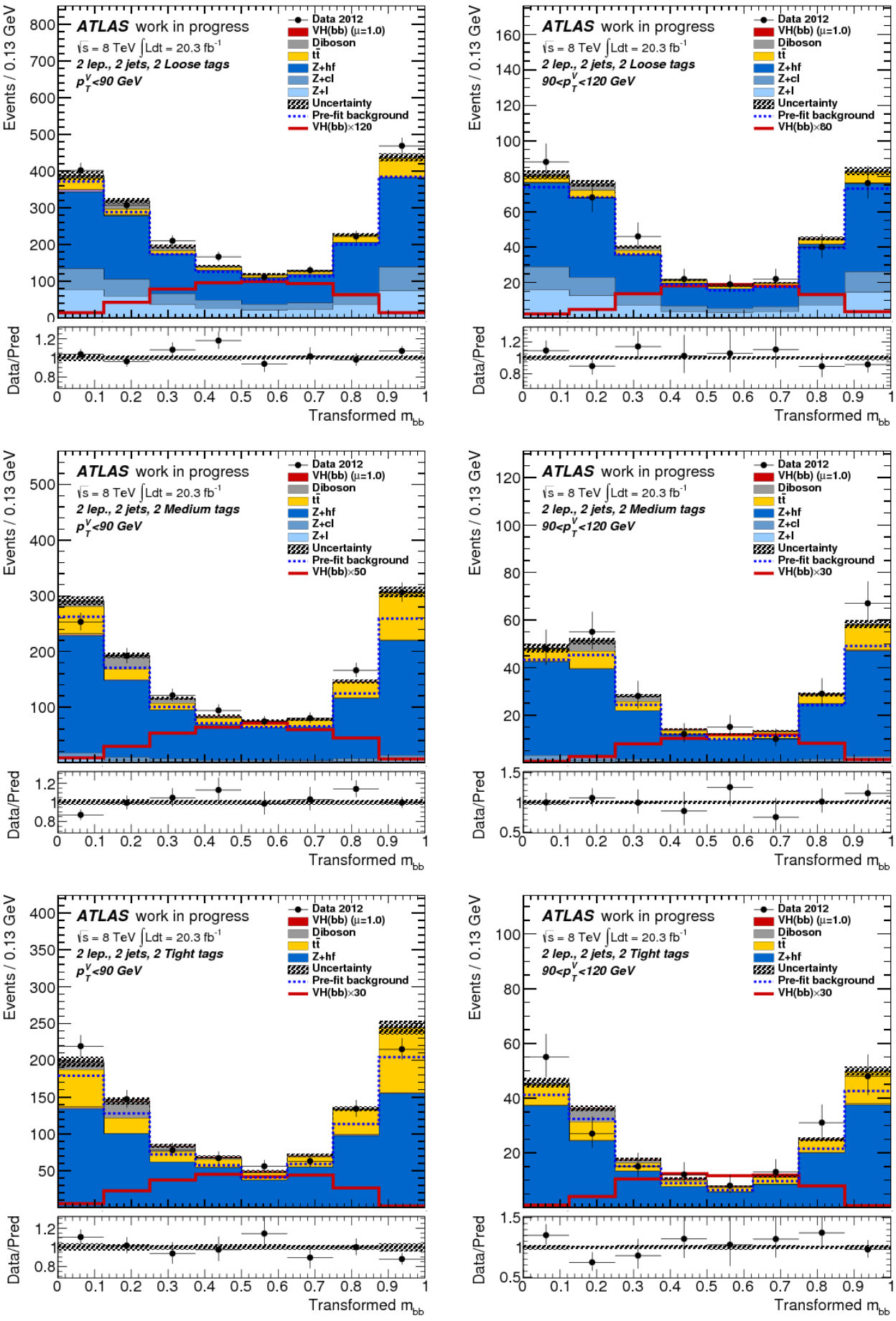

Figure 10.10: Di-jet distribution in two-lepton channel with 2 b-tagged 2-jets and $p_T^V < 90$ GeV. The two b-tagged jets are in three categories, 2 loose, 2 medium and 2 tight.

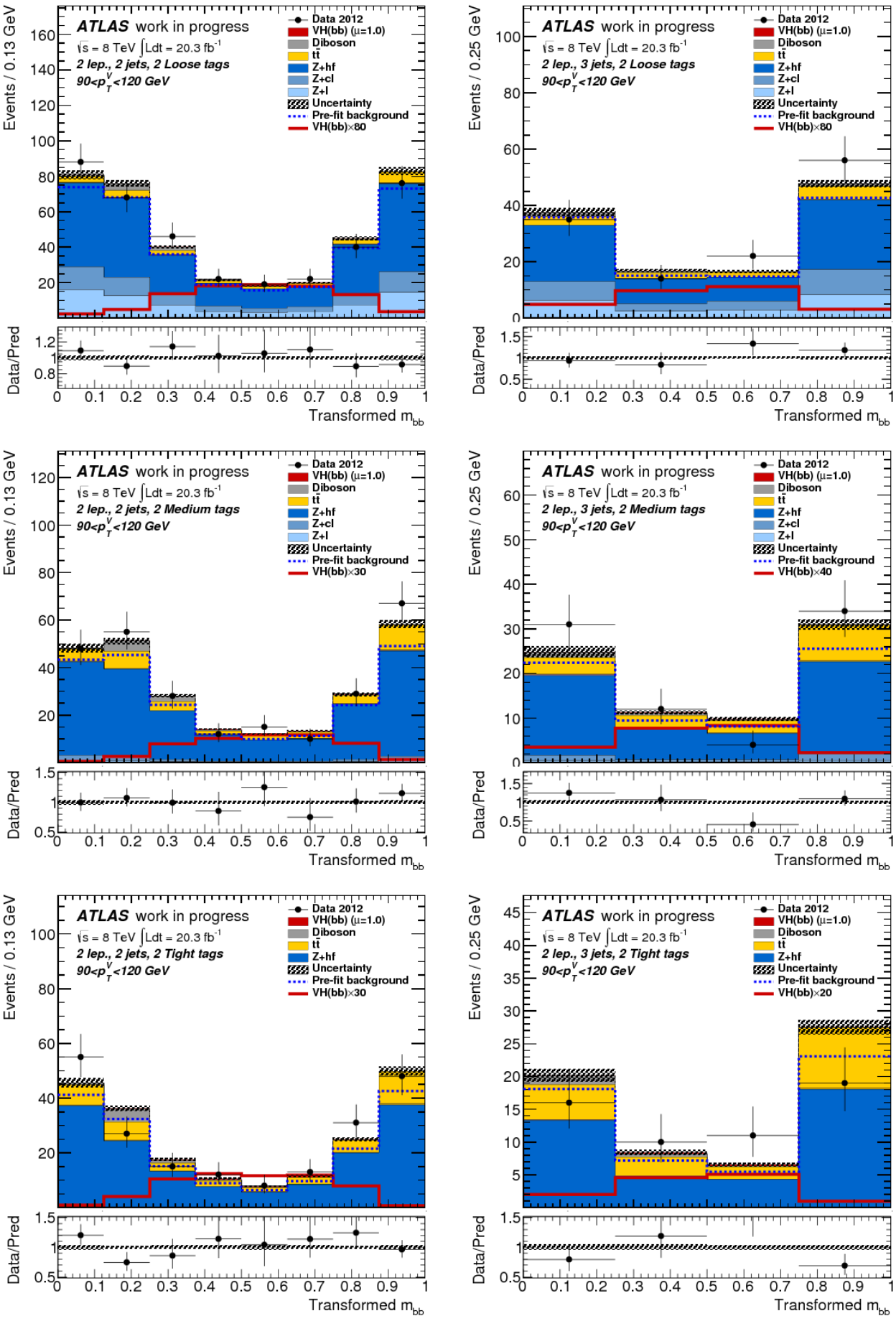

Figure 10.11: Di-jet distribution in two-lepton channel with 2 b-tagged 2-jets and $90 < p_T^V < 120$ GeV. The two b-tagged jets are in three categories, 2 loose, 2 medium and 2 tight.

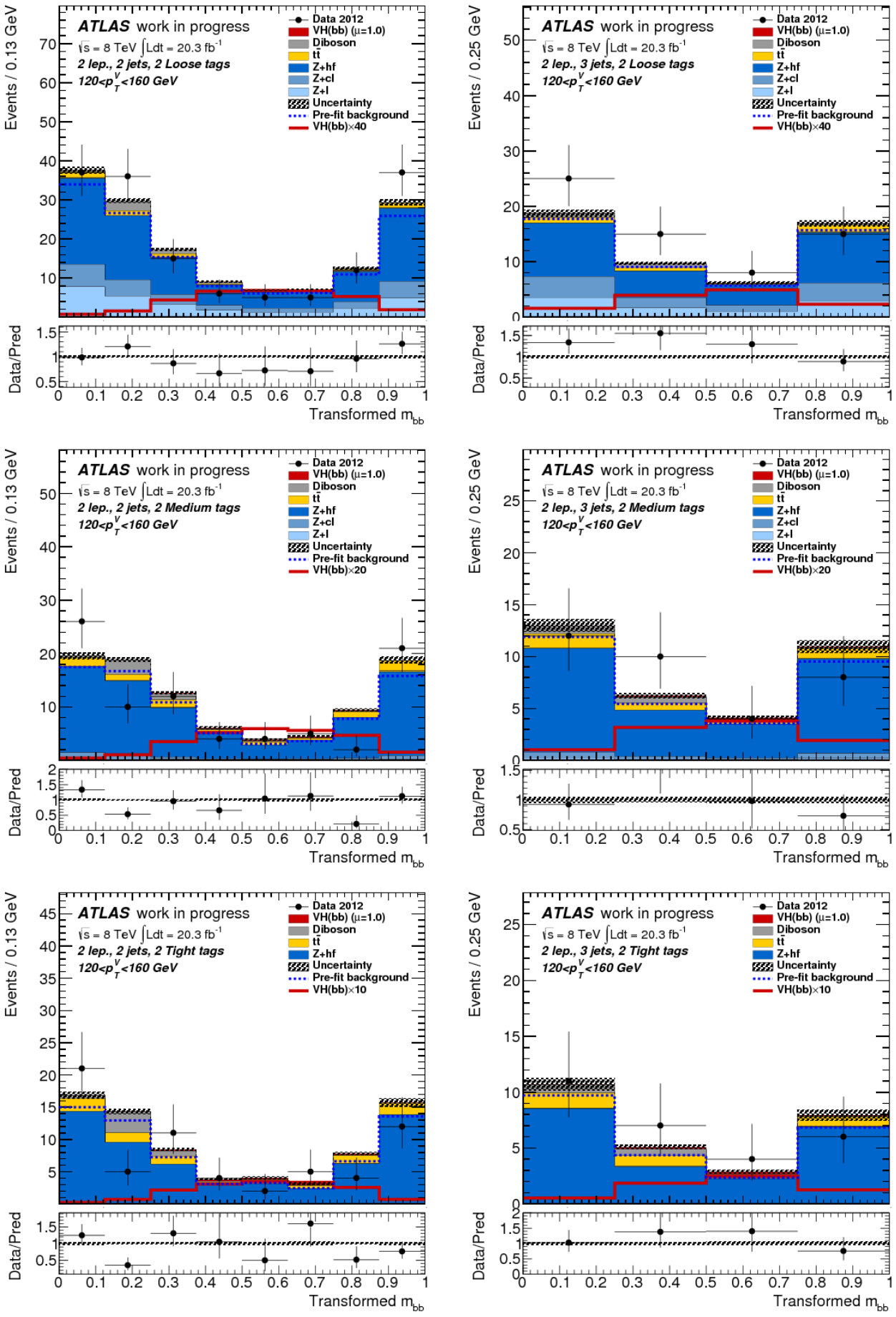

Figure 10.12: Di-jet distribution in two-lepton channel with 2 b-tagged 2-jets and $120 < p_T^V < 160$ GeV. The two b-tagged jets are in three categories, 2 loose, 2 medium and 2 tight.

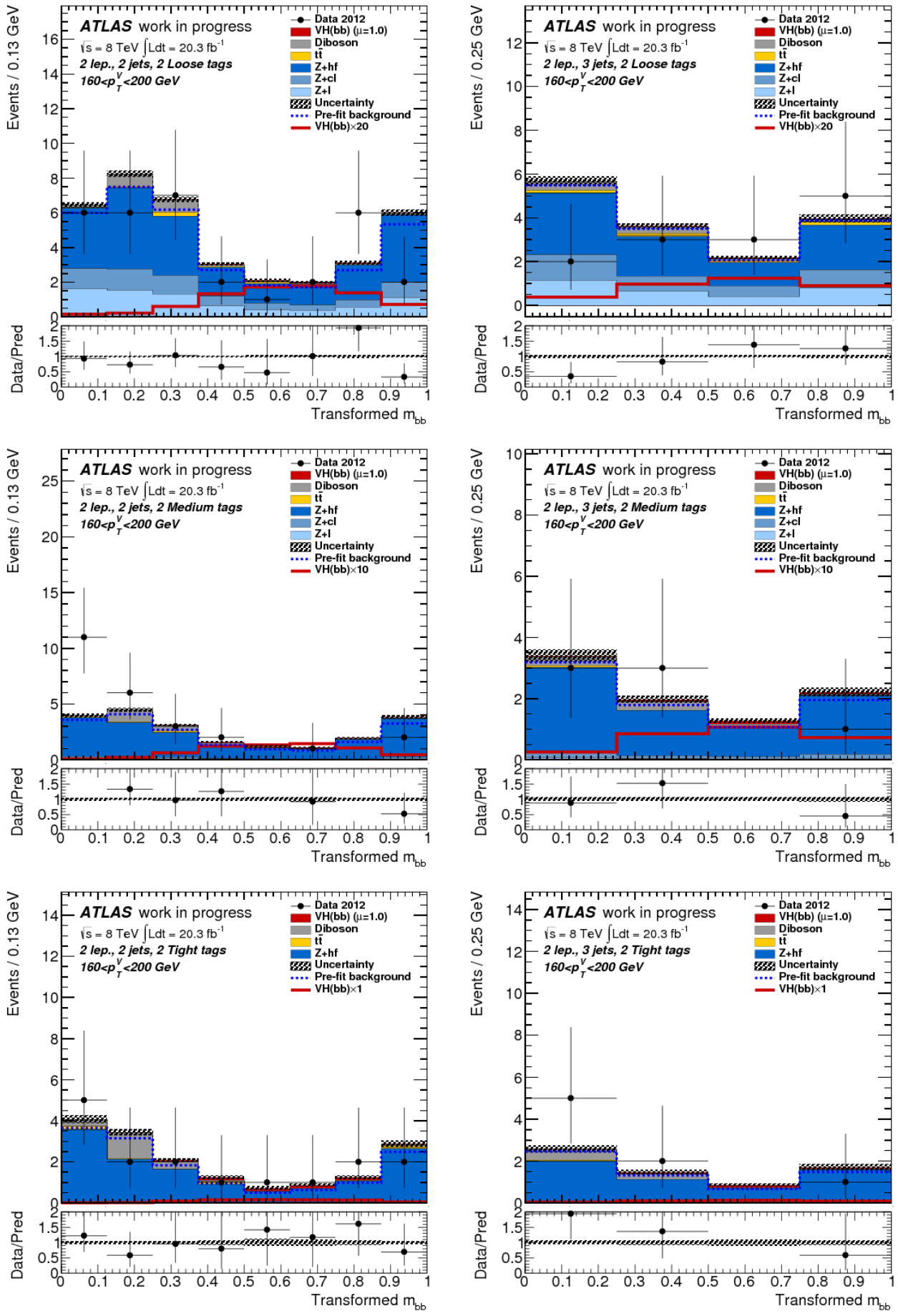

Figure 10.13: Di-jet distribution in two-lepton channel with 2 b-tagged 2-jets and $160 < p_T^V < 200$ GeV. The two b-tagged jets are in three categories, 2 loose, 2 medium and 2 tight.

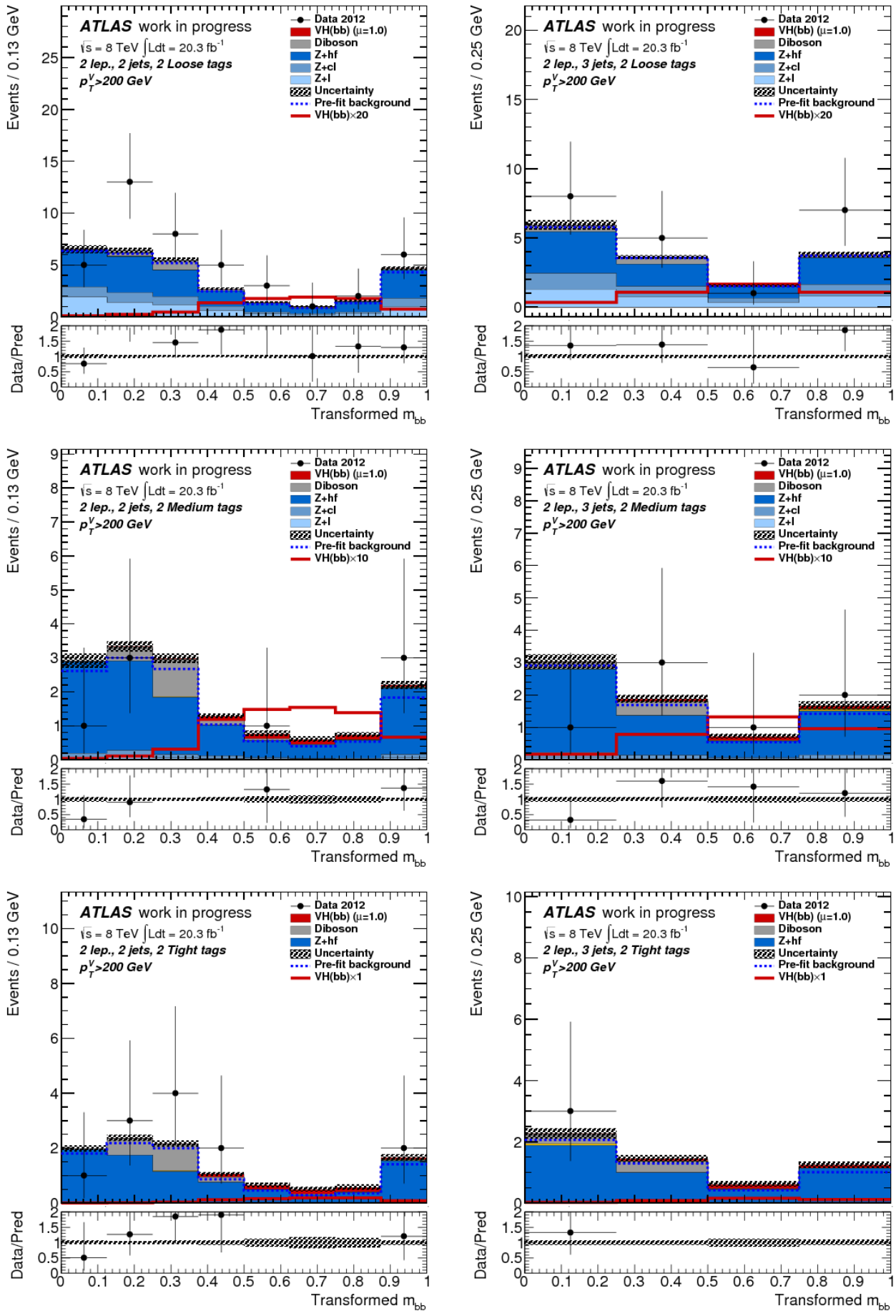

Figure 10.14: Di-jet distribution in two-lepton channel with 2 b-tagged 2-jets and $p_T^V > 200$ GeV. The two b-tagged jets are in three categories, 2 loose, 2 medium and 2 tight.

10.2 BDT output distributions for MVA analysis

The BDT output distributions and b-tag weight(MV1c) distributions for MVA based analysis are shown in this section.

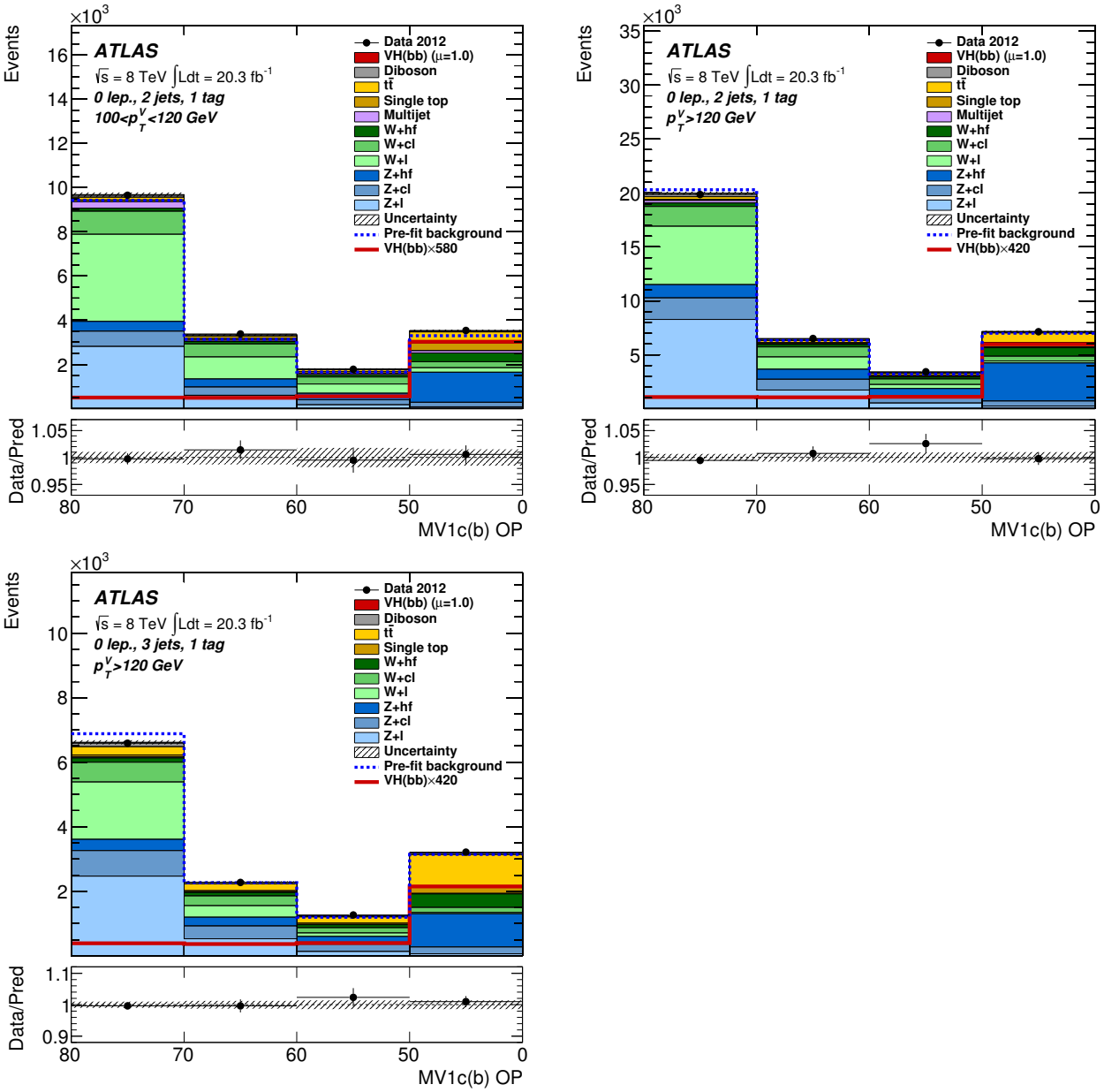

Figure 10.15: BDT input variables as function of b-tagging efficiency in the zero-lepton channel for the 1-b-tag categories with 100< p_{T}^{V} <120 GeV and p_{T}^{V} >120 GeV (2 jets and 3 jets identified). The horizontal is the b-tagging efficiency at fixed efficiency points, with the left bin boundaries denote the operating points of the MV1c b-tagging algorithm.

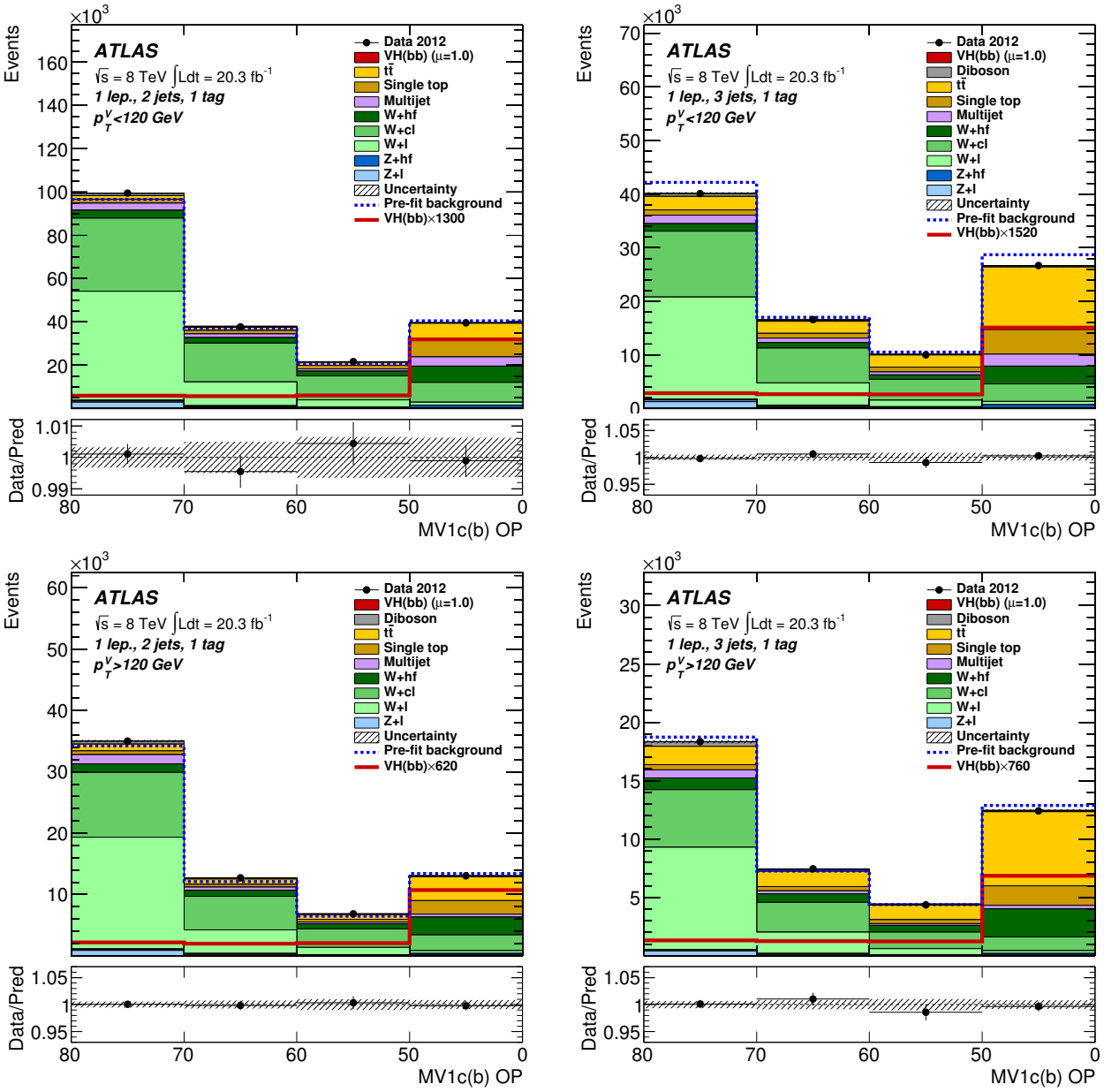

Figure 10.16: BDT input variables as function of b-tagging efficiency in the one-lepton channel for the 1-b-tag categories with p_{T}^{V} <120 GeV and p_{T}^{V} >120 GeV (2 jets and 3 jets identified). The horizontal is the b-tagging efficiency at fixed efficiency points, with the left bin boundaries denote the operating points of the MV1c b-tagging algorithm.

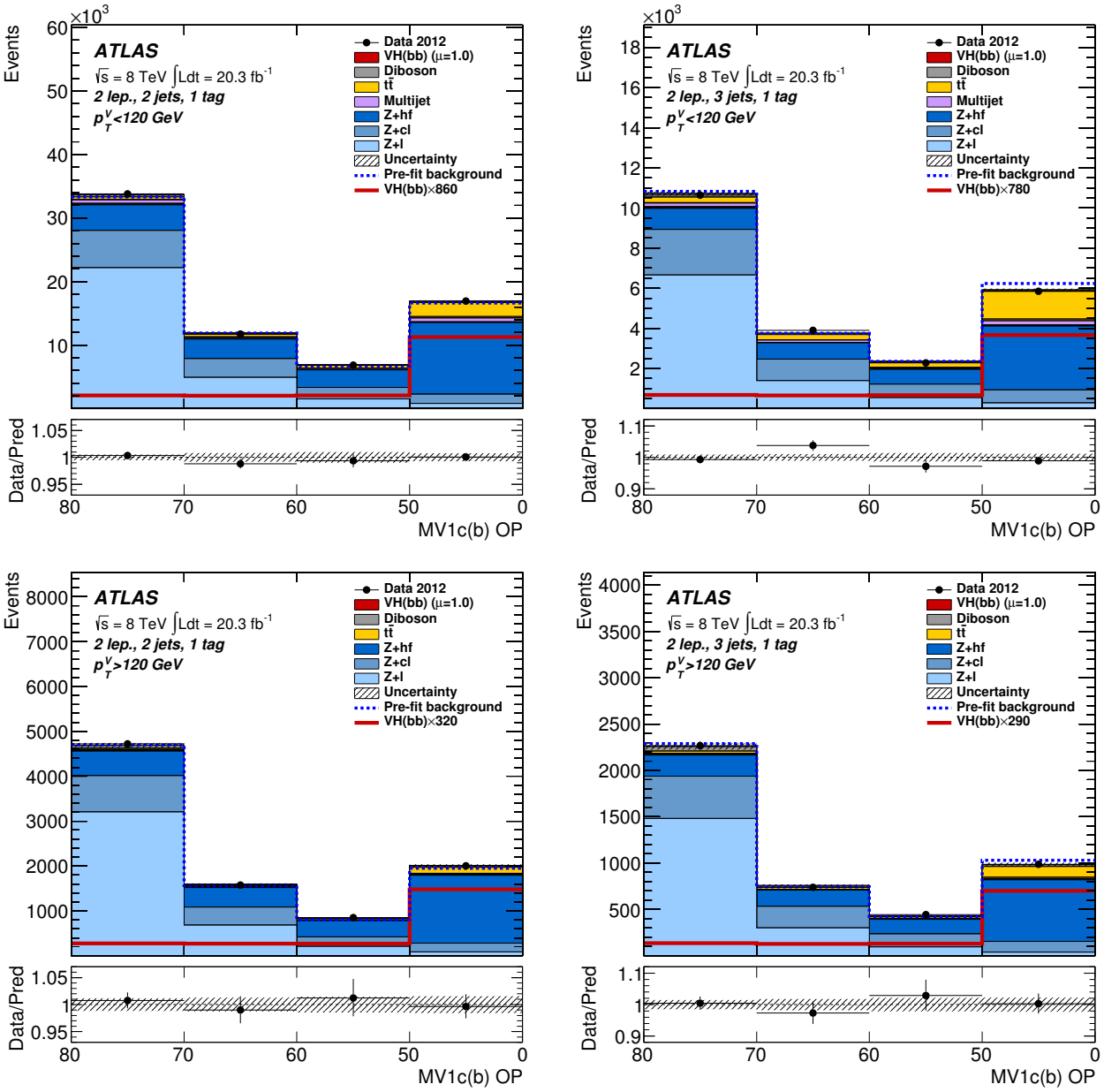

Figure 10.17: BDT input variables as function of b-tagging efficiency in the two-lepton channel for the 1-b-tag categories with p_{T}^{V} <120 GeV and p_{T}^{V} >120 GeV (2 jets and 3 jets identified). The horizontal is the b-tagging efficiency at fixed efficiency points, with the left bin boundaries denote the operating points of the MV1c b-tagging algorithm.

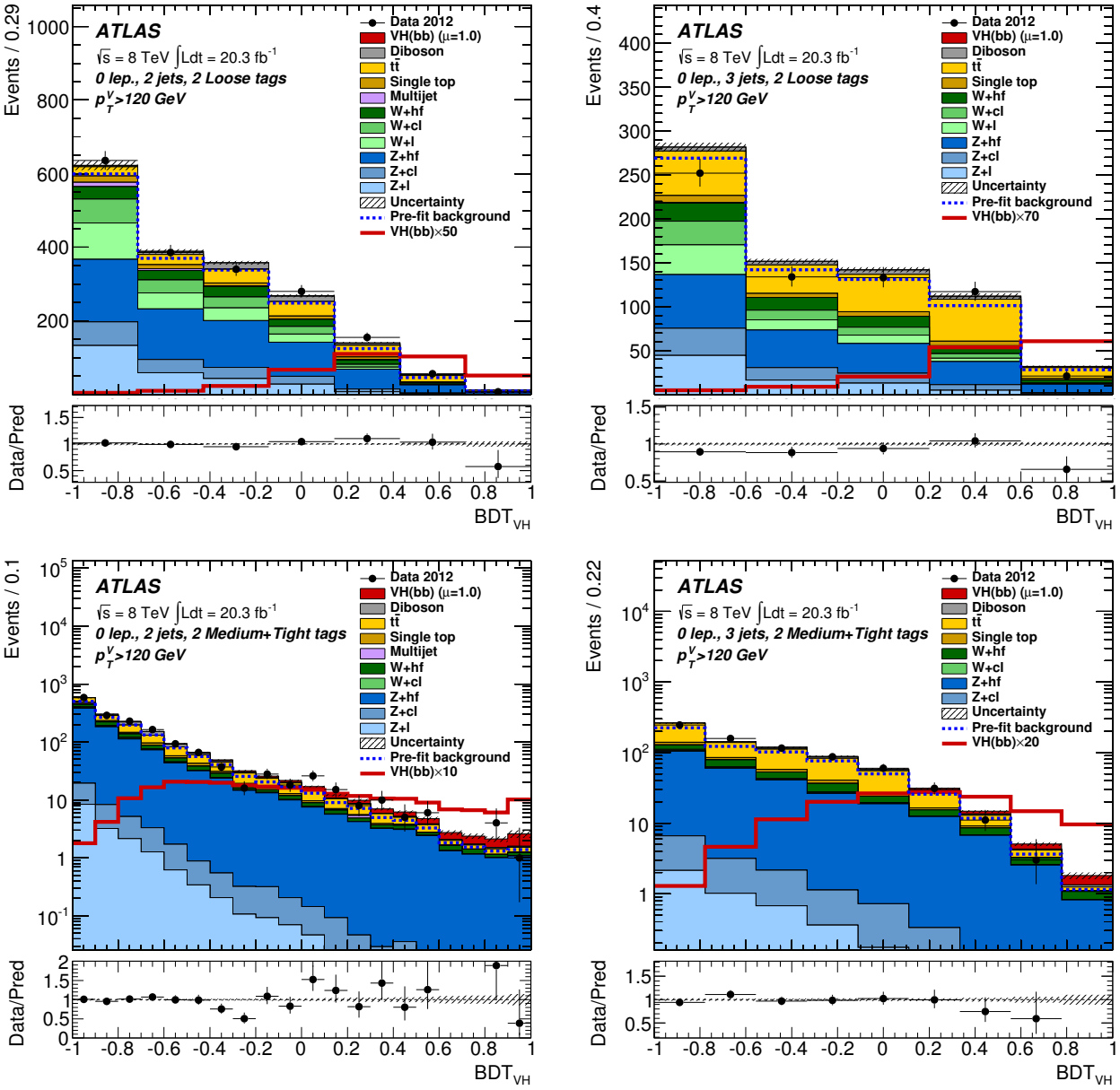

Figure 10.18: MVA distributions in zero-lepton channel for the 2-b-tag categories with 2-jets (left) and 3-jets (right). The two b-tagged jets are in two categories, 2 loose (top) and 2 medium+tight (bottom).

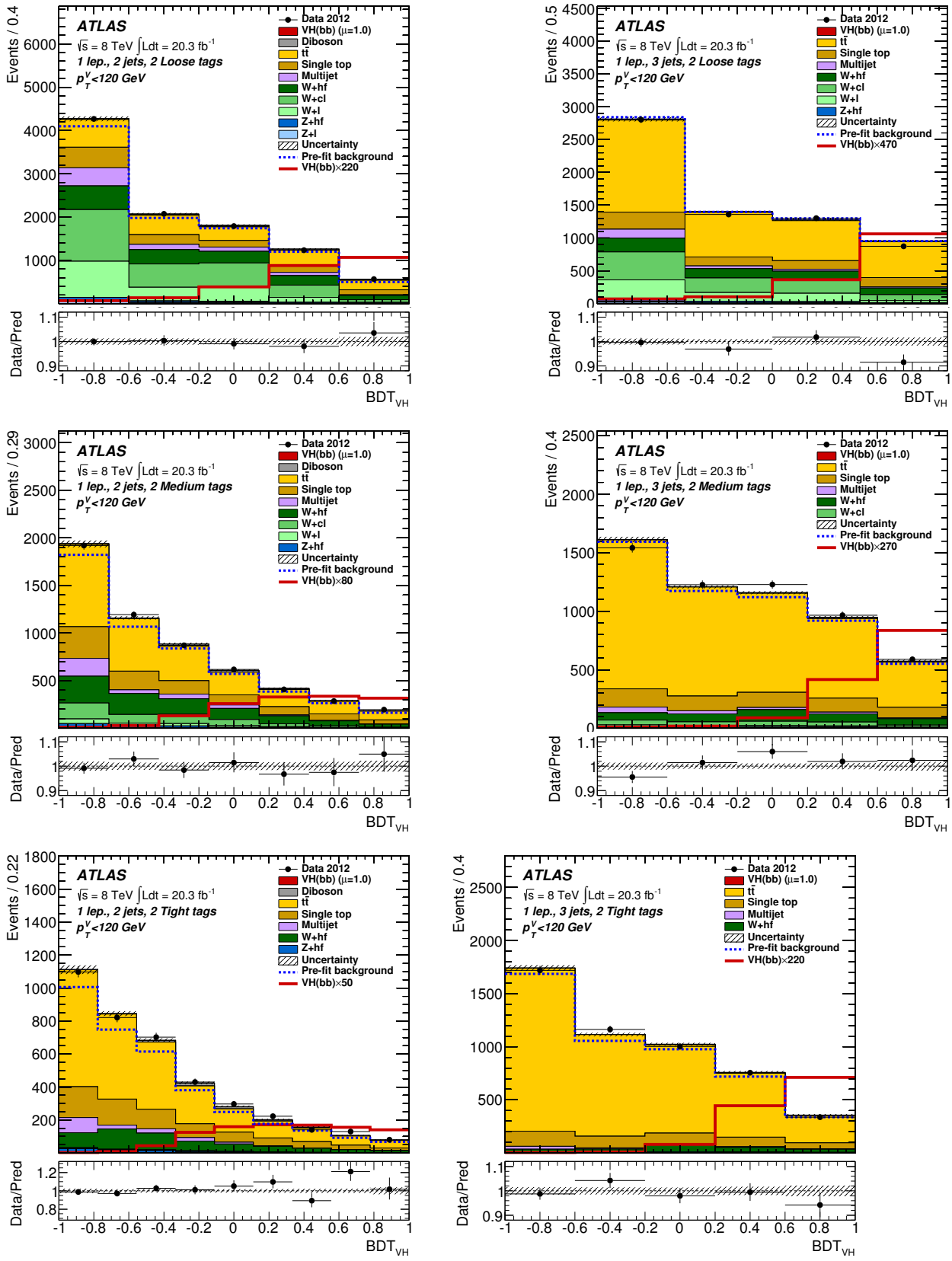

Figure 10.19: MVA distributions in one-lepton channel for the 2-b-tag categories with 2-jets (left) and 3-jets (right) and $p_T^V < 120$ GeV. The two b-tagged jets are in three categories, 2 loose (top), 2 medium (middle) and 2 tight (bottom).

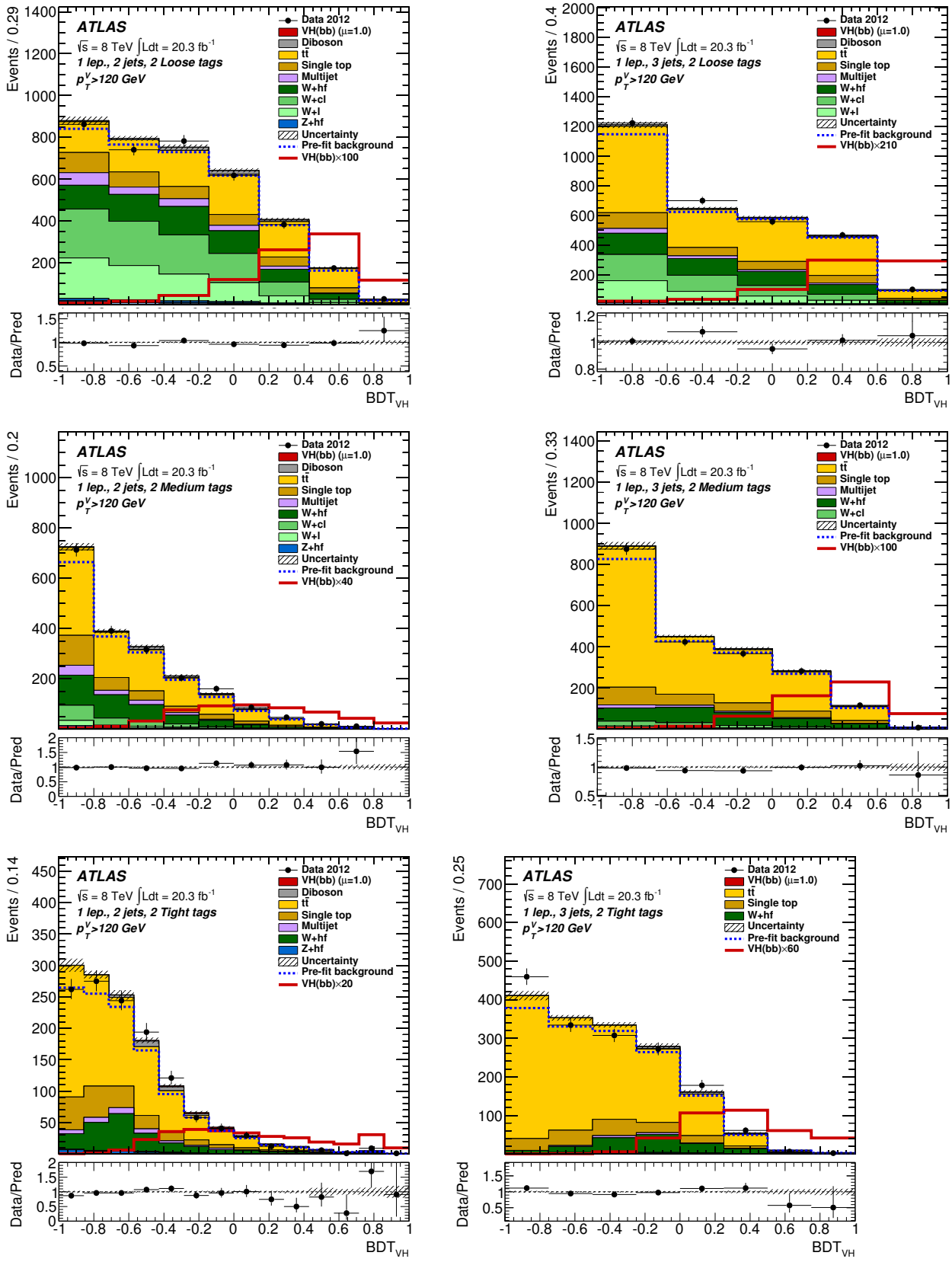

Figure 10.20: MVA distributions in one-lepton channel for the 2-b-tag categories with 2-jets (left) and 3-jets (right) and $p_T^V > 120$ GeV. The two b-tagged jets are in three categories, 2 loose (top), 2 medium (middle) and 2 tight (bottom).

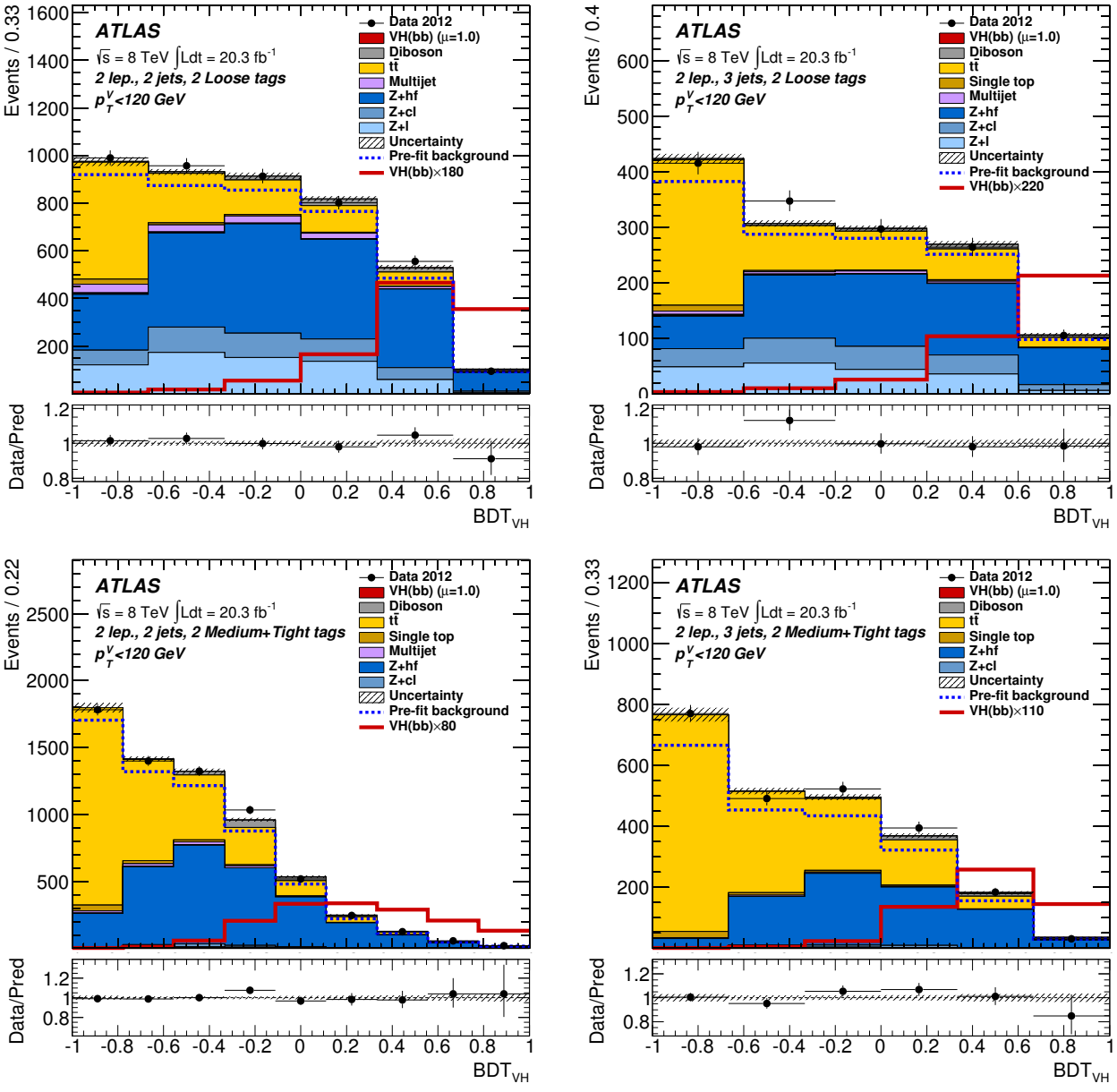

Figure 10.21: MVA distributions in two-lepton channel for the 2-b-tag categories with 2-jets (left) and 3-jets (right) and $p_T^V < 120$ GeV. The two b-tagged jets are in two categories, 2 loose (top) and 2 medium+tight (bottom).

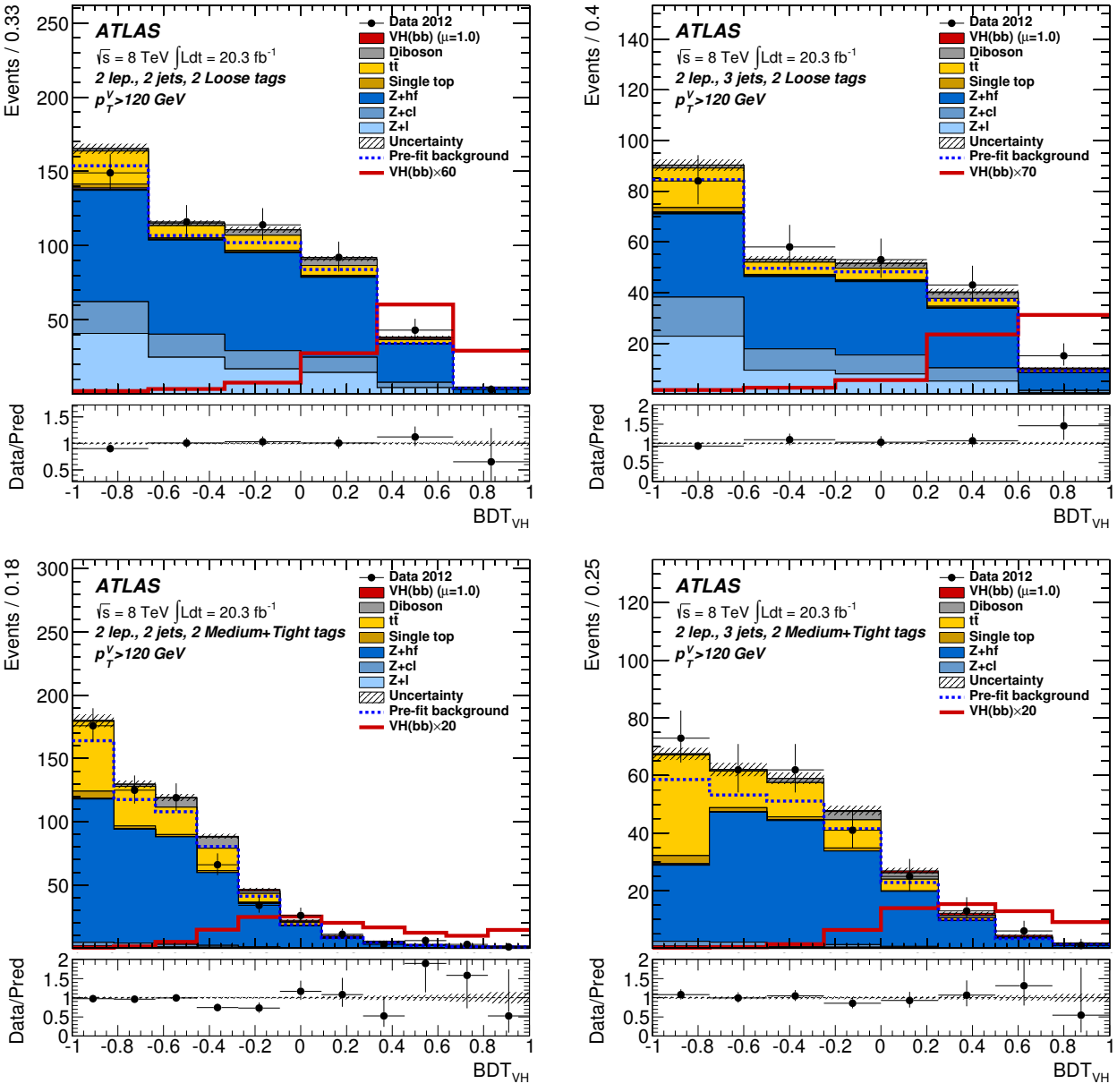

Figure 10.22: MVA distributions in two-lepton channel for the 2-b-tag categories with 2-jets (left) and 3-jets (right) and $p_T^V > 120$ GeV. The two b-tagged jets are in two categories, 2 loose (top) and 2 medium+tight (bottom).

10.3 Exclusion limit, significance and signal strength

The exclusion limit for $H \to bb$ production, signal strength and its significance are obtained by the binned maximum likelihood fit. The results are summarized as follows:

1. The observed limit for the Standard Model Higgs (m_H = 125 GeV) production is 1.2 times the SM, while the expected limit is 0.8. Figure 10.23 shows the observed and expected, both Higgs existence and non-existence hypotheses, 95% CL exclusion limits as a function of the assumed Higgs mass. The background only probability p_0 to explain the observed signal is 8%, while the expected value is 0.5% as shown in Figure 10.24. The corresponding significance of the observed excess is 1.4σ, to be compared to an expectation of 2.6σ for the SM Higgs.

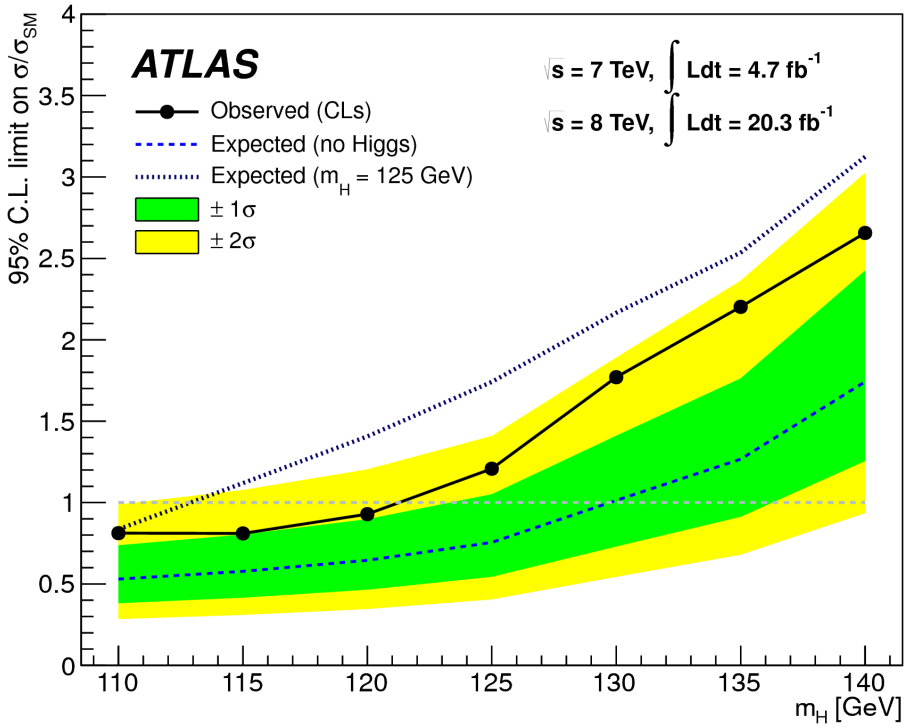

Figure 10.23: Observed and expected 95% CL cross-section upper limits normalised to the Standard Model Higgs boson production cross section times branching ratio. The dotted curve with bands are for the case where Higgs does not exist. The data points are to be compared also with the expected limit (dashed curve) in the case where 125 GeV/c^2 SM Higgs exists.

2. The signal strength normalised by the Standard Model Higgs production is obtained by the MVA analysis as

$$\mu = 0.51 \pm 0.31(\text{stat.}) \pm 0.24(\text{syst.}). \tag{10.1}$$

The signal strength obtained by the cut-based analysis is

$$\mu = 1.12 \pm 0.42(\text{stat.}) \pm 0.40(\text{syst.}). \tag{10.2}$$

The consistency of the cut-based analysis result and MVA analysis result is 8% (expected to be 67% correlated). We take the cut-based analysis as a cross check to MVA analysis, since the expected significance for cut-based analysis 2.0σ, while 2.5σ is obtained from MVA analysis. The diboson cross section measurement is performed with exactly same method as the present analysis to validate the analysis method.

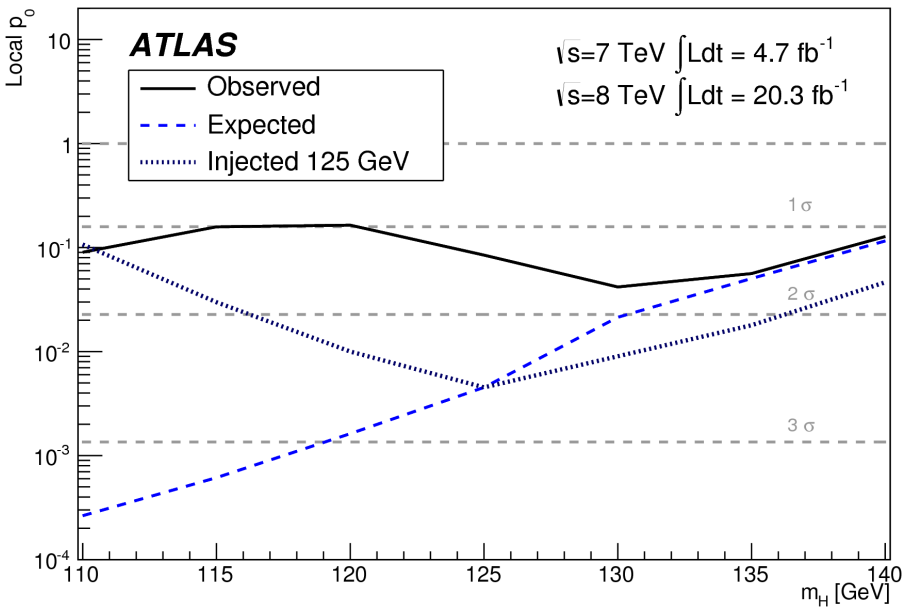

Figure 10.24: Observed (solid) and expected (dashed and dotted) local p_0 values as a function of the assumed Higgs boson mass, evaluated under the background-only hypothesis. The expected curves test the null hypothesis when the Higgs signal is present, with the assumed mass (dashed) or 125 GeV/c^2 (dotted). ashed curve).

The fitted signal strength with MVA analysis is

$$\mu_{VZ} = 0.77 \pm 0.10(\text{stat.}) \pm 0.15(\text{syst.}) \tag{10.3}$$

and with cut-based mass analysis is

$$\mu_{VZ} = 0.79 \pm 0.11(\text{stat.}) \pm 0.16(\text{syst.}) \tag{10.4}$$

for the 8-TeV dataset. The signal strength for combined 7-TeV and 8-TeV datasets obtained by MVA analysis is

$$\mu_{VZ} = 0.74 \pm 0.09(\text{stat.}) \pm 0.14(\text{syst.}). \tag{10.5}$$

The significance of this result is 4.9, to be compared to an expected significance of 6.3σ.

Table 10.1 lists the breakdown of the uncertainty on the measured signal strength obtained with the MVA analysis for the 8 TeV data. The individual sources of systematic uncertainty by category are combined. To assess the contribution of systematic uncertainties by category to the total systematic uncertainty, all NPs associated with the uncertainties within the category are fixed to their fitted values and the fit is repeated. The difference in quadrature between the uncertainties on the measured signal strength the one from this fit and from the nominal fit provides an estimate of the systematic uncertainty, which is attached to the uncertainties from the considered category. The sum in quadrature of the systematic uncertainties by category differs from the total systematic uncertainty due to correlations. For the W+jets, Z+jets and $t\bar{t}$ backgrounds, the uncertainties arising from the floating normalisations and those arising from the modelling are reported independently. The uncertainty due to b-tagging for all jet flavours combined is 10%.

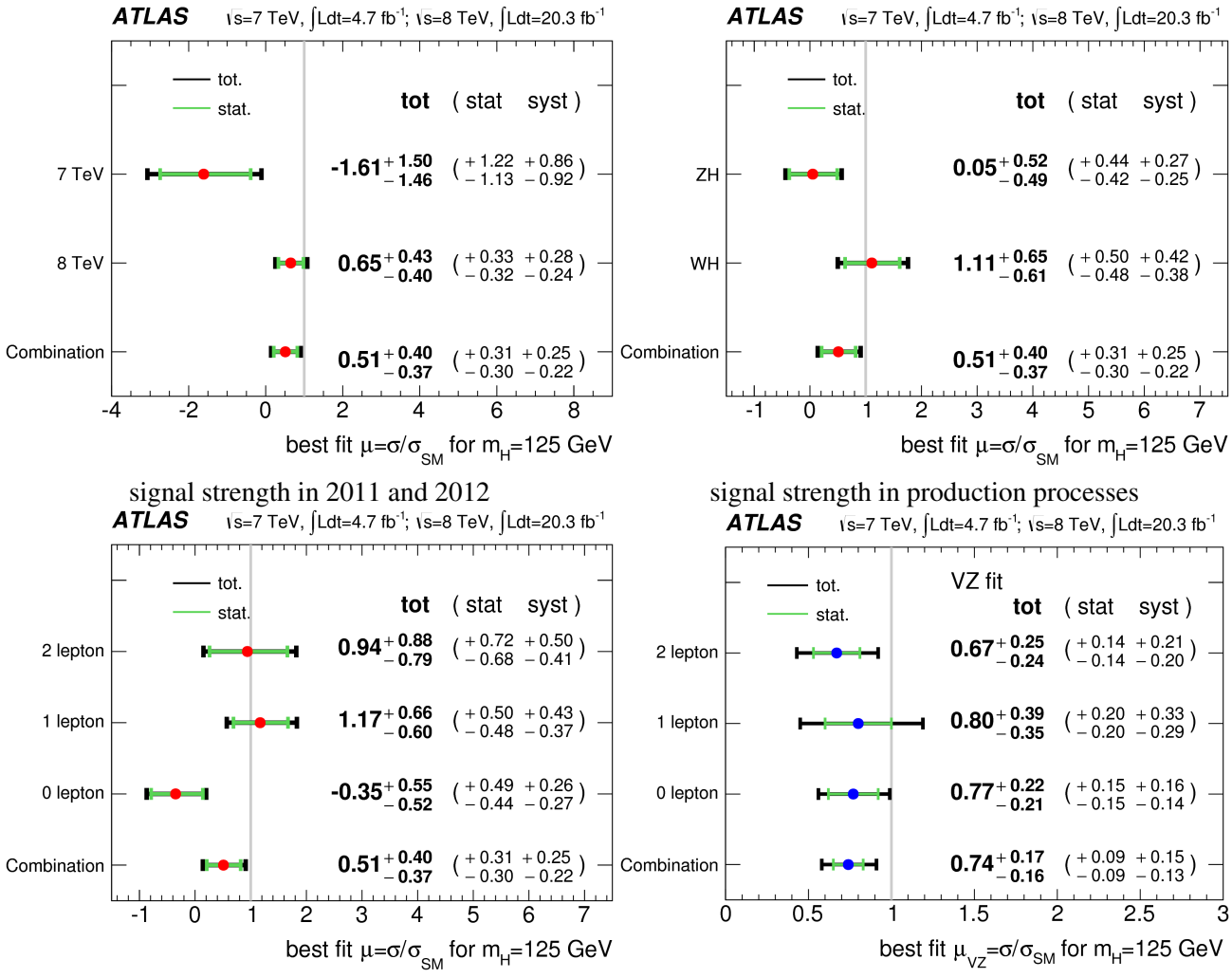

signal strength in 2011 and 2012

signal strength in production processes

signal strength in analysis channel

signal strength for diboson

Figure 10.25: Fitted signal strength parameters for the Higgs bosons in various sub-datasets and for VZ boson production.

Table 10.1: Breakdown of the uncertainty on the signal strength.

Source of uncertainty		σ_μ
Total		0.41
Statistical		0.32
Systematic		0.26
Experimental uncertainties		
Jets		0.08
$E_{\mathrm{T}}^{\mathrm{miss}}$		0.03
Leptons		0.01
b-tagging	b-jets	0.07
	c-jets	0.04
	light jets	0.04
Luminosity		0.03
Theoretical and modelling uncertainties		
Signal		0.07
Floating normalisations	W+jets	0.06
	Z+jets	0.03
	$t\bar{t}$	0.04
Background modelling	W+jets	0.11
	Z+jets	0.08
	$t\bar{t}$	0.5
Single-top		0.04
Diboson		0.02
Multi-jet		0.06

10.4 Additional materials

Figures 10.26 left plot shows the data, signal with the Standard Model prediction($\mu = 1$) and fitted background yields. The signal to background ratio of last bin (bin 9) is 0.7, second last bin (bin 8) is 0.3 and third last bin (bin 7) is 0.09. Signal contribution in these three bins slightly lower but statistically consistent with the SM expectation. The data and background expectation in background dominant region shows a good agreement. Figures 10.26 right plot shows the m_{bb} distribution in data after subtraction of background except the diboson background. The Z^0 boson mass peak is clearly seen around Z^0 boson mass and the excess in the data is consistent with the Standard Model Higgs boson prediction. The sideband of the Z^0 and H ($m_H = 125$ GeV) is consistent with zero.

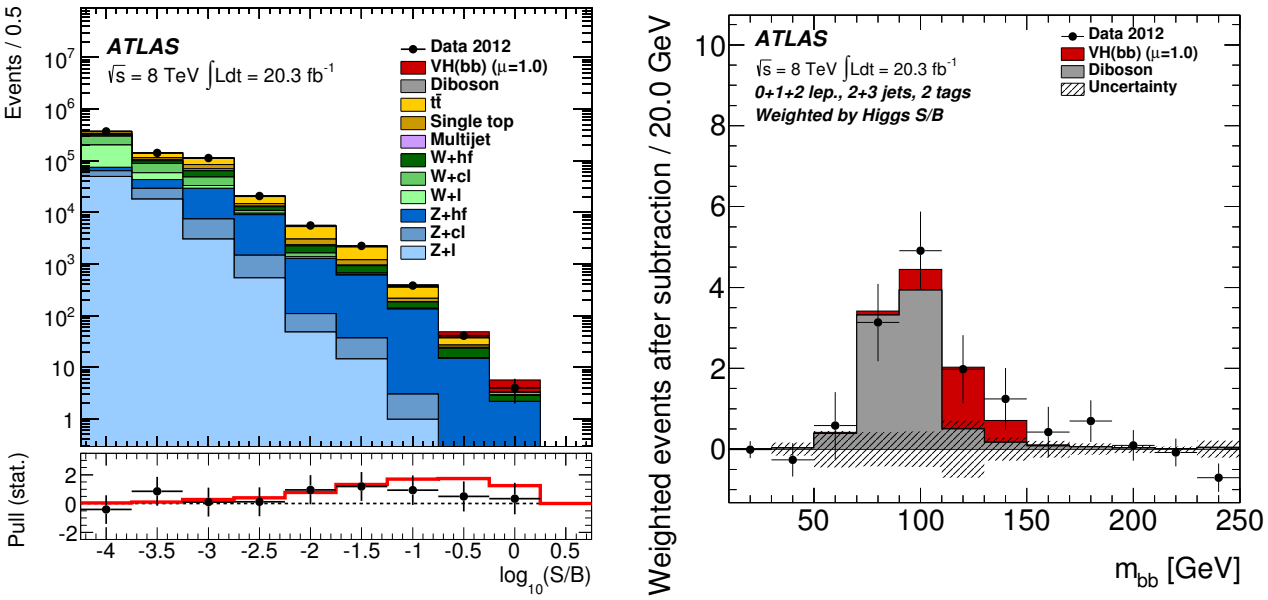

Figure 10.26: (left) Event yields as a function of log(S/B) for data and background process as obtained with the MVA analysis and (right) the di-jet mass distributions in data after subtraction of all backgrounds except for the diboson production processes.

10.5 Comparison with other experimental results

Figures 10.27, shows the significance results of ATLAS, CMS [92] and Tevatron [93] experiments, the present result achieved the best sensitivity in all $H \to b\bar{b}$ analyses, presenting a direct evidence of Higgs boson coupling to the quark sector, as postulated in the Standard Model. Three experiment group analyzed zero lepton, one lepton and two lepton final states. Each tevatron group (CDF experiment and D0 experiment) analysed the data taken at $\sqrt{s} = 1.96$ TeV, correspond to integrated luminosity up to 9.7 fb^{-1}. All analysis groups used MVA technique to maximise the sensitivity to the higgs boson signal.

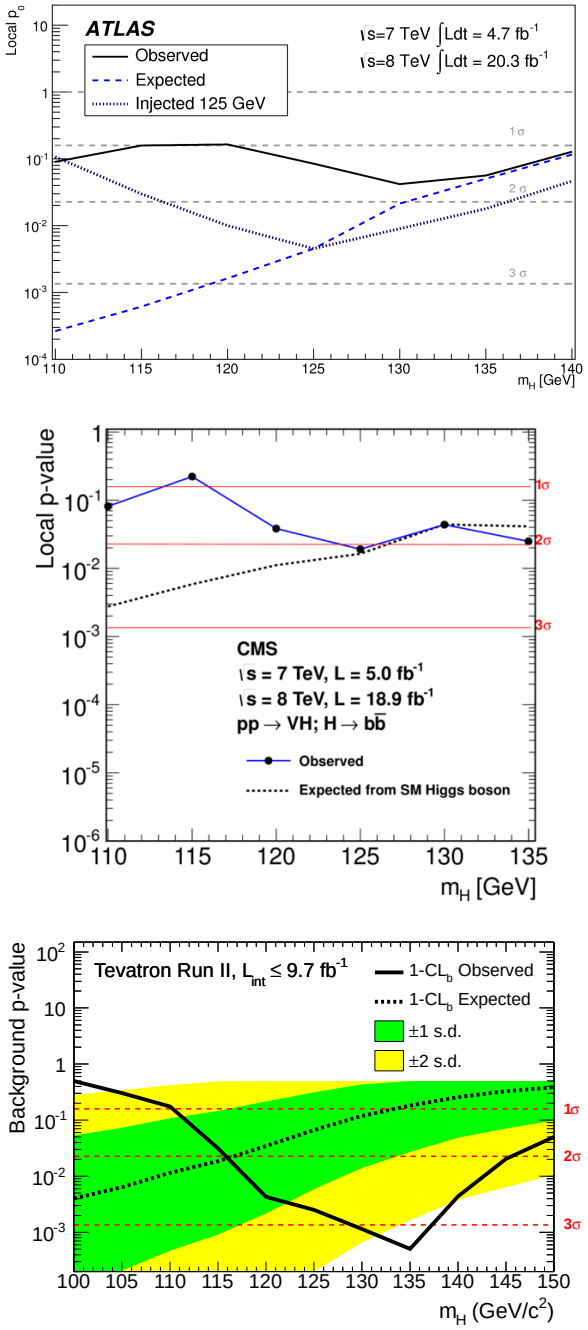

Figure 10.27: Observed (solid) and expected (dashed and dotted) local p_0 values as a function of the assumed Higgs boson mass, evaluated under the background-only hypothesis. Local p_0 values of cuntion of the Higgs mass calculated under a hypothesis of background-only. (Top) ATLAS experiment (same plot as in Figure 10.24), (middle) CMS experiment [92] and (bottom) Tevatron combined [93].

Chapter 11

Conclusion

Search for the Standard Model Higgs boson decaying in to $H \to b\bar{b}$ channel has been performed with the ATLAS detector at the Large Hadron Collider. This search focuses on the weak boson associated production ($(W^{\pm}/Z^0)H$) analysis using the full 2012 pp collision data sample of 20.3 fb^{-1} recorded at $\sqrt{s} = 8$ TeV. The data is divided into three channels according to the number of observed leptons from weak boson decay: $Z^0H \to \nu\bar{\nu}b\bar{b}$, $W^{\pm}H \to \ell^{\pm}\nu b\bar{b}$ and $Z^0H \to \ell^+\ell^- b\bar{b}$. With the combination of full 2011 pp collision data sample of 4.6 fb^{-1} recorded at $\sqrt{s} = 7$ TeV, the observed (expected) deviation from the background-only hypothesis corresponds to a local significance of 1.4 (2.6) standard deviations and the ratio of the measured signal yield to the Standard Model Higgs boson expectation is found to be $\mu = 0.52 \pm 0.32$ (stat)± 0.24 (syst). This result is consistent with the Standard Model Higgs boson expectation with mass $m_H = 125$ GeV/c^2.

Bibliography

[1] A. Purcell, A standard infographic for the standard model, 2012, http://www.isgtw.org/spotlight/go-particle-quest-first-cern-hackfest.

[2] M. Peskin and D. Schroeder, *An Introduction to Quantum Field Theory*Advanced book classics (Addison-Wesley Publishing Company, 1995).

[3] Particle Data Group, K. Olive *et al.*, Chin.Phys. **C38**, 090001 (2014).

[4] P. A. M. Dirac, Proceedings of the Royal Society of London A: Mathematical, Physical and Engineering Sciences **114**, 243 (1927).

[5] E. Fermi, Rev. Mod. Phys. **4**, 87 (1932).

[6] S. Tomonaga, Progress of Theoretical Physics **1**, 27 (1946), http://ptp.oxfordjournals.org/content/1/2/27.full.pdf+html.

[7] J. Schwinger, Phys. Rev. **73**, 416 (1948).

[8] J. Schwinger, Phys. Rev. **74**, 1439 (1948).

[9] R. P. Feynman, Phys. Rev. **76**, 769 (1949).

[10] R. P. Feynman, Phys. Rev. **76**, 749 (1949).

[11] F. J. Dyson, Phys. Rev. **75**, 486 (1949).

[12] F. J. Dyson, Phys. Rev. **75**, 1736 (1949).

[13] C. N. Yang and R. L. Mills, Phys. Rev. **96**, 191 (1954).

[14] O. W. Greenberg, Phys. Rev. Lett. **13**, 598 (1964).

[15] Y. Nambu, p. 133 (1966).

[16] M. Y. Han and Y. Nambu, Phys. Rev. **139**, B1006 (1965).

[17] F. Englert and R. Brout, Phys. Rev. Lett. **13**, 321 (1964).

[18] P. W. Higgs, Phys. Lett. **12**, 132 (1964).

[19] P. W. Higgs, Phys. Rev. Lett. **13**, 508 (1964).

[20] G. S. Guralnik, C. R. Hagen, and T. W. B. Kibble, Phys. Rev. Lett. **13**, 585 (1964).

[21] P. W. Higgs, Phys. Rev. **145**, 1156 (1966).

[22] T. W. B. Kibble, Phys. Rev. **155**, 1554 (1967).

[23] S. L. Glashow, Nuclear Physics **22**, 579 (1961).

[24] S. Weinberg, Phys. Rev. Lett. **19**, 1264 (1967).

[25] A. Salam, (1969), Proc. of the 8th Nobel Symposium on 'Elementary Particle Theory, Relativistic Groups and Analyticity', Stockholm, Sweden, 1968, edited by N. Svartholm, p. 367-377.

[26] N. Cabibbo, Physical Review Letters **10**, 531 (1963).

[27] M. Kobayashi and T. Maskawa, Progress of Theoretical Physics **49**, 652 (1973).

[28] B. Pontecorvo, Soviet Journal of Experimental and Theoretical Physics **26**, 984 (1968).

[29] Z. Maki, M. Nakagawa, and S. Sakata, Progress of Theoretical Physics **28**, 870 (1962).

[30] L. Faddeev and V. Popov, Phys.Lett. **B25**, 29 (1967).

[31] W. A. Bardeen, A. J. Buras, D. W. Duke, and T. Muta, Phys. Rev. D **18**, 3998 (1978).

[32] T. Van Ritbergen, J. Vermaseren, and S. Larin, Physics Letters B **400**, 379 (1997).

[33] K. Chetyrkin, B. A. Kniehl, and M. Steinhauser, Nucl.Phys. **B510**, 61 (1998), arXiv:hep-ph/9708255.

[34] S. Bethke, Eur.Phys.J. **C64**, 689 (2009), arXiv:0908.1135.

[35] Y. L. Dokshitzer, Sov.Phys.JETP **46**, 641 (1977).

[36] V. Gribov and L. Lipatov, Sov.J.Nucl.Phys. **15**, 438 (1972).

[37] G. Altarelli and G. Parisi, Nucl.Phys. **B126**, 298 (1977).

[38] S. Moch, J. Vermaseren, and A. Vogt, Nucl.Phys. **B688**, 101 (2004), arXiv:hep-ph/0403192.

[39] LHC Higgs Cross Section Working Group, S. Dittmaier, C. Mariotti, G. Passarino, and R. Tanaka (Eds.), CERN-2011-002 (CERN, Geneva, 2011), arXiv:1101.0593.

[40] J. R. Ellis, M. K. Gaillard, and D. V. Nanopoulos, Nucl. Phys. B **106**, 292 (1976).

[41] T. Han and S. Willenbrock, Phys.Lett. **B273**, 167 (1991).

[42] P. Baikov, K. Chetyrkin, and J. H. Kuhn, Phys.Rev.Lett. **96**, 012003 (2006), arXiv:hep-ph/0511063.

[43] LHC Higgs Cross Section Working Group, S. Heinemeyer, C. Mariotti, G. Passarino, and R. Tanaka (Eds.), CERN-2013-004 (CERN, Geneva, 2013), arXiv:1307.1347.

[44] ATLAS, Summary plots from the atlas higgs physics group, `https://atlas.web.cern.ch/Atlas/GROUPS/PHYSICS/CombinedSummaryPlots/HIGGS/`.

[45] CMS Collaboration, CERN Report No. CMS-PAS-HIG-14-009, 2014 (unpublished).

[46] Physics Letters B **726**, 120 (2013).

[47] F. Marcastel, (2013), General Photo.

[48] A. Team, Diagram of an LHC dipole magnet., 1999.

[49] M. Lamont, Journal of Physics: Conference Series **455**, 012001 (2013).

[50] ATLAS, Luminosity public results, `https://twiki.cern.ch/twiki/bin/view/AtlasPublic/LuminosityPublicResults`.

[51] J. Pequenao and P. Schaffner, An computer generated image representing how ATLAS detects particles, 2013.

[52] J. Pequenao, Computer generated image of the whole ATLAS detector, 2008.

[53] ATLAS, G. Aad *et al.*, JINST **3**, S08003 (2008).

[54] R. L. Gluckstern, Nuclear Instruments and Methods **24**, 381 (1963).

[55] J. Pequenao, Computer generated image of the ATLAS inner detector, 2008.

[56] T. Rohe, G. Lutz, R. H. Richter, F. Hugging, and R. Wunstorf, Nucl.Instrum.Meth. **A409**, 224 (1998).

[57] J. Pequenao, Computer generated images of the Pixel, part of the ATLAS inner detector., 2008.

[58] J. Pequenao, Computer Generated image of the ATLAS calorimeter, 2008.

[59] ATLAS Electromagnetic Barrel Liquid Argon Calorimeter Group, B. Aubert *et al.*, Nucl.Instrum.Meth. **A558**, 388 (2006).

[60] J. Pequenao, Computer generated image of the ATLAS Muons subsystem, 2008.

[61] W. Buttinger, Journal of Physics: Conference Series **396**, 012010 (2012).

[62] P. Billoir and S. Qian, Nuclear Instruments and Methods in Physics Research Section A: Accelerators, Spectrometers, Detectors and Associated Equipment **311**, 139 (1992).

[63] W. Lampl *et al.*, ATL-LARG-PUB-2008-002 (2008), https://cds.cern.ch/record/1099735.

[64] ATLAS Collaboration, ATLAS-CONF-2014-032 (2014), https://cds.cern.ch/record/1706245.

[65] A. Collaboration, The European Physical Journal C **74** (2014).

[66] ATLAS, G. Aad *et al.*, (2014), arXiv:1407.3935.

[67] M. Cacciari, G. P. Salam, and G. Soyez, JHEP **04**, 063 (2008), arXiv:0802.1189.

[68] ATLAS Collaboration, CERN Report No. ATL-COM-PHYS-2013-449, 2013 (unpublished).

[69] ATLAS, G. Aad *et al.*, CERN Report No. ATLAS-CONF-2013-083, 2013 (unpublished).

[70] ATLAS Collaboration, (2014), arXiv:1406.0076.

[71] ATLAS Collaboration, ATLAS-CONF-2013-082 (2013), https://cds.cern.ch/record/1570993.

[72] ATLAS, G. Aad *et al.*, CERN Report No. ATLAS-CONF-2014-046, 2014 (unpublished).

[73] ATLAS, G. Aad *et al.*, CERN Report No. ATLAS-CONF-2014-004, 2014 (unpublished).

[74] ATLAS Collaboration, ATLAS-CONF-2012-039 (2012), https://cdsweb.cern.ch/record/1435193.

[75] ATLAS Collaboration, ATLAS-CONF-2012-040 (2012), https://cdsweb.cern.ch/record/1435194.

[76] ATLAS Collaboration, ATLAS-CONF-2012-043 (2012), https://cdsweb.cern.ch/record/1435197.

[77] T. Sjöstrand, S. Mrenna, and P. Z. Skands, JHEP **05**, 026 (2006), arXiv:hep-ph/0603175.

[78] I. W. Stewart and F. J. Tackmann, Phys.Rev. **D85**, 034011 (2012), arXiv:1107.2117.

[79] A. D. Martin *et al.*, Eur. Phys. J. **63**, 189 (2009), arXiv:0901.0002v3.

[80] R. D. Ball *et al.*, Nucl.Phys. **B867**, 244 (2013), arXiv:1207.1303.

[81] H.-L. Lai *et al.*, Phys.Rev. **D82**, 074024 (2010), arXiv:1007.2241.

[82] A. Denner, S. Dittmaier, S. Kallweit, and A. Mück, PoS **EPS-HEP2011**, 235 (2011), arXiv:1112.5258.

[83] M. L. Mangano, M. Moretti, F. Piccinini, R. Pittau, and A. D. Polosa, JHEP **0307**, 001 (2003), arXiv:hep-ph/0206293.

[84] S. Frixione, P. Nason, and C. Oleari, JHEP **0711**, 070 (2007), arXiv:0709.2092.

[85] S. Alioli, P. Nason, C. Oleari, and E. Re, JHEP **1006**, 043 (2010), arXiv:1002.2581.

[86] C. Oleari and L. Reina, JHEP **1108**, 061 (2011), arXiv:1105.4488.

[87] J. Alwall *et al.*, (2014), arXiv:1405.0301.

[88] G. Corcella et al., JHEP **0101**, 010 (2001).

[89] B. P. Kersevan and E. Richter-Was, (2004), arXiv:hep-ph/0405247.

[90] J. M. Campbell and R. Ellis, Nucl.Phys.Proc.Suppl. **205-206**, 10 (2010), arXiv:1007.3492.

[91] A. Hoecker *et al.*, PoS **ACAT**, 040 (2007), arXiv:physics/0703039.

[92] ATLAS Collaboration, CMS-PAS-HIG-13-012 (2013), https://cds.cern.ch/record/1546801.

[93] CDF, D0 Collaborations, Phys.Rev.Lett. **109**, 071804 (2012), arXiv:1207.6436.